$$\dot{u} = \frac{1}{m_{RB11} + a_{11}}(m_{RB11}vr - m_{RB11}wq - a_{13}(\infty)\dot{w} - a_{15}(\infty)\dot{q} - \int_0^\infty \mathrm{k}_{11}(t-\tau)u\,(\tau)d\tau - \int_0^\infty \mathrm{k}_{13}(t-\tau)\mathrm{w}(\tau)$$
$$- \int_0^\infty \mathrm{k}_{15}(t-\tau)\mathrm{p}(\tau)d\tau + \sum_{i=1}^{N}\left(\frac{F_{wx_i}}{\zeta_{a_i}}\right)\cos(\omega_i t + \varepsilon_i + \varepsilon_{wx\zeta_i}) + \sum_{i=1}^{N}\sum_{j=1}^{N}\zeta_i\zeta_j \cdot \bar{P_{x_{ij}}} \cdot \sin[(\omega_i - \omega_j)t + (\epsilon_i - \epsilon_j)]$$
$$+ \sum_{i=1}^{N}\sum_{j=1}^{N}\zeta_i\zeta_j \cdot \bar{Q_{x_{ij}}} \cdot \sin[(\omega_i - \omega_j)t + (\epsilon_i - \epsilon_j)] + X_{hull} + X_{rud} + X_{prop} + X_{wind})$$

$$\dot{v} = \frac{1}{m_{RB22} + a_{22}}(m_{RB22}wp - m_{RB22}ur - a_{24}(\infty)\dot{p} - a_{26}(\infty)\dot{r} - \int_0^\infty \mathrm{k}_{22}(t-\tau)\mathrm{v}\,(\tau)d\tau - \int_0^\infty \mathrm{k}_{46}(t-\tau)\mathrm{p}(\tau)d\tau$$
$$- \int_0^\infty \mathrm{k}_{26}(t-\tau)\mathrm{r}(\tau)d\tau + \sum_{i=1}^{N}\left(\frac{F_{wy_i}}{\zeta_{a_i}}\right)\cdot\cos(\omega_i t + \varepsilon_i + \varepsilon_{wx\zeta_i}) + \sum_{i=1}^{N}\sum_{j=1}^{N}\zeta_i\zeta_j \cdot \bar{P_{y_{ij}}}\sin[(\omega_i - \omega_j)t + (\epsilon_i - \epsilon_j)]$$

A Modular Unified Model of Ship Manoeuvering in Irregular Wind Generated Waves

L.J. van Tongeren

Figure 1: Castillo de Tebra.

$$\dot{r} = \frac{1}{I_{66}+a_{66}}(-a_{62}(\infty)\dot{v} - a_{64}(\infty)\dot{p} - \int_0^\infty \mathrm{k}_{62}(t-\tau)\dot{v}\,(\tau)d\tau - \int_0^\infty \mathrm{k}_{44}(t-\tau)\dot{p}(\tau)d\tau - \int_0^\infty \mathrm{k}_{64}(t-\tau)\dot{r}(\tau)d\tau +$$
$$\sum_{i=1}^{N}\left(\frac{F_{wn_i}}{\zeta_{a_i}}\right)\cdot\cos(\omega_i t + \varepsilon_i + \varepsilon_{wx\zeta_i}) + \sum_{i=1}^{N}\sum_{j=1}^{N}\zeta_i\zeta_j \cdot \bar{P_{n_{ij}}}\cdot\sin[(\omega_i - \omega_j)t + (\epsilon_i - \epsilon_j)] + \sum_{i=1}^{N}\sum_{j=1}^{N}\zeta_i\zeta_j \cdot \bar{Q_{n_{ij}}}\cdot$$
$$\sin[(\omega_i - \omega_j)t + (\epsilon_i - \epsilon_j)] + N_{hull} + N_{rud} + N_{wind})$$

TU Delft

Thesis for to pursuit a MSc degree in Marine Technology in the specialization of *Mechanical Engineering.*

MT.22/23.001.M

A Modular Unified Model of Ship Manoeuvering in Irregular Wind Generated Waves

By

Lindert J. van Tongeren

Performed at

Technical University Delft

This thesis is classified as confidential in accordance with the general conditions for projects performed by the Technical University Delft.

To be defended publicly on
18 October 2022 at 10:00

Company supervisors

Responsible supervisor:	Dr. ir. P. de Vos
E-mail:	P.deVos@tudelft.nl

Thesis exam committee

Chair:	Dr. ir. P.R. Wellens
Staff Member:	Dr. ir. P de Vos
Staff Member:	Dr. ir. C. Sui

Author Details

Study number:	4282132
Author contact e-mail:	Lindert.van.tongeren@gmail.com

Preface

To comply with the Energy Efficiency Design Index a simple suggested short term solution is the installation of less engine power. Therefore, concerns have been raised to the survivability of ships in adverse weather conditions. Therefore, Sui (2021) developed a holistic simulation model, from 'tank to wake' of a manoeuvring ship in irregular waves to investigate a minimum power limit for regulation purposes. The model contains sophisticated methods to simulate the behaviour of the components of propulsion system and a hydrodynamic model is included. I am appreciative that he published a master thesis topic on the improvement of the hydrodynamics of his simulation. At that point, I was attracted to work with a model of a ship manoeuvring in waves. The design, hydrodynamics and systems onboard of the ship are often treated separately. Yet, the ship needs to perform all together. This holistic principle and interdisciplinary character of the study is important to me. My contribution to the model consists of modular unified model based on the Cummins equation wherein the manoeuvring forces of Kijima model are included as non-linear damping in the motion equation. Furthermore, I have provided a model to obtain realistic sea conditions for the storms that the endangered ships encounter provided a sea state.

I am happy with the results, although; it must be acknowledged that there is still room for improvements. But as Peter de Vos puts it; 'Research is never finished'. I am looking back on a period in which I have obtained a lot of knowledge and developed new skills. Therefore, I am grateful to Congbiao Sui, Peter de Vos, and Peter Wellens for inspiring me with new ideas and concepts and supporting me throughout the research.

Theories and results are often profoundly published whereas the implementation are treated timidly in sentences like; 'The theory is implemented in a Matlab-Simulink environment'. Therefore, I want to thank Thor I. Fossen and Tristan Perez for opening up the maritime research community with the openly available models in the Simulink Library 'Maritime Systems Simulator'. I think it is the foundation of science to make research insightful and reproducible.

Eventually, I must acknowledge that at the time I started, I was unaware of the difficult challenge it is to graduate during a pandemic. Yet, I have persisted, but want to thank Pleun and my family for their support and patience during this time.

Abstract

With the introduction of the Energy Efficiency Design Index, concerns have been raised to the survivability of ships with small engine power to maintain manoeuvring capabilities in adverse weather conditions. Therefore, Sui (2021) developed a simulation model from 'tank to wake' of a manoeuvring ship in irregular waves to advice a minimum power limit for regulation purposes. The original model consists of the Kijima model extended with the mean second order wave drift forces of a VLCC tanker published by (Yasukawa et al., 2019).

The research reported in this thesis is conducted as part of this work. Therefore, the aim is to improve the fidelity of hydrodynamics. Therefore, a modular unified model is established where the manoeuvring forces of Kijima model are included as non-linear damping in the Cummings equation. Whereas only the mean second order wave drift forces were included in the original model, the first and second order wave excitation forces, the radiation forces, and the restoring forces are included in the new model. The convolution integrals of the radiation damping forces are circumvented with state space models with the identification method of Perez & Fossen (2009). The input of the forces are the force response amplitude operators, the quadratic transfer functions, and the added mass and damping coefficients in the frequency domain obtained from the diffraction analysis performed on a barge in Ansys Aqwa, because the hull geometry of the benchmark ship is unknown.

Moreover, a wave generation model is included capable of generating sea surface realizations for irregular waves from multiple wave spectra. In this study, irregular long crested wind generated waves are generated from a JONSWAP spectrum. The JONSWAP spectrum is generated based on the wind growth curves and thus depend on the wind speed. Consequently, the significant wave height and the peak period of the spectrum are consistent.

The model is validated against the measurements of the benchmark turning trail and compared to the original model. The original model is slightly more accurate. Nevertheless, both results are considered acceptable, and, it is concluded that that the fidelity of the models is similar.

Thereof, the model is used to simulate a ship escaping an increasing storm based on the case of the Pasha Bulker. Therefore, a turn from beam to head waves starting at a low velocity is simulated in sea state 7, 8, and 9. In the original simulation, the ship failed in sea state 9. With the new model, the ship is able to perform all turns. Therefore, it is concluded that the ship is not underpowered. Consequently, the engine power is reduced. With half installed power the ship fails to escape the storm and it is endangered.

List of symbols

Roman symbols

$\overline{KG}$	The height of centre of mass w.r.t. the keel
A	Added mass matrix
$\hat{A}$	State matrix
$\hat{A}_{ik}$	Coefficient of the state matrix
A_∞	Added mass matrix evaluated as frequency approaches infinity
a_{ij}	Added mass matrix coefficient
B	Damping matrix
B	Beam
$\hat{B}$	Input matrix
$\hat{B}_{ik}$	Coefficient of the input matrix
C	Restoring force or hydrodynamic stiffness matrix
$\hat{C}$	Output matrix
c_{ij}	Restoring force matrix coefficient
D	Moulded depth
d	Draught
d	water depth
$\tilde{d}$	Non-dimensional water depth
$\boldsymbol{F}$	Force vector
$\tilde{F}$	Non-dimensional fetch
$\boldsymbol{F_{FK,D}}$	Force vector containing the combined Froude-Krylov and diffraction force
$\boldsymbol{F_{2nd}}$	Second order wave force vector
$\boldsymbol{F\_A}$	Wind force vector
$\boldsymbol{F_D}$	Diffraction force vector
$\boldsymbol{F_{FK}}$	Froude-Krylov force vector
$\boldsymbol{F_H}$	Hull force vector
F_k	Force component for a degree of freedom
$\boldsymbol{F_P}$	Propellor force vector
$\boldsymbol{F_R}$	Rudder force vector
$\boldsymbol{F_{rad}}$	Radiation force vector
$\boldsymbol{F_{res}}$	Restoring force vector
$\boldsymbol{F_v}$	Viscous force vector
$\boldsymbol{F_W}$	Wave force vector
g	Gravity constant
$\tilde{H}$	Non-dimensional significant wave height
$\tilde{H}_\infty$	Non-dimensional significant wave height for fully developed seas
I	Identity matrix
$\boldsymbol{i}$	Complex operator
$\boldsymbol{i}$	Unit vector
I_{ii}	Moment of Inertia of a degree of freedom
I_{xx}	Mass moments of inertia around the x-axis
I_{yy}	Mass moments of inertia around the y-axis
I_{zz}	Mass moments of inertia around the z-axis
K	Matrix containing the impulse response functions
$\hat{K}$	A matrix containing transfer functions
k_1	Growth curve coefficients
k_2	Growth curve coefficients
k_3	Growth curve coefficients
k_4	Growth curve coefficients

k_{ij}	Impulse response function matrix coefficient
K_{jk}	Impulse response function
L_{pp}	Length between perpendiculars
M	Rigid body mass matrix
m	The mass of the ship
m_1	Growth curve coefficients
m_2	Growth curve coefficients
m_3	Growth curve coefficients
m_4	Growth curve coefficients
M_{RB}	Rigid body mass matrix
m_{RBii}	Mass matrix coefficient corresponding to a degree of freedom
p	Growth curve coefficients
p	Rotation rate around the x-axis
p	Nominator coefficients of the transfer function
P_{ij}^{-}	The in-phase difference quadratic transfer function (QTF)
P_{ij}^{+}	The in-phase sum quadratic transfer function (QTF)
P_{ik}	Nominator of the transfer function
q	Growth curve coefficients
q	Rotation rate around the y-axis
q	Denominator coefficients of the transfer function
Q_{ij}^{-}	The out-of-phase difference quadratic transfer function (QTF)
Q_{ij}^{+}	The out-of-phase sum quadratic transfer function (QTF)
Q_{ik}	Denominator of the transfer function
r	Rotation rate around the z-axis
R^2	Coefficient of determination
S	Wetted surface
s	The Laplace operator
$\boldsymbol{s}_k$	Normal vector of the wetted surface
t	Time
T	Transformation matrix
$\tilde{T}$	Non-dimensional peak period
$\tilde{T}_{\infty}$	Non-dimensional peak period for fully developed seas
u	Velocity in x-direction
U_{10}	Wind speed at 10 meters height above the ground
v	Velocity in y-direction
w	Velocity in z-direction
w_i	Weight coefficients of the least square estimation
$\boldsymbol{X}$	Position vector
$\mathbf{x}$	State vector
$\dot{\boldsymbol{X}}$	Velocity vector
$\ddot{\boldsymbol{X}}$	Acceleration vector
x_g	Centre of floatation w.r.t. midship($L_{pp}/2$)
x_j	Position for a degree of freedom

Greek Symbols

$\widehat{\boldsymbol{\eta}}$	Output vector that approximates the impulse response functions
∇	Displacement Volume
∇_A	The volume of the superstructures
∇_{DH}	The volume of the deckhouse
$\frac{F_{wa_i}}{\zeta_{a_i}}$	The wave load transfer function (RAO)
δ_{jk}	Impulse function
$\tilde{\varepsilon}_i$	Phase of a harmonic wave component
$\varepsilon_{w\zeta_i}$	The phase shift of the wave load with respect to the wave elevation
ϵ_i, ϵ_j	The corresponding phase shifts of the QTFs
ζ	Water surface elevation
ζ_i, ζ_j	Amplitude of a harmonic wave component
$\boldsymbol{\eta}$	Vector function containing the impulse response functions
$\boldsymbol{\theta}$	Vector containing the transfer function coefficients
ρ	Density
τ	A reference moment in time
$\boldsymbol{\tau}_{exc}$	Excitation force vector
Φ	Total fluid potential
φ_j	Fluid potential preceding the impulse
ψ_j	Fluid potential during the impulse
ω	Radial frequency
ω_i	Wave frequency of a harmonic wave component

Contents

1 Introduction

As part of the paradigm shift regarding the preservation of the environment, the International Maritime Organisation (IMO) introduced the Energy Efficiency Design Index (EEDI) for new ships in 2011. The EEDI is defined as the emitted grams of CO_2 per ship's capacity mile, e.g. g_{CO2}/t nm in the design conditions. The index is introduced to simulate the introduction of innovative propulsion systems by gradually reducing the emission allowance over time as more clean alternatives are developed. On short term, an effective solution to comply with the EEDI is to reduce the ship speed in design which practically means that these new ships have a smaller engine power installed (Sui et al., 2019; Ventikos et al., 2018). Consequently, the ships could sail with insufficient propulsion and steering capability to maintain speed and manoeuvrability in adverse weather conditions and leads to serious concerns regarding the operational safety in some circumstances (SHOPERA, 2016).

However, these concerns are not unduly. The hazard situations occur when the ships are waiting to berth anchoring off shore and a storm is closing in. Although, ship masters are alerted on this, no shelter is searched until the anchor is dragging significantly. The decision is understandable as the adverse conditions are insidious as the conditions seem gentle at the time of the warnings. The accidents happen in worsening storms, thus mild wave conditions with strengthening winds. When the ship is dragging and the master applies full engine power, the ship is not able to accelerate and overcome the environmental conditions. Consequently, groundings and collisions occur which might have been prevented with more engine power. Examples are the grounding of Pacha Bulker in Newcastle, Australia, in 2007, the collision of Bungo Princess and a bridge in Yokohama, Tokyo Bay, in 2019, and the collision of Julietta D with the Pechora Star and an offshore wind park transformer tower in Ijmuiden, Netherlands.

Subsequently, Chongbioa Sui conducted a research to predict the transport performance of an ocean-going cargo ship with small EEDI more accurately. The ultimate aim is to obtain a holistic insight in the short term complications on the operational safety in heavy operating conditions as the EEDI strives designers to reduce the propulsion and steering capacity in this circumstances. Therefore, a benchmark tanker, Castillo de Tebra, is selected as underpowered ship and its performance is modelled with a simulation from 'tank to wheel' (Sui et al., 2019). This contains sophisticated models to simulate the behaviour of the propulsion system, the electric power generation system, and the hydrodynamics of the ship hull. Subsequently, different propulsion control and energy management configurations can be analysed on their transport performances. The focus on the study has been on the machinery and that is modelled on a detailed level. Subsequently, the research is progressing in order to improve the hydrodynamics in the simulation.

The present implemented model is a manoeuvring model (Sui, 2021). The Kijima model consists of a set of 3 degree of freedom motion equations (surge, sway, yaw). It is a modular approach in which the total force is a summation of hull, rudder, propeller, and environmental forces and moments that are simulated with different models. The models for the propeller and hull force can be found in Sui et al. (2019). The manoeuvring hull forces are provided in empirical formulas for the hydrodynamic derivatives which are derived from 15 captive model experiments in which each model is towed in 48 loading conditions. Furthermore, the ships specific resistance is modelled as a function of the ship speed (Sui et al., 2019). Additionally, the wave-induced steady forces in surge and sway forces and yaw moment are included as tabular coefficients (Sui, 2021). These are computed with a strip theory on a VLCC tanker and published by (Yasukawa et al., 2019). Therefore, the aim in this study is to consider the original hydrodynamic model and to replace the wave force model with a higher fidelity model in the simulation. Besides, the model introduces a challenge for the extension with more specific wave forces as solely the main dimensions and some form coefficients are used. As a result, the exact geometrical description of the hull form of the Castillo de Tebra is unknown. Yet, the wave forces arise from the

pressure distribution on the hull wetted surface and thus depend principally on the hull form. The influence of waves on the propeller performance and the propeller-hull interaction are out of the scope of this research as it is the topic of my colleague graduate Josef Ferschtman.

This thesis starts with a brief description of the original model, with the implemented Kijima model and the wave forces that are included, in chapter 2. The aim in this study is to improve the fidelity of this model and therefore the state of the art of the modelling of ship manoeuvring in waves is scrutinized with a literature study. This is described in chapter 3. From the state of the art, it was found that generally four approaches are distinguished, i.e. model experiments, computational fluid dynamics, two time-scale approaches, and unified approaches. Thereof, it was concluded that the unified approach is both applicable in the framework of this study and the most consistent approach to include the wave forces. Subsequently, a unified approach is established and this is extensively described in chapter 4. The model is modular and based on the Cummins equation. The convolution integrals are circumvented with state space models. The waves in the model are generated from a JONSWAP spectrum for which the parameters, i.e. peak period and significant wave height, are determined from wave growth curves. This model is validated on the measurements of the turning cycle trail of the benchmark tanker and compared with original model in chapter 0. Both simulations slightly overpredict the turning cycle compared to the benchmark but provide acceptable results. In chapter 6, the simulations are executed for the ship that sails at a low velocity in beam seas and turns into head waves in storms of 7,8, and 9 Beaufort. It is seen that the ship is able to make the turn in all conditions. Thereof, the engine power is reduced. With half the engine power installed the ship is not able to make the turn. Therefore, it is concluded that the Castillo de Tebra is not an underpowered ship. This conclusions is drawn in chapter 7, also recommendations to improve the simulation are given.

2 Original Model

As mentioned in the chapter 1, the Kijima model is presently implemented in the model. Therefore, the focus in this section is to briefly introduce the Kijima model, and thereafter wave force model.

Traditionally, the manoeuvring performances are examined in calm water conditions, and, the horizontal ship motions are considered. Objectives are course keeping, changes in heading, track keeping and speed changes. Typical tests to find the manoeuvring performance are the turning test and the zigzag test. Manoeuvring is a viscosity dominated phenomenon in which fluid effects as flow separation, vortex formation, viscous and potential effects are important. These phenomena are measured with towing tank experiments and are estimated to obtain a simple model for simulation purposes. The fundamental assumption is that the fluid forces are assumed to be unique at any instant of time and solely dependent on the hull geometry, and the velocities and accelerations. This justifies the expansion of the hydrodynamic forces in a series approximation. As a result, forces are expressed a series with linear and non-linear terms in the motion equation, which are referred to as the hydrodynamic derivatives. Thereof, extensive captive model tests are performed to measure all terms in the expansion. According to Clarke (2003), these parametrizations can, in general, be divided in two classes: truncated Taylor series expansions and second-order modulus models (Fossen, 2005). The former is a pure mathematical approach whereas the latter has physical meaning as is based on cross flow drag. The Kijima model is a generalization of the second-order modulus model.

The Kijima model is an empirical method derived from the results of 15 captive model tests in which each model is tested in 48 loading conditions (Kijima et al., 2004). It is developed as a tool to predict the manoeuvring performance in an early design stage for even and trimmed keel conditions. The Kijima model consists of a set of 3 degree of freedom motion equations (surge, sway, yaw). The hydrodynamic derivatives are derived from fits on the experimental data based on low-aspect wing theory. It is a modular approach with the derived semi-empirical formulas for the hydrodynamic forces expressed in hull shape parameters like the length and the block coefficient. Over the years, the empirical formulas have been improved (Sui, 2021).

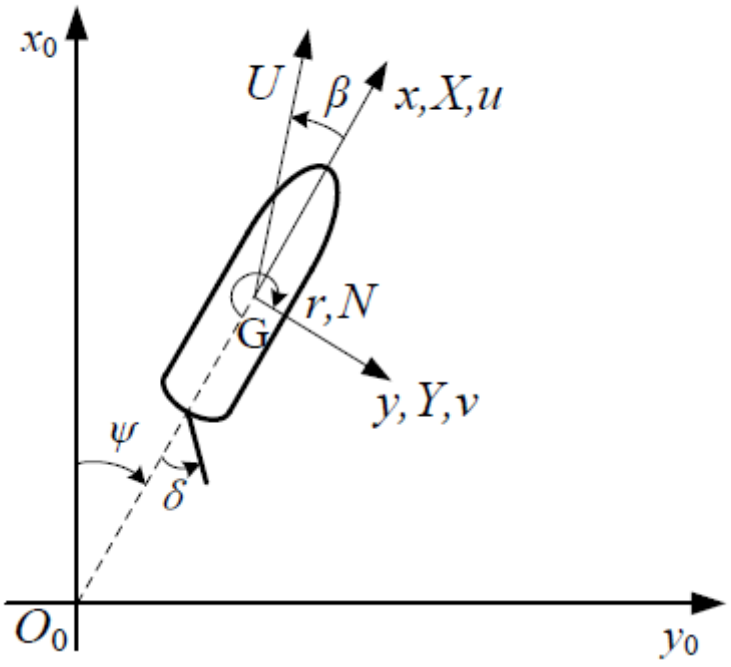

Figure 2: The reference systems in the manoeuvring simulation (Sui, 2021).

The global and body fixed reference frames of the Kijima model is given in figure 2 above. The ship is assumed to be a rigid body, and, the motion equation is from classical mechanics depending on the chosen coordinate systems. Unlike seakeeping conventions, the acceleration hydrodynamic derivatives, that represent the body reaction forces or added mass, are transferred to the kinematic side of the motion equation.

$$\begin{gathered}(m+m_x)\dot{u}-(m+m_y)vr=X\\(m+m_y)\dot{v}+(m+m_x)ur=Y\\(I_z-J_z)\dot{r}=N\end{gathered} \qquad 2\text{-}1$$

In which $\dot{u}$, $\dot{v}$ are the accelerations in the x- and y-direction and u, v, and r are the velocities in x- and y-direction and the angular velocity around the z-axis. The mass of the ship m is obtained from the known displacement ∇, and the moment of inertia I_z is estimated:

$$m=\rho\cdot\nabla \qquad 2\text{-}2$$

$$I_z=m\cdot r_{gyr}^2 \text{ where } r_{gyr}=k_{gyr}\cdot L \qquad 2\text{-}3$$

Where, ρ is the density of seawater, r_{gyr} is the radius of gyration, k_{gyr} is a coefficient that is set as 0.25 (Sui, 2021), and L is the length of the ship. Furthermore, the added masses m_x and m_y, and added moment of inertia J_z are found from empirical formulas, based on the main particulars, obtained from Dirix (2002) and Clarke et al. (1982):

$$m_x=\frac{m}{\pi\sqrt{L^3/\nabla}-14} \qquad 2\text{-}4$$

$$m_y=\frac{\pi}{2}\cdot\rho\cdot d^2\cdot L\cdot\left[1+0.16\cdot C_b\cdot\frac{B}{d}-5.1\cdot\left(\frac{B}{L}\right)^2\right] \qquad 2\text{-}5$$

$$J_z=\frac{\pi}{2}\cdot\rho\cdot d^2\cdot L^3\cdot\left[\frac{1}{12}+0.017\cdot C_b\cdot\frac{B}{d}-0.33\cdot\frac{B}{L}\right] \qquad 2\text{-}6$$

Where, d is the draught, C_b is the block coefficient, and B is the beam.

The forces and moment on the left hand side are assumed to be a superposition of the hydrodynamic forces on the hull, the rudder forces, the propeller forces, and the external environmental forces form currents, wind and waves:

$$\begin{gathered}X=X_H+X_R+X_P+X_{env}\\Y=Y_H+Y_R+Y_P+Y_{env}\\N=N_H+N_R+N_P+N_{env}\end{gathered} \qquad 2\text{-}7$$

This is referred to as a modular approach as the individual forces can be computed with different models, for example lift theory for rudders and the open-water diagram for the propeller.

As mentioned, the hull forces in calm water are described with the modulus series expansions:

$$X'_H=X'_{uu}\cdot\cos^2\beta+X'_{\beta r}\cdot r'\cdot\sin\beta \qquad 2\text{-}8$$

$$Y'_H=Y'_\beta\beta+Y'_r r'+Y'_{\beta\beta}\beta|\beta|+Y'_{rr}r'|r'|+\left(Y'_{\beta\beta r}\beta+Y'_{\beta r}r'\right)\beta r' \qquad 2\text{-}9$$

$$N'_H=N'_\beta\beta+N'_r r'+N'_{\beta\beta}\beta|\beta|+N'_r r'|r'|+\left(N'_{\beta\beta r}\beta+N'_{\beta r}r'\right)\beta r' \qquad 2\text{-}10$$

Where, X'_{uu} is the ships calm water resistance. The other hydrodynamic derivatives are indicated with the velocity components u, r and β corresponding to transverse velocity v, see figure 2 above. The accent indicates that the force components and hydrodynamic derivatives are provided in a non-dimensional form:

$$X', Y' = \frac{X}{0.5 \cdot \rho \cdot L \cdot d \cdot U^2}, \frac{Y}{0.5 \cdot \rho \cdot L \cdot d \cdot U^2}$$
$$N' = \frac{N}{0.5 \cdot \rho \cdot L^2 \cdot d \cdot U^2} \qquad 2\text{-}11$$
$$v', u' = \frac{v}{U}, \frac{u}{U}$$
$$r' = \frac{rL}{U}$$

Eventually, the hydrodynamic coefficients in equation 2-8 to 2-10 are provided with the empirical formulas as described by Sui (2021):

$$X'_{vr} = (c_m - 1) \cdot m'_y \text{ , where } c_m = 1.66 \cdot C_b - 0.49 \qquad 2\text{-}12$$

$$Y'_{\beta} = \frac{1}{2} \cdot \pi \cdot k + 1.9257 \cdot C_b \cdot \frac{B}{L} \cdot \sigma_a$$
$$Y'_r = \frac{1}{4} \cdot \pi \cdot k + 0.052 \cdot e'_a - 0.457 + (m' + m'_x)$$
$$Y'_{\beta\beta} = -0.4784 \cdot \frac{B}{d} \cdot K + 1.3 \qquad 2\text{-}13$$
$$Y'_{mr} = 0.24267 \cdot C_b \cdot \frac{d}{B} \cdot e'_a - 0.13108$$
$$Y'_{\beta rr} = -1.38643 \cdot C_b \cdot e'_a \cdot K + 1.29$$
$$Y'_{\beta\beta r} = 0.78145 \cdot e' \cdot K - 0.43232$$

$$Y'_{\beta\beta} = k \cdot \left\{150.668 \cdot \left[(1 - C_b) \cdot \frac{d}{B} \cdot e'_a \cdot K\right]^2 - 23.819 \cdot \left[(1 - C_b) \cdot \frac{d}{B} \cdot e'_a \cdot K\right] + 1.802\right\}$$
$$N'_r = -0.54 \cdot k + k^2 - 0.0477 \cdot e'_a \cdot K + 0.0368$$
$$N'_{\beta} = k \cdot \left\{150.668 \cdot \left[(1 - C_b) \cdot \frac{d}{B} \cdot e'_a \cdot K\right]^2 - 23.819 \cdot \left[(1 - C_b) \cdot \frac{d}{B} \cdot e'_a \cdot K\right] + 1.802\right\} \qquad 2\text{-}14$$
$$N'_{\beta\beta} = 43.857 \cdot \left[(1 - C_b) \cdot \frac{d}{B} \cdot e'_a \cdot K\right]^2 - 3.671 \cdot \left[(1 - C_b) \cdot \frac{d}{B} \cdot e'_a \cdot K\right] + 0.086$$
$$N'_{rr} = 0.15 \cdot K - 0.068$$
$$N'_{\beta rr} = -0.4086 \cdot C_b + 0.27$$
$$N'_{\beta\beta r} = -0.826 \cdot (1 - C_b) \cdot \frac{d}{B} \cdot e'_a - 0.026$$

In the formulas 2-13 and 2-14, L is the length of the ship, B is the beam, d is the draught, C_B is the block coefficient, and $k = \frac{2d}{L}$ is the aspect ratio. Furthermore, e_a, e'_a, σ_a, and K are shape parameters that are included in order to improve the accuracy of the force approximation in the aft ship (Kijima et al., 2004).

To complete the hydrodynamics in the simulation, the Kijima model is extended with the time averaged steady wave-induced forces and moment (Sui, 2021). Unlike the empirical formulas, the computed non-dimensional forces and moment coefficients of a benchmark SCb84 tanker published by are used, see figure 3 on the next page. The coefficients in the figures are converted to look-up tables, and, the time averaged steady wave-induced forces and moment are reproduced with equation 2-15 below.

$$\left.\begin{aligned} X_W &= \rho_w \cdot g \cdot H_{1/3}^2 \cdot (B^2/L) \cdot C_{XW}(U, T_v, \chi_W) \\ Y_W &= \rho_w \cdot g \cdot H_{1/3}^2 \cdot (B^2/L) \cdot C_{YW}(U, T_v, \chi_W) \\ N_W &= \rho_w \cdot g \cdot H_{1/3}^2 \cdot B^2 \cdot C_{NW}(U, T_v, \chi_W) \end{aligned}\right\} \qquad 2\text{-}15$$

Where ρ_w is the water density, g is the gravitational constant, $H_{1/3}^2$ is the significant wave height, C_{XW}, C_{YW}, and C_{NW} are the steady wave-induced force and moment coefficients which depend on the velocity, the averaged wave period T_v, and the relative wave direction χ_W.

The coefficients in irregular waves are defined as in equation 2-16 below.

$$\overline{C_{XW}}\,(U,T_v,\chi_0) = 2\int_{-\pi}^{\pi} G(\theta)d\theta \int_0^{\infty} C_X(U,\omega,\chi_0)\frac{S_{\zeta\zeta}(\omega)}{H_{1/3}^2}d\omega$$
$$\overline{C_{YW}}(U,T_v,\chi_0) = 2\int_{-\pi}^{\pi} G(\theta)d\theta \int_0^{\infty} C_Y(U,\omega,\chi_0)\frac{S_{\zeta\zeta}(\omega)}{H_{1/3}^2}d\omega \qquad 2\text{-}16$$
$$\overline{C_{NW}}(U,T_v,\chi_0) = 2\int_{-\pi}^{\pi} G(\theta)d\theta \int_0^{\infty} C_N(U,\omega,\chi_0)\frac{S_{\zeta\zeta}(\omega)}{H_{1/3}^2}d\omega$$

Where, $G(\theta)$ is the wave spreading function, ω is the wave frequency, $S_{\zeta\zeta}$ is a wave spectrum, and C_X, C_Y, and C_N are the steady wave force coefficients in regular waves, see equation 2-17. These steady wave force coefficients are determined by captive wave towing testes in regular waves. Time histories of the wave amplitude and phase, the model motions and hydrodynamic forces are measured. The averaged hydrodynamic forces $\overline{X_{Wm}}$, $\overline{Y_W}$, and $\overline{N_w}$ are obtained by taking the averaged value of the measured force of the time history. Where the surge force is corrected with the still water resistance:

$$C_X = \frac{R_0 - \overline{X_{Wm}}}{\rho_w g h_a^2 B^2/L}$$
$$C_Y = \frac{\overline{Y_W}}{\rho_w g h_a^2 B^2/L} \qquad 2\text{-}17$$
$$C_N = \frac{\overline{N_W}}{\rho_w g h_a^2 B^2}$$

In which, R_o is the still water resistance and h_a is the wave amplitude. Consequently, the steady wave-induced force and moment coefficients can be seen as wave force spectra. The results are validated with a free running test and the results are considered acceptable, although; the accuracy of the steady yaw moment is considered insufficient.

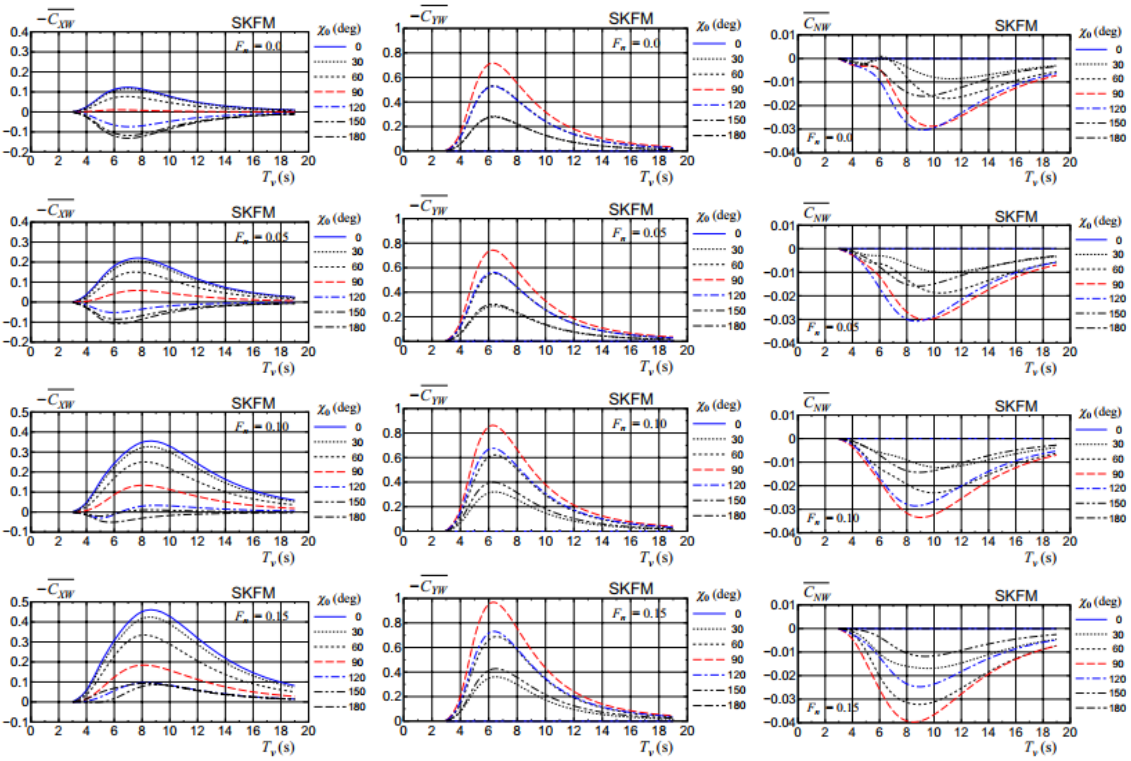

Figure 3: Coefficients of added resistance CXW , averaged steady lateral force CYW and steady yaw moment CNW in irregular waves based on the calculations by SKFM. The figure 11 is published in (Yasukawa et al., 2019).

3 State of the Art

For a general manoeuvring ship, the propeller is providing the force to advance and the origin of all forces on the hull and the rudder can be traced back to the interaction of water flow and ship motions. The exact fluid flow is established in the nonlinear partial differential Navier-Stokes equations[1] to which an analytical solution remains desired and the present computational power remains insufficient for good numerical approximations (Fossen, 2011; Larsson & Raven, 2010). Consequently, simplifications are adopted based on observations of ship behaviour and the environmental conditions in restricted waters and at open seas (Tello Ruiz, 2018). In the former, the ships obviously need to manoeuvre to avoid collisions and groundings and calm water conditions can be assumed in these sheltered waters. The horizontal, surge, sway and yaw, motions are generally considered and the dominating hydrodynamic forces and moments originate from the viscous, lift, cross flow effects. The state of the art is to model these forces as higher order series expansions. The so-called hydrodynamic coefficients, are obtained from fits to systematic towing tank experiments to measure all motion couplings; in example surge with a yaw angle. Clear sources on manoeuvring theory are Fossen (2011) and Yasukawa & Yoshimura (2015). In open seas, the ships appear to sail in straight lines with constant heading and constant velocity in waves. Therefore, the effect of propeller and rudder forces are neglected. The hydrodynamics are assumed to be dominated by wave effects and the viscous forces are neglected. The motions are assumed to be linear responses to regular wave excitations and the ship is considered to be a mass spring damper system. Generally, the motion equation is solved in the frequency domain, and, the results are the response operators and hydrodynamic coefficients. By means of spectral analysis the results are transformed to irregular actual seas. A profound explanation of seakeeping theory is written by Journée & Massie (2008).

Hence, two main-disciplines are distinguished in the traditional treatment of ship dynamics; seakeeping theory and manoeuvring theory. Fortunately, researchers, also, have carried out research to amalgamate the two disciplines since the Eighties. Subsequently, the aim in this chapter is to review the state of the art approaches to incorporate the two disciplines and to ultimately select the most suitable method that can be deployed in the further study to obtain a simulation of the ship manoeuvring in waves.

Therefore, criteria are defined to ease the selection. The starting point is the original implemented modular method in a Matlab-Simulink environment by Sui (2021). Recall that this consists of a rigid body motion equation for surge, sway, and yaw motions and where the force side is a superposition of the hydrodynamic forces derived from low-aspect lift theory in calm water, the propeller force, the rudder force. Additionally, time averaged steady wave forces and moment obtained from the results of a VLCC tanker published by Yasukawa et al. (2019)are reproduced from tabular coefficients (Sui, 2021). This approach is adopted because the lines plan of the tanker is not available due to commercial reasons. The Kijima model is suitable because it is based on empirical fits on towing tank tests results. Therefore, solely the main particulars of the ship are required. The aim is to improve this model and subsequently two criterion can be formulated:

- The method should improve the fidelity compared to the present wave forces in the manoeuvring model.
- The method should be applicable in the framework of the present model.

It is acknowledged that there is room for debate in these criterions and that these are not unequivocal. Therefore, a brief motivation is appropriate.

[1] Actually, the non-linear partial differential equations consists of the continuity equation and the Navier-Stokes equations. The former represents mass conservation and the latter momentum conservation. To determine the real flow around a ship this system of differential equations should be solved.

The first criterion is formulated to account for the improvement of fidelity of the method. In the present study the horizontal manoeuvring forces and the second order wave forces are taken into account. These forces all influence the trajectories of manoeuvres. However, the ultimate aim is to obtain insight in the minimum power requirement of the ship, as mentioned in the Introduction. Thereof, all forces and influence on the sailing ship should be included, i.e. the first- and second order wave forces. Furthermore, these forces depend on the surroundings of the ship, for example, on the water depth. Thereof, this should be seen as a veracity criterion.

The second criterion involves the absence of the lines plan of the Castillo de Tebra. The wave forces are defined as a pressure distribution around a hull surface. As far as the knowledge of the author reaches, no method exists to estimate these forces without the geometrical description of the hull shape. Consequently, a uncertainty is introduced with the absence of the exact hull shape. An approach would be to generate a hull shape based on pictures, the main particulars and the block coefficient. Nevertheless, the uncertainty on the hull geometry will be introduced. Thereof, it is chosen to save effort and the adopted approach here is to overestimate the wave forces on a barge. The focus is therefore on the method and less on accuracy of the forces on the particular ship. The subjacent notion is that more insight is gained with a working method with higher fidelity and that the model can be updated when perhaps more information is released or another case study is selected.

The following section 3.1 contains a literature review on the methods to combine the seakeeping and manoeuvring theory. It ends with a comparison of the suitable methods. This is followed with the conclusion and hence the reasoning to select the recommended approach.

3.1 Combined Manoeuvring and Seakeeping Models

Since the eighties, methods that include manoeuvring in waves are being developing, and, many studies are described by the manoeuvring committee (ITTC, 2011, 2014, 2017). The Manoeuvring Commitee 2011 distinguishes four approaches to deal with manoeuvring in waves: experimental approaches, unified theory, two time-scale approaches, and CFD. Generally, the aim in these studies is to calculate the fuel consumption and emission more accurately. Recall from the introduction that the geometry of the hull is unknown, and, that the objective is a numerical simulation. This reveals limits in the applicability of the mentioned approaches as the empirical Kijima model is already implemented. Thereof, the unified and two-time-scale approach are more suitable.

Nevertheless for the sake of completeness, the model test and CFD will first be described. Thereafter, the two time-scale approach will be explained, followed by the unified approach.

3.1.1 Model tests and CFD

The model test are stated to be the most reliable method to deal with manoeuvring in waves (ITTC, 2011). The model tests are conducted in order to find the wave forces and moments. The results are used directly in the manoeuvring motion equation or the wave loads in the theoretical model are first adjusted and used for simulations (Tello Ruiz, 2018).

Throughout literature, mostly free running test in waves are carried out for benchmark purposes. The most comprehensive study is carried out in the Energy Efficient Safe SHip OPERAtion (SHOPERA) study (Shigunov et al., 2018). The study assesses the accuracy of present numerical methods to calculate the mean second order forces and moments and the manoeuvres in waves. For benchmark data, over 1300 tests were carried out in regular waves on a VLCC tanker (KVLCC2) and the Duisburg Test Case (DTC) varying draughts, water depth, forward speeds, wave directions, wave heights, and wave periods. In addition, the test data for the KVLCC2 tanker were provided by Yasukawa & Yoshimura (2015). These data were compared to the numerical results submitted by participants. The authors conclude that numerous numerical methods are ubiquitous present to calculate the components of the time-averaged wave induced forces, but that manoeuvring is mostly considered in calm water.

Computational fluid dynamics considers the conservation of mass and momentum in the fluid domain. Due to the large computational time and the dependency on the selected turbulence model, CFD is, generally, considered as a topic of state of the art research (Zhang et al., 2017). Nevertheless, CFD provides adequate descriptions of the physics involved, especially in resistance and propulsion studies. These studies are well validated and include sinkage and trim, boundary layer flows, wake vortices and wave patterns around the ship hull (Abhiroop et al., 2018). The advantage of CFD is that more physical insight is obtained in some hydrodynamic effects with respect to captive- and free running model tests because of the difficulties in instantaneous visualization of the effects and the sophisticated measurement tools involved. Yet, in many other marine applications, the accuracy of results needs improvements and more validations (Abhiroop et al., 2018). Considering the seakeeping and manoeuvring performance, no reliable results were reported before 2014. Since, more successful seakeeping analysis appeared especially in the added resistance, heave-pitch models of normal hull shapes and free running seakeeping simulations (Abhiroop et al., 2018). Also, multiple successful studies are conducted to obtain the hydrodynamic derivatives in calm water and simulations has been done (Abhiroop et al., 2018). However, CFD studies of manoeuvring in a seaway still needs to be developed and validated. Therefore, the application of CFD is only utilized to provide the input for the hydrodynamic derivatives and can be considered as a numerical model test. An example is the study of Uharek (2019).

3.1.2 Two time-scale Approaches

In the two time-scale approaches, the manoeuvring and seakeeping theory are considered as weakly-coupled independent problems. Two time-scale approaches are modular time domain simulations which imply that the hull, rudder, propeller, and environmental forces are superimposed.

The motion equations are solved in two interchanging modules based on the distinguishes between high frequency seakeeping theory and low, read zero, frequency manoeuvring theory. Mostly the hydrodynamic derivatives are provided in a 3 or 4 DOF motion equation which is solved in manoeuvring module for the heading and the velocity in a time step. At the end of this step, the data are transferred to a seakeeping module where the wave loads are computed with strip theory or a panel method or interpolated from stored values in lookup tables. Thereof, the forces are set as new initial conditions for the next manoeuvring time step. In the models, well established theories of the seakeeping and manoeuvring discipline can be utilized because of the separation in independent modules.

The models are built in series or parallel dependent on whether the seakeeping analysis is solved in the time domain or not, see figure 4. In series, the seakeeping part is solved after the manoeuvring part and this is repeated until the simulation time ends. In parallel, the seakeeping part is solved for several timesteps while only one timestep is solved in the manoeuvring part (Tello Ruiz et al., 2012). The parallel method is found in (Lee & Kim, 2020; Seo & Kim, 2011; Zhang, 2017) and the series approach is found in (Skejic & Faltinsen, 2006, 2008; Wicaksono & Kashiwagi, 2019). The literature falls short in providing insight in which of the two is preferable.

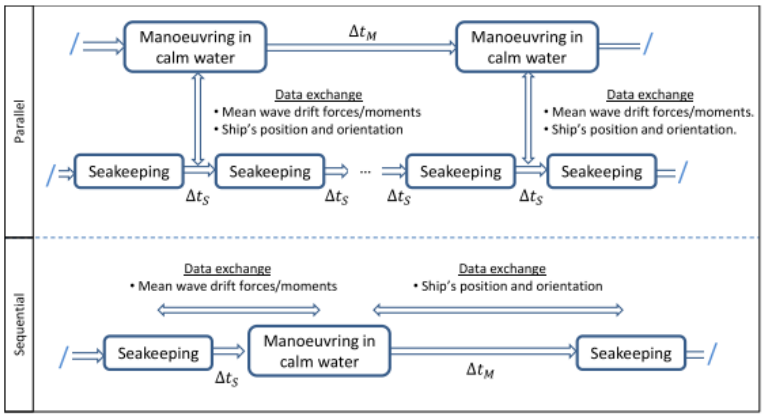

Figure 4: Difference between parallel and sequential two-time scale models(Tello Ruiz, 2018).

In table 1, state of the art two time-scale studies are compared, and, most studies have adopted the modular 3DoF manoeuvring motion. All adopted Taylor series expansion of the forces on the hull into the hydrodynamic derivatives which all are determined by model experiments except for the Söding approximations. Further, All models use a ITTC resistance formula to estimate the resistance of the vessels.

Table 1: Comparison of methods used in state of the art studies.

	Methods		
Study	**Resistance**	**Manoeuvring**	**Seakeeping**
(Skejic & Faltinsen, 2008)	ITTC formula	3DoF Taylor series with Söding approximations	Strip theories
(Seo & Kim, 2011)	ITTC formula	4DoF MMG (Taylor series)	Time domain Rankine panel method.
(Zhang et al., 2017)	ITTC formula	3DoF Taylor series with Model tests)	Time domain Rankine panel method.
(Wicaksono & Kashiwagi, 2019)	(-)	3DoF MMG (Taylor series)	Enhanced Unified (strip) Theory & New Strip Theory

The main differences are found in the methods that are adopted to solve the seakeeping analysis. However, all take the advance velocity into account in the seakeeping analysis. Skejic & Faltinsen (2006, 2008) compared four direct pressure methods based on strip theory of which one specifically for short wave lengths. Following this, Wicaksono & Kashiwagi (2018) compared two new strip theories: enhanced unified theory and new strip method and the wave drift forces are obtained from the far-field method. On the contrary, Seo & Kim (2011) solve the direct integration with a Rankine time domain panel method wherein the Newman-Kelvin linearization is utilized to linearize the surface boundary condition. This study is modified by Zhang (2017) with the introduction of the double-body model. As a result, the influence of a trailing vortex on the second order wave drift forces is included and the accuracy of the simulation is increased. Evidently, the accuracy of the wave computations differ, and, the accuracy might even be improved with another method. Comprehensive reviews on this are provided by Bunnik et al. (2010) and Fossen (2011). However, the literature does not provide insight in what the improvement of the accuracy of the wave computations contribute to the quality of the simulation results. Accordingly, the premise of Tello Ruiz (2018), that the numerical method to calculate the wave forces seemed to be selected based on an availability rather than on suitability, appears right.

The second order wave forces are computed based on the first order wave drift forces. Although the mean wave drift forces are relatively small, all authors regard only the mean drift forces as important for manoeuvring in waves, especially the second order yaw moment, whereas the first order wave forces are neglected. Also, all authors regard their results, see figure 5 below, acceptable. The discrepancies between the simulations and model experiments are considered due to inaccuracies in the computation and the measurements of the wave drift forces. All conclude that the methods are not reliable for computations of the drift forces for smaller wave lengths than half the ship length. Intriguing is that the studies discuss this accuracy in depth, but no considerations on the amalgamation method is provided. The manoeuvring theory is regarded as the basis where the wave forces are added. In contrast to Fossen (2005) considers manoeuvring theory a trivial problem in seakeeping theory in the time domain at zero frequency. At nonzero frequency, the non-linear damping from manoeuvring theory, as described in section 2, can be added directly in the time domain. From this perspective, the two time-scale approach can be considered as an engineering model.

Moreover, Skejic & Faltinsen (2008) also point out that errors appear in model test measurements in short waves. Like Ueno et al. (2003) showed with model test, Zhang et al. (2017) observed that the wave drift distance increases with decreasing wave length and conclude that the contribution of the drift forces has a strong inverse relation with the wave length. This, however, is not a completely correct conclusion because the wave amplitude is taken constant and the wavelength is varied in the studies. As a result, the wave steepness in increased. According to Kim et al. (2020) the magnitude of wave drift forces and moments are strongly dependent on this.

The evaluation of the capability of the different studies is difficult as the methods are validated on different ship models: Skejic & Faltinsen (2008) validated with the calm water results of the Mariner and the Esso Osaka, Wicaksono & Kashiwagi (2018) used the SR-108 container ship model, and the S-175 containership is used by Seo & Kim (2011) and Zhang et al. (2017). Furthermore, the ship speeds and wave conditions are all different in the experiments. Thereof, the relative comparison of the methods, can only be on a qualitative level, see figure 5 below. For this comparison, the turning trajectories starting in head waves with the same ratio of wave length over ship length is chosen. It can be seen that all methods predict the advance and the transfer distance good compared the model experiment data; which are the distances between the moment the rudder is given an angle and the distant travelled in longitudinally and transversely till the new heading is perpendicular to the initial heading. However, the numerical results with the drift forces from the New Strip Method of Wicaksono & Kashiwagi (2018) show deviations which are explained due to an inaccuracies in the drift force computations. For all studies, the numerical results start to deviate from half a turning cycle. Following

the reasoning of Kim et al. (2020), the drift is defined as the vector between the positions that the ship has turned 360^0 and 720^0, see figure 6 below, because the drifting distance is converged after 270^o. As a consequence, all studies are acceptable to model the general behaviour.

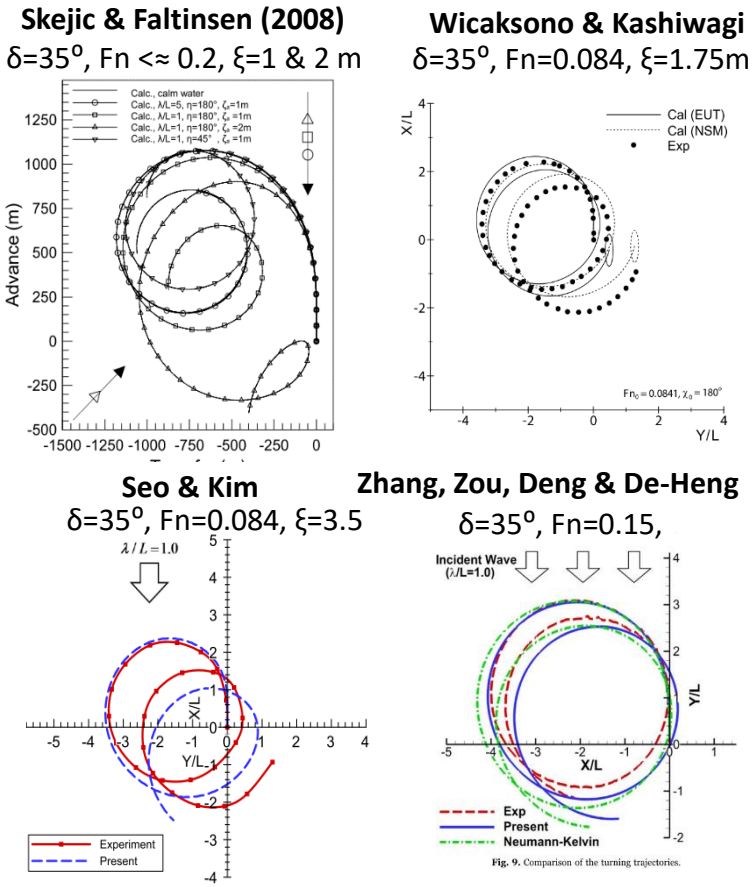

Figure 5: Comparison of the turning trajectories predicted in regular head waves by the different studies. The comparison is difficult because the methods use different model tests at different speeds. Skejic and Faltinsen (2008) used the Esso Okasa, but did not describe the model size. According to the ITTC (2002) *20 model test with different sizes between 1.650m and 8.125m were used for this benchmark study, so the Froude number cannot be verified. Seo & Kim and Zhang, Zou, Deng, and De-Heng used both the S175 container model. Lastly, Wicaksono and Kashiwagi used the SR108 container ship.*

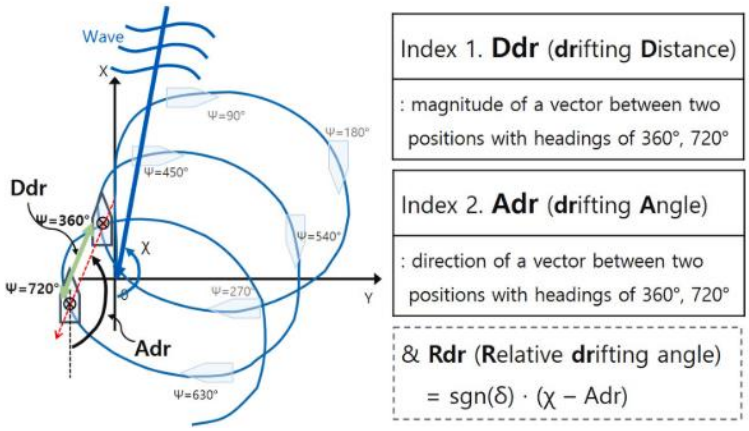

Figure 6: Definition of drift distance and angle in waves (Kim et al., 2020) *. Note that χ is the incoming wave angle and δ is the rudder angle.*

3.1.3 Unified Approach

The unified approach refers to an approach where fluid effects of the manoeuvring and seakeeping motions are simultaneously solved in a generic set of rigid body motion equations (Tello Ruiz et al., 2012). Hence, the physics of the hydrodynamic forces are more consistently included in the unified approach. Likewise the two time-scale approach, the method is modular and the rudder and propeller forces are superimposed in the time domain. The first successful attempts is published by Bailey et all. (1998) with the convolution integral approach of Cummins (1962) (Skejic, 2013). Latter similar studies are conducted by Ayaz et al. (2006), Fossen (2005), Pérez Arribas (2007), and (Tello Ruiz, 2018). All these studies are performed in order to develop the method and the focus is on validation.

Cummins (1962) was the first to apply the motion impulse function on seakeeping theory and derived a linear 6 degree motion equation in time domain. The ship is subjected to a small displacement x_j of constant velocity in an arbitrary direction, i.e. surge, sway, etcetera, over a short period of time Δt. Thereof, the flow is described with a normalized potential ψ_j that is proportional to the impulse velocity during the impulse. After the impulse interval, the ship motion stops abruptly, but the fluid is energized. The generated waves at the free surface will radiate and dissipate the impulse energy. This decaying wave motion is described in a second normalized velocity potential φ_j. As a consequence, the impulsive displacement influences the motions of the fluid during the interval and at all later times. Contrary, the motion is influenced by the previously induced motions in the fluid, which is referred to as the memory (Journée & Massie, 2008). Thereof, the motions are considered as a continuous sequence of small impulses. The total potential Φ is for the j[th] motion:

$$\Phi = \dot{\mathrm{x}}\psi_\mathrm{j} + \int_{-\infty}^{t} \varphi_j(t-\tau)\dot{\mathrm{x}}_\mathrm{j}(\tau)\mathrm{d}\tau \qquad 3\text{-}1$$

This potential satisfies the free surface boundary condition (Cummins, 1962). The set of motion equations is found from integration of the dynamic pressure p over the wetted surface S. Subsequently, Cummins (1962) derived the motion equations of the ship subjected to wave exciting forces $f_k(t)$:

$$\sum_{j=1}^{6}\left[\left(M_j\delta_{jk} + A_{jk}\right)\ddot{x}_j + C_{jk}x_j + \int_{-\infty}^{t} K_{jk}(t-\tau)\dot{x}_j(\tau)d\tau\right] = F_k(t) \qquad 3\text{-}2$$

$$A_{\mathrm{jk}} = \rho\int_{\dot{S}} \psi_\mathrm{j}\,\boldsymbol{s}_\mathbf{k}\mathrm{dS} \qquad 3\text{-}3$$

$$\mathrm{K_{jk}}(\tau) = \rho\int_{\mathrm{S}}^{\partial} \frac{\partial\varphi_\mathrm{j}(\tau)}{\partial t}\mathbf{s}_\mathbf{k}\mathrm{dS} \qquad 3\text{-}4$$

Where m_j is the inertia in the j[th] mode, δ_{jk} is the impulse function ($\delta_{jk} = 1\ if\ j = k$ and $\delta_{jk} = 0\ if\ j \neq k$), a_{jk} is the added mass, K_{jk} is the retardation function, t is the time, τ is the reference point in time, c_{jk} the hydrostatic force, ρ the density of the water, $\boldsymbol{s_k}$ is the normal vector of the hull surface, and dS is an infinitesimal surface element.

The restoring force coefficients can be found from hydrostatic analysis. Nevertheless, the potentials need to be solved in order to find the added mass and damping coefficients and the retardation functions. Therefore, Oglivie (1964) adopted the added mass and damping coefficients from the existing frequency domain potential programs, and, developed the concept of forced oscillations (Fossen, 2011). In fact, Oglivie related the above time domain equation with the frequency domain added mass and damping coefficients by comparison of the time domain equation and the frequency motion equation:

$$\sum_{j=1}^{6}\left[-\omega^2\left(M_{jk} + A_{jk}\right) + i\omega B_{jk} + C_{jk}\right]\zeta_j = F_k \qquad 3\text{-}5$$

Therefore, the ship is forced to move in unit amplitude oscillations:

$$\boldsymbol{x}(t) = \boldsymbol{i} \cdot \cos(\omega t) \text{ where } \boldsymbol{i} \text{ is the unit vector.} \quad \text{3-6}$$

Firstly, the τ is replaced by $t - \tau$ and the integration boundaries, therefore, changed. Then a convenient form is obtained in matrix notation, to which is referred as the Cummins equation:

$$(M + A) \cdot \ddot{\boldsymbol{x}}(t) + \int_0^\infty K(\tau) \cdot \dot{\boldsymbol{x}}(t - \tau) \cdot d\tau + C \cdot \boldsymbol{x}(t) = \boldsymbol{F}(t) \quad \text{3-7}$$

Now by substitution of 3-6 in the Cummins equation 3-7 and the classical frequency equation 3-5, the following two equations are compared:

$$-\omega^2 \cdot \left\{(M + A) - \frac{1}{\omega} \cdot \int_0^\infty K(\tau) \cdot \sin(\omega\tau) \cdot d\tau\right\} \cdot \cos(\omega t) \quad \text{3-8}$$
$$-\omega \cdot \left\{\int_0^\infty K(\tau) \cdot \cos(\omega\tau) \cdot d\tau\right\} \sin(\omega t) + \{C\} \cdot \cos(\omega t) = \boldsymbol{F}(t)$$

$$-\omega^2 \cdot \{M + A(\omega)\} \cdot \cos(\omega t) \quad \text{3-9}$$
$$-\omega \cdot \{B(\omega)\} \cdot \sin(\omega t) + \{C\} \cdot \cos(\omega t) = \boldsymbol{F}(t)$$

From the comparison of the motion equations, it can be concluded that the hydrostatic coefficients are the same and that:

$$A(\omega) = A - \frac{1}{\omega}\int_0^\infty \mathrm{K}(\tau)\sin(\omega\tau)\mathrm{d}\tau \quad \text{3-10}$$

$$B(\omega) = \int_0^\infty K(\tau)\cos(\omega\tau)\mathrm{d}\tau \quad \text{3-11}$$

Thereof, equation 3-10 should be valid for all ω, and A is evaluated at infinity frequency from the application of the Riemann-Lebesgue lemma (Taghipour et al., 2008), i.e. $A = A(\infty)$. Moreover, the inverse Fourier transformation is taken of 3-11, and thereof, the retardation functions can be determined:

$$\mathrm{K}(t) = \frac{2}{\pi}\int_0^\infty B(\omega)\cos(\omega t)\mathrm{d}\omega \quad \text{3-12}$$

Thereof, the time domain radiation forces can be obtained from the frequency domain coefficients which can be provided by any diffraction panel code or strip theory.

The unified approach is a straight forward approach as the retardation functions can be provided by any diffraction code (Tello Ruiz, 2018). However, Skejic & Faltinsen (2008) argue that the method is linear, but that some of the first order quantities are integrated over the instantaneous wetted surface. Therefore, the second order wave drift force are considered partly. Accordingly, the authors conclude that second order convolutions integrals should be considered which is difficult in a combine seakeeping and manoeuvring study. However, it is possible to keep the left hand side of the motion equation 3-7 linear and to take the non-linear effects into account in the external force (De Jong et al., 2020; Fossen, 2005, 2011; Journée & Massie, 2008; Tello Ruiz, 2018). Thereof, also, the second order wave drift forces are included from potential considerations.

The second part of the criticism of Skejic & Faltinsen (2008) is that added mass and damping coefficients are encounter frequency dependent, and that the first order wave forces and moments have to be transformed via a Fourier transformation. All change with the encounter frequency, which change with as the heading and speed changes, and therefore; the impulse response functions need to be evaluated frequently. Consequently, the method is considered to be computational time consuming. This argument is, however, unjustified imbedded in literature from time to time, because the study of Skejic & Faltinsen (2008) focuses on real time simulations. If real time is no requirement, then the method is equally applicable as the two time-scale approach. Moreover, there exists different approaches that approximate the retardation functions; like the State Space representation and the

Prony's approximation. In the State Space representation is adopted by De Jong et al. (2020), Fossen (2011), and Tello Ruiz (2018). Therein, the convolution integrals are replaced by a system of ordinary differential equations which simplifies the numerical computation time. In Prony's method, the retardation functions are approximated with summations of exponential functions which also reduces the computational time significantly (Armesto et al., 2015).
Besides, real time simulations based on impulse response functions have been published by Bailey et al. (2002) for the same benchmark vessel the Mariner in similar conditions as in (Skejic & Faltinsen, 2006). The studies are compared in figure 7 below, and both results seem are similar accurate. Nevertheless, the comparison is difficult because the waves come from opposite directions.

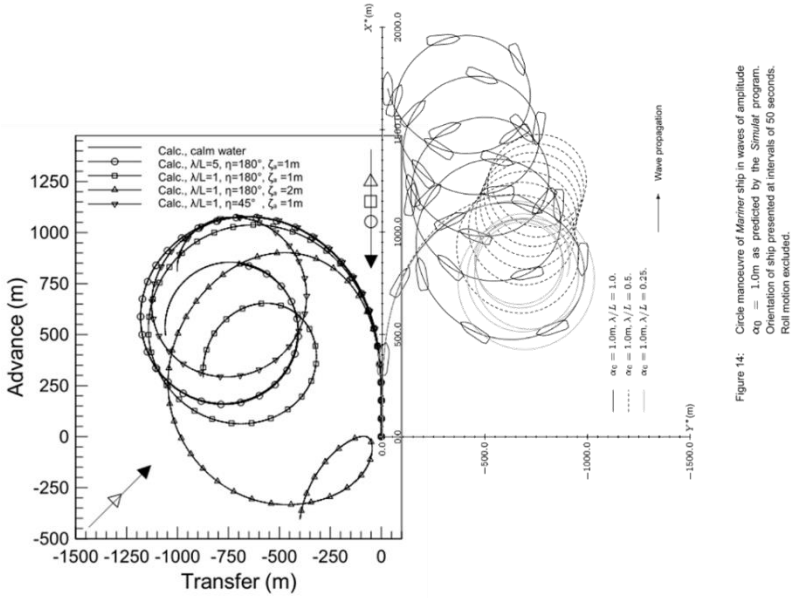

Figure 7A

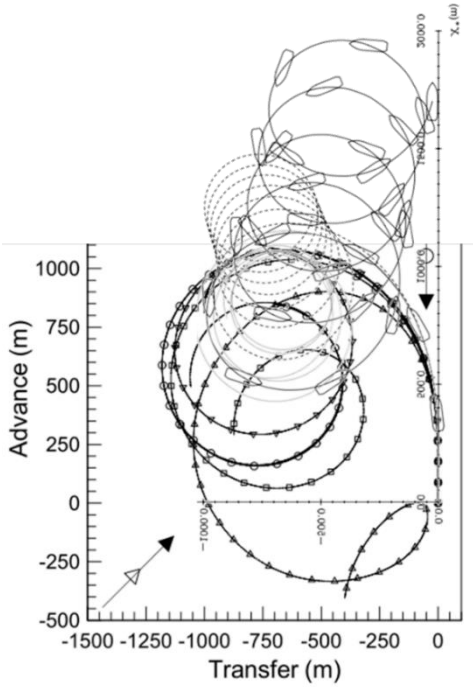

Figure 7B

Figure 7: Comparison of the circle trajectory of benchmark ship 'Mariner' in regular waves simulated with the unified approach and the two time-scale approach. In figure 7A the results are presented next to each other, and in figure 7B the results are placed on each other. Unfortunately, Skejic & Faltinsen (2006) *published the results for starting in head waves, while* Bailey et al. (2001) *published following seas.*

3.1.4 Comparison of Two Time-scale Approach and Unified Approach

From the above, the difficulty of the comparison between the two methods becomes clear. The unified appraoch is based on the Cummins equation and the wave influences are included consitently. The model is, however, more difficult in application due to the convolution integrals. Contrary, in the classification the two time-scale approach seems to be an engineering work-arround the convolution integrals by neglecting all wave influences except for the mean second order drift forces and yaw moment. The advantage of the two time scale approaches is claimed to be the high accuracy of the coupled manoeuvring and seakeeping theories. Nevertheless, no explaination or insight is provided in the seperate modules, to the knowlegde of the author.

3.2 Conclusion

The aim in this chapter was to obtain understanding on manoeuvring and seakeeping methods that combine the two From this literature study, the question can be answered: *"What methods in combined seakeeping and manoeuvring can be deployed?"*. This method or methods are found when the following criteria are fulfilled:

1. The method should improve the fidelity compared to the present wave forces in the manoeuvring model.
2. The method should be applicable in the framework of the present model.

Traditionally, seakeeping and manoeuvring theory are considered independently based on in-field observations, and well established methods exists. In manoeuvring theory the horizontal motions of a ship are considered and the viscous forces are described with hydrodynamical derivatives. The derivatives are obtained from model experiments. On the contrary, the viscous effects are neglected in seakeeping theory and the ship is assumed to sail in a straight course with constant velocity. Thereof, the ship is considered as a mass-spring system and transfer functions can be formulated to describe the system behaviour. By means of potential theory, the wave excitation, the radiation, and diffraction forces are found from frequency domain analysis. Moreover, the second order forces and moments can be found with the direct pressure method. These forces consist of a mean force component and a slowly oscillating force component. These second order forces contribute to course and velocity changes.

In the combination of seakeeping and manoeuvring theory, four approaches are distinguished to deal with manoeuvring in waves that are developing; experimental approaches, unified theory, two time-scale approaches, and CFD. Experiments are mainly conducted to measure the hydrodynamic derivatives for the manoeuvring motion equation, or to have a benchmark to validate a numerical study to. Moreover, the hull geometry is unknown and therefore it does not make sense to perform costly experiments. The computational methods and power need further developments in order to simulate a ship manoeuvring in waves. Therefore, CFD is presently useful in order to estimate the hydrodynamic derivatives and can be seen as a digital experiment. Thereof it is concluded that these two methods do not satisfy the applicability criterion. The two time-scale- and unified methods do satisfy the criterion. Both methods employ the modular approach from manoeuvring theory to incorporate the hydrodynamic, rudder, propeller forces in the motion equations.

In the two time-scale approach, the hydrodynamic forces corresponding to manoeuvring and seakeeping theory are further separated. The main assumption is that the manoeuvring forces act on a slower time scale than the seakeeping forces. Thereof, the two motion equations are solved in separate modules that are weakly coupled with the transfer of data from the manoeuvring problem to the seakeeping problem and vice versa in a series or parallel model. The main advantage of the approach is that for both problems, the most accurate methods can be deployed. Especially, the studies in literature differ mostly in the accuracy of the second order wave drift forces. The comparison of the different

methods in the studies of this approach is difficult due to the few benchmark measurements in waves. All studies are conducted on different ships and at different speeds. Nevertheless, all authors conclude that the results are reasonably satisfactory.

On the contrary, the unified approach incorporates the seakeeping and manoeuvring theory into one single set of motion equations and a more physical consistent model is obtained. The fundament is the Cummins equation which is a time domain motion equation that is derived from the impulse response functions. Thereof, the ship is assumed to have an arbitrary impulse over a short period of time. Consequently, motions are induced in the fluid which do not vanish when the impulse is abruptly stopped. This fluid motions influence the ship motions in the subsequent time steps and vice versa. This difficult behaviour is captured in the retardation functions. Ogilvie developed a method to relate these retardation function with the frequency domain coefficients from seakeeping analysis. Nevertheless, the retardation functions needs to be computed. Therefore, the functions can be computed directly, an alternative state space representation can be given, or approximated with the Prony's coefficients. In most unified studies, the second order wave drift forces are included partly as the first order forces are integrated to the instantaneous waterline. Only few studies included the mean second order forces and moments. Nevertheless, a more physically based simulation can be obtained with this method.

From the section above, it can be concluded that the two time-scale approaches and the unified approach can be deployed in this study. In the two time-scale approaches, the two seakeeping and manoeuvring theory are artificially coupled. The main advantage of this separation is that accurate models of both disciplines can be used without limitations. As a consequence, the selection of the methods seem to be based on availability and not suitability. The unified approaches strive to a incorporate the fluid forces of the manoeuvring and seakeeping motions in a generic set of rigid body motion equations. Hence, the physics of the hydrodynamic forces are more consistently included in the unified approach. The main points of criticism are that the frequent evaluation of the convolution integrals is time consuming, and that the second order forces are only partly included. Multiple studies in literature prove that these criticisms easily can be refuted by the application of a state space approximation (Armesto et al., 2015; Fossen, 2005). Consequently, it is concluded that a unified approach is most suitable to be deployed to enhance the veracity of the simulation.

4 Unified Model

As mentioned in the introduction, the ultimate objective is to obtain insight in the required minimum power to maintain manoeuvre capabilities of the tanker in adverse weather conditions. As part of this research, the main aim in this study is to develop a method to improve the fidelity of the wave influences on the ship hull in the original manoeuvring model of the Castillo de Tebra. Presently, the hull forces are modelled with the Kijima model and the time averaged steady wave forces are taken into account as tabular coefficients of a VVLC tanker. Moreover, the hull geometry is unknown and the ship will be modelled as a barge in the calculation of the wave forces on the hull.

Traditionally, manoeuvring- and seakeeping theory are treated separately. However, the study in chapter 3.1 showed that four approaches are distinct that merge the two disciplines, and, it is concluded that the two time-scale approaches and the unified approach are applicable in this study. In the two time-scale approaches, the two seakeeping and manoeuvring theory are artificially coupled in different models that exchange data. The main advantage of this separation is that accurate models of both disciplines can be used without limitations. As a consequence, the selection of the methods seem to be based on availability and not suitability. The unified approaches strive to an amalgamation of the manoeuvring and seakeeping motions in a generic set of rigid body motion equations. Hence, the physics are more consistently included in the unified approach. Therefore, it is chosen to establish a unified approach to include the wave forces in the manoeuvring model.

Subsequently, this chapter will introduce the unified approach. The method is inspired on the work of de Jong (2018), Fossen (2005), Perez & Fossen (2009), and Tello Ruiz (2018). Furthermore, the Marine Systems Simulator (MSS) developed by Fossen, T & Perez (2021) is consulted. The MSS is a Matlab and Simulink library for marine systems and contains methods and algorithms for hydrodynamic models for ships, underwater vehicles, and floating structures, and, guidance, navigation, and control (GNC) blocks for real-time simulation. The methods and algorithms are described in Fossen (2011). As mentioned in section 3.1.3, the input for the time domain radiation problem can be obtained from the frequency domain. Therefore, a diffraction analyses is executed in ANSYS AQUA.

4.1 Diffraction Analysis in Ansys Aqwa

The time domain model is associated with the frequency domain model. As illustrated in section 3.1.3, the frequency dependent added mass and damping coefficients can be used to approximate the convolution integrals for the time domain radiation problem. Therefore, any diffraction code or strip method can be used. The diffraction analyses in this study is executed in ANSYS AQUA due to the available licence at the Technical University Delft. The theory of the solver is well described in ANSYS Inc. (2016), Fossen (2011), and Journée & Massie (2008). The diffraction analysis is based on potential flow. Hence, the fluid is assumed to be irrotational and non-viscous. From the diffraction analysis, the frequency dependent added mass and damping coefficients and the infinity frequency added mass coefficients are obtained which will be used in the radiation forces, see section 0. Furthermore, the force response operators (RAO) and the quadratic transfer functions (QTFs) are obtained for the wave excitation forces, see section 4.4.

The main input to the diffraction analysis are a description of the hull geometry and the mass properties of the ship. However, these are to a large degree unknown for the benchmark tanker. Therefore, the ship will be modelled as a barge with the same dimensions as the tanker, see table 2 and figure 8 below.

Table 2: A selection of the known main particulars of the Castillo de Tebra (Sui, 2021) .

Particular	Symbol	Value
Length between perpendiculars	L_{pp}	$113.8m$
Beam	B	$22m$
Draught	d	$8.5m$
Molded depth	D	$11.4m$
Displacement	∇	$16998\ m^3$
Centre of floatation w.r.t. midship($L_{pp}/2$)	x_g	$1.698m$

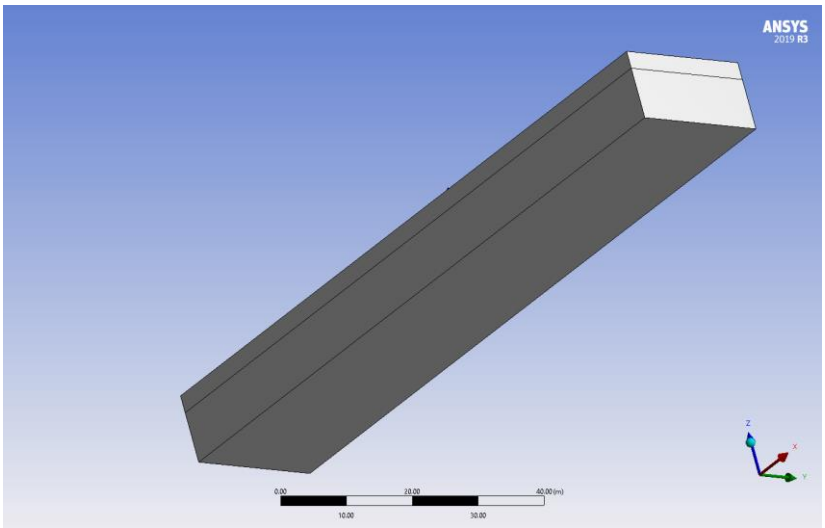

Figure 8: The geometry of barge model in Ansys Aqwa with a length of 113.6 meters, a beam of 22 meters, a draught of 8.5 meters, and a depth of 11.4 meters.

The mass is found from the provided displacement and the moments of inertia are estimated from the provided radii of gyration of the ITTC (2014) recommendations. The advised radius of gyration is for roll $0.4B$ and for pitch and yaw $0.25L_{pp}$. This assumption for yaw is in agreement with the assumption made by Sui (2021).Thereof, the mass matrix is:

$$M_{RB} = \begin{bmatrix} m & 0 & 0 & 0 & 0 & 0 \\ 0 & m & 0 & 0 & 0 & 0 \\ 0 & 0 & m & 0 & 0 & 0 \\ 0 & 0 & 0 & 0.4B & 0 & 0 \\ 0 & 0 & 0 & 0 & 0.25L_{pp} & 0 \\ 0 & 0 & 0 & 0 & 0 & 0.25L_{pp} \end{bmatrix} \quad 4\text{-}1$$

These mass properties are assigned to the barge model as a point mass. Therefore, the centre of gravity is required. Contrary to the real ship, the centre of floatation of the barge is assumed to be midship to avoid trim of the barge. According to Papanikolaou (2014) and Schneekluth & Bertram (1998), the height of centre of mass $\overline{KG}$ is estimated with:

$$\overline{KG} = C_{KG}\,(D + \frac{\nabla_A + \nabla_{DH}}{L_{pp}B}) \quad 4\text{-}2$$

Where C_{KG} is a coefficient that relates $\overline{KG}$ to the depth and ∇_A and ∇_{DH} are the volume of the superstructures and the deckhouse, respectively. As mentioned by the authors, the coefficient is varying for different ship types and for tankers the coefficient is varying between 0.52 and 0.54. Due to size effects, the light weight to displacement ratio of smaller tankers is relatively larger and therefore the coefficient is chosen 0.54 in this study. The volumes of the super structure and the deck house are estimated based on dimension ratios, see figure 9 and figure 10. The deck heights of the deckhouse and the forecastle height are assumed to be $2.5m$.

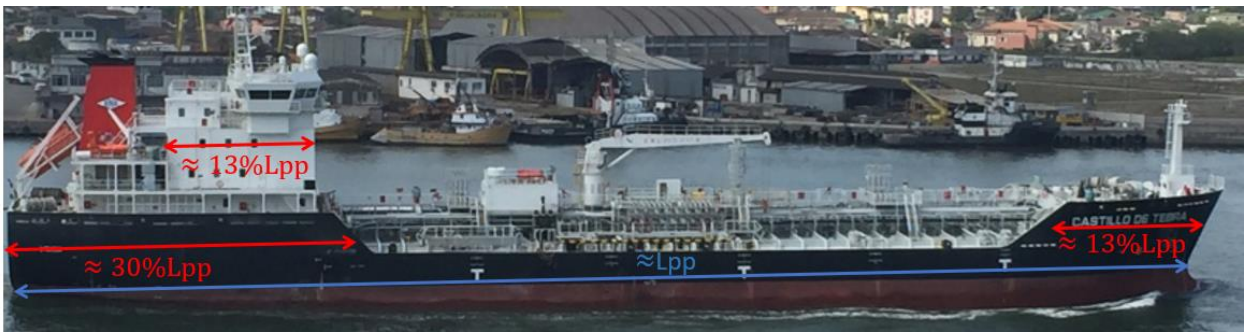

Figure 9: Side view of the ship with size estimations of the superstructures and deckhouse based on the Lpp (https://www.shipspotting.com/photos/2734272?navList=moreOfThisShip&imo=9753636&lid=2738636).

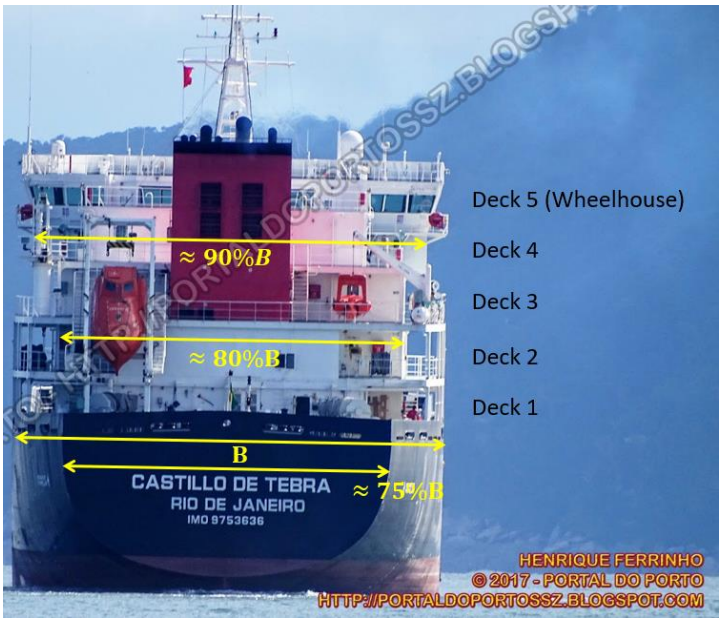

Figure 10: Back view of the ship with the estimations of the superstructure widths of the poop deck and deckhouse.

With the geometry and mass properties defined, the mesh of the model is generated. For the element size of the mesh should be one-seventh of the smallest wave length (Ibinabo & Tamunodukobipi, 2019). For wind generated waves with a typical wave period between 0.5 and 10 seconds, the minimum wave length from the dispersion relation in deep water is roughly 0.4 meters (Vinet & Zhedanov, 2011). Therefore, the element size of the mesh should be 0.055m. Unfortunately, the maximum of 40000 elements is exceeded and therefore the element size is increased at the cost of some information in the high frequency. Nevertheless, the ship responses are dominated by the ships mass and the influences are small.

Subsequently, a mesh with 6120 and 23140 elements are compared in deep water. The frequency domain analysis is executed for 37 directions from -180 till 180 degrees and for 50 frequencies from 0.06 till 2.70 radians per seconds. For Ansys Aqwa the hull should be closed and therefore, the former has 3628 and the latter 13840 diffracting elements (below the waterline). The added mass and damping coefficients, and the force RAOs are provided in figure 12 to figure 17. Note that the results of the finer mesh continuous to higher frequencies. Furthermore, the lines are smooth with some small disruptions for the pure motions. Hence, the results seem to be converged although the small outliers disappeared in the higher frequency for the finer mesh.

Most coupling terms are fiercely fluctuating and are small except for the surge-pitch and sway-yaw couplings that have significant contributions. From the force RAO figures, it can be seen that the results are divided in some local optima. The reason might be that a certain number of wave lengths of a wave of a certain direction and frequency correspond to a main dimension of the ship. The resultant force of the pressure around the hull is then zero.

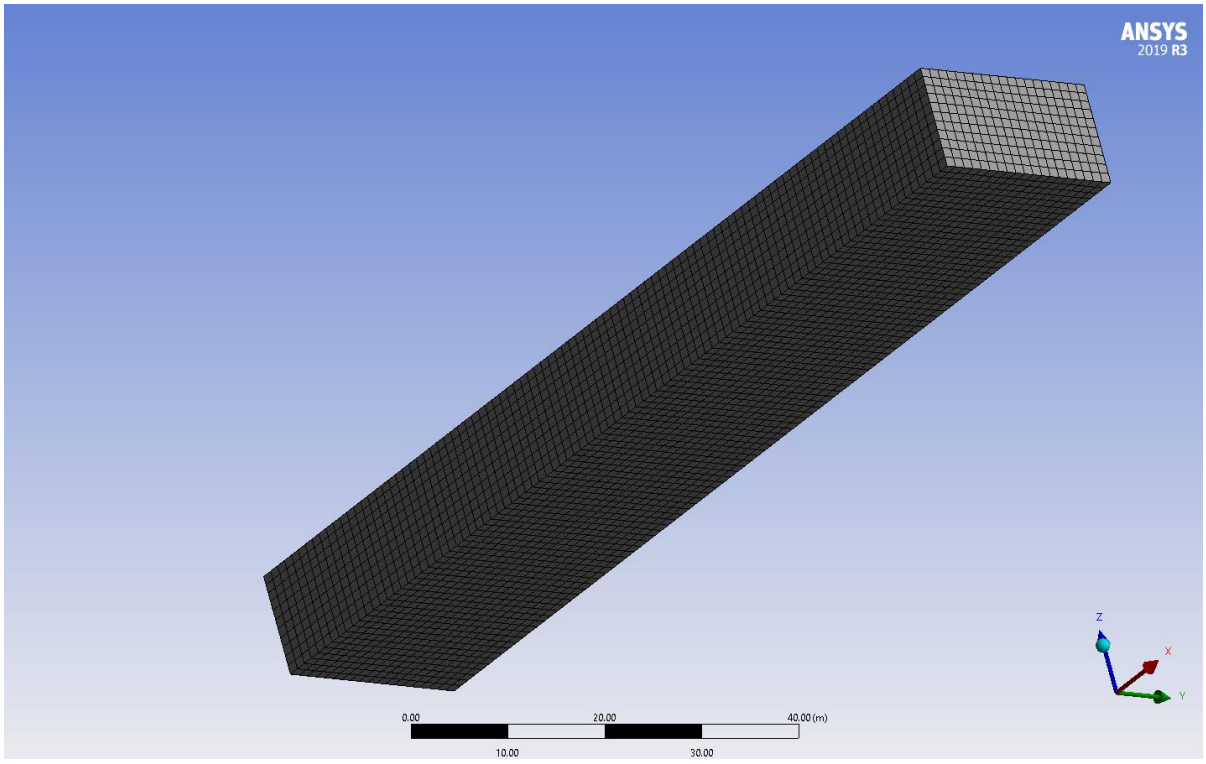

Figure 11: Mesh of the barge model with 6120 elements of which 3629 diffracting. The elements have a maximum of 2 meters.

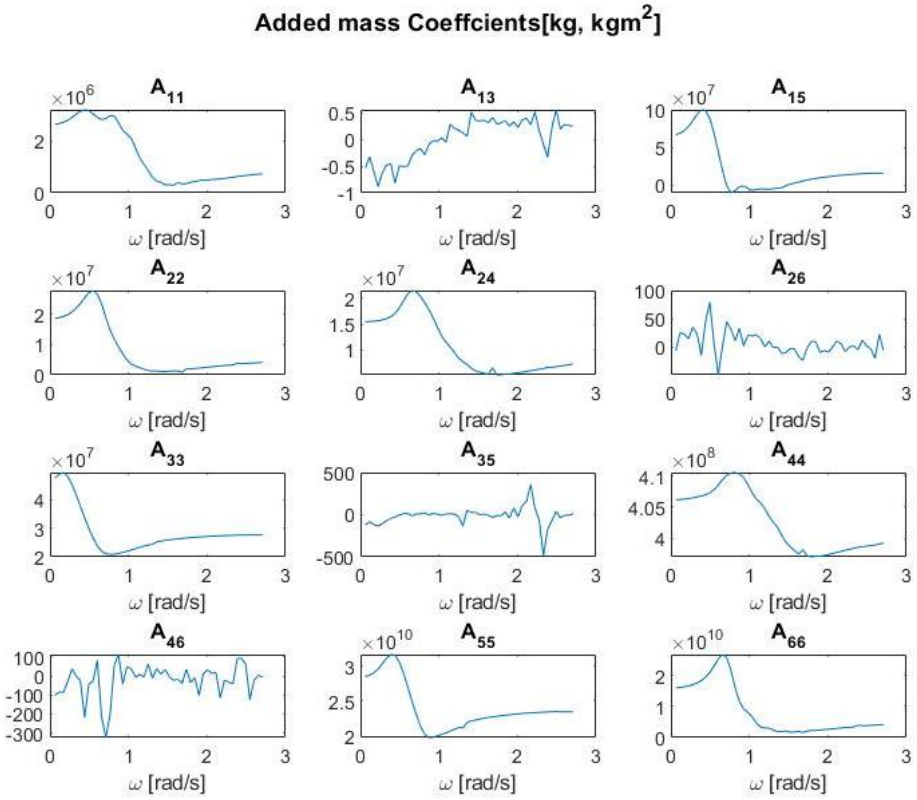

Figure 12: Added mass coefficients for the mesh with mesh 3629 diffracting elements.

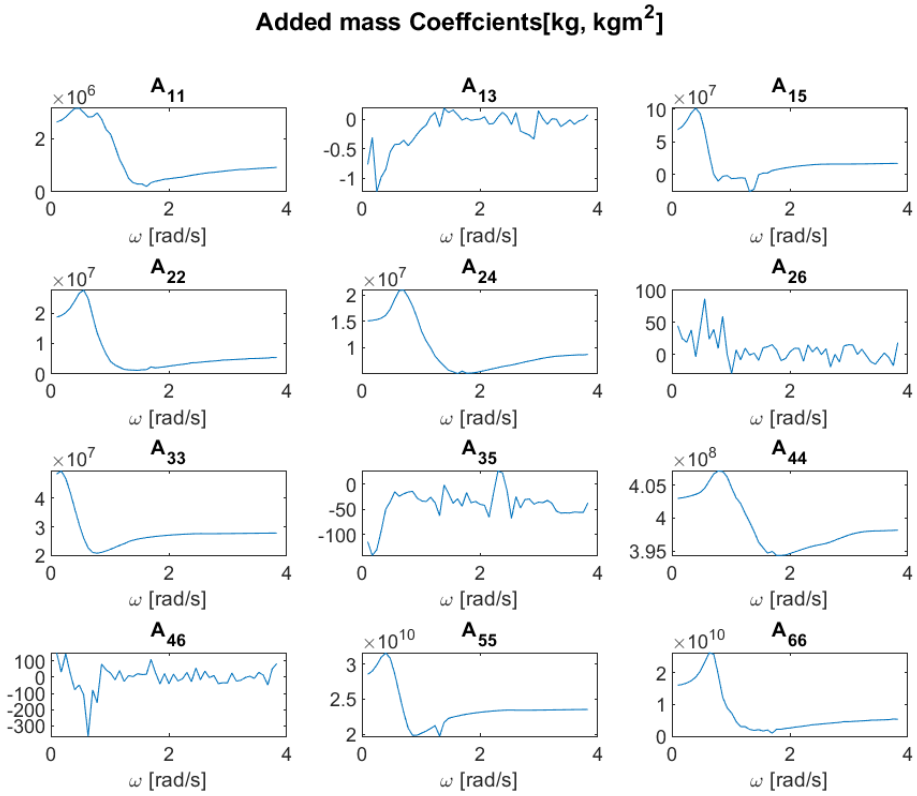

Figure 13: Added mass coefficients for the mesh with mesh 13840 diffracting elements.

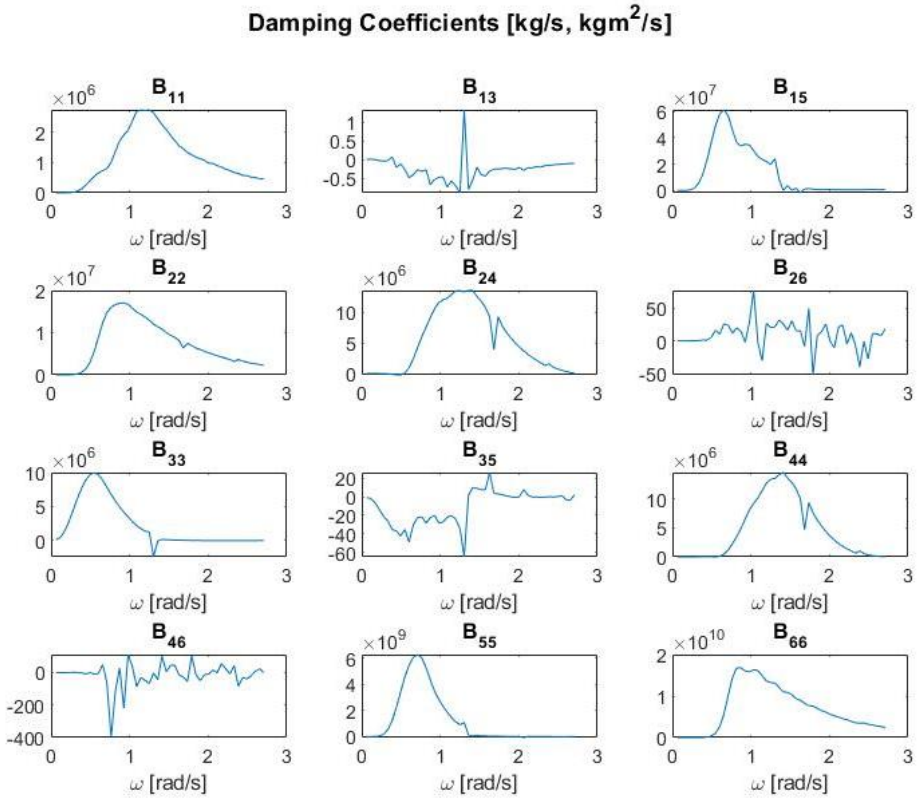

Figure 14:Damping coefficients for the mesh with mesh 3629 diffracting elements.

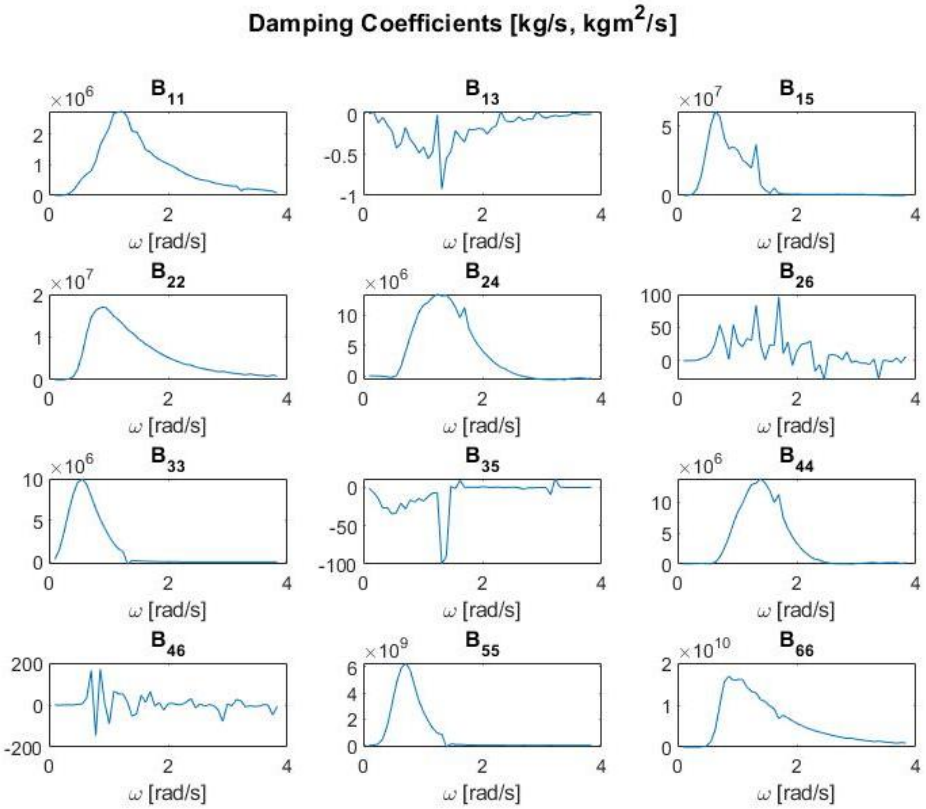

Figure 15: Damping coefficients for the mesh with mesh 13840 diffracting elements.

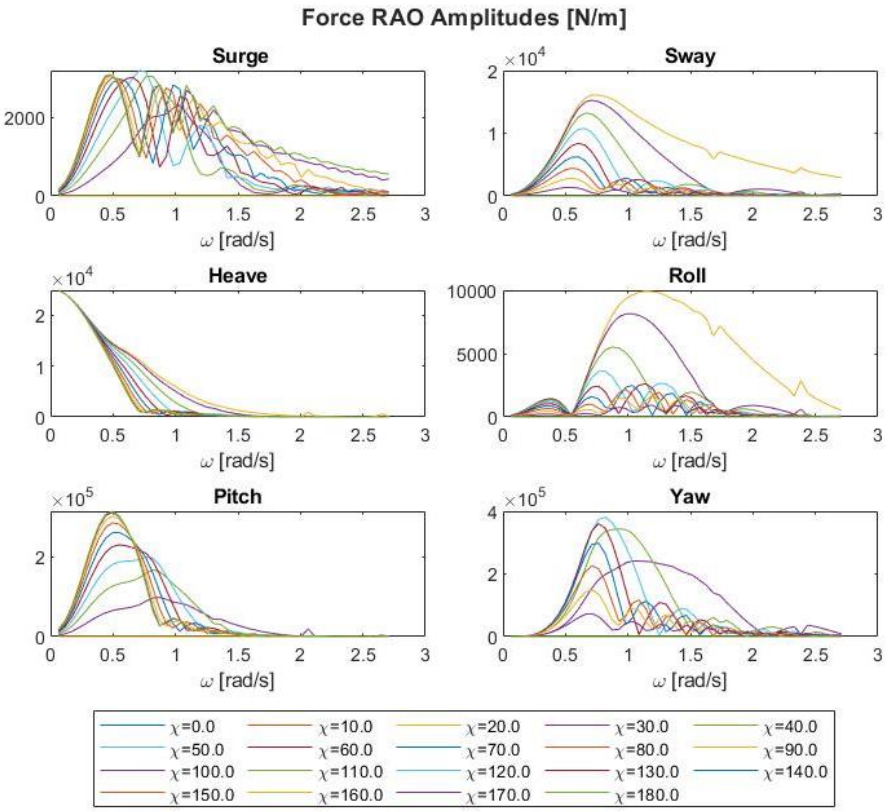

Figure 16: Force RAO for the mesh with mesh 3629 diffracting elements.

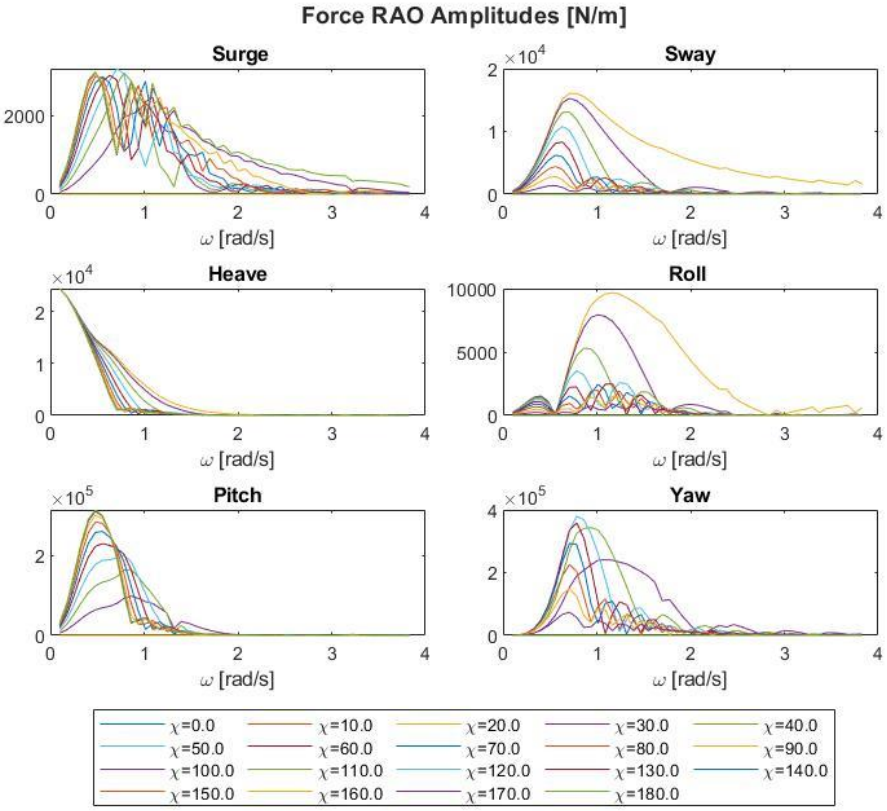

Figure 17: Force RAO for the mesh with mesh 13840 diffracting elements.

4.2 Unified Motion Equation

The original manoeuvring model contains the typical manoeuvring reference systems, see section 2. As only the horizontal, surge, sway, and yaw, motions are included, the equation of motion is expressed using a Newtonian and a body fixed reference frame, see figure 18 and figure 19. The North-East-Down reference frame is Earth fixed and indicated with (X_0, Y_0, Z_0). In the ships centre of gravity, a body fixed coordinate system (x_b, y_b, z_b) translates with the centre of gravity and rotates with the heading of the ship (Sui, 2021).

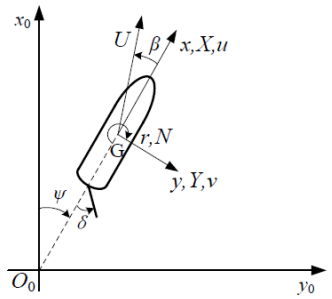

Figure 18: The reference systems in the manoeuvring simulation (Sui, 2021).

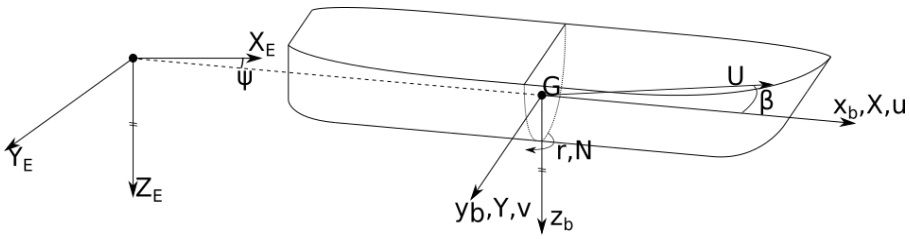

Figure 19: A 3D-representation of the Earth fixed reference system (E-frame) and the b-frame as adopted in the Kijima model.

In the model, the ship is assumed to be a rigid body and the origin of the body fixed reference frame is in the centre of gravity. According to Tello Ruiz (2018), the motion equation of marine structures can expressed in the body fixed frame as:

$$\boldsymbol{F} = \begin{cases} m(\dot{u} - vr + wq) \\ m(\dot{v} - wp + ur) \\ m(\dot{w} - uq + vp) \\ I_{xx}\dot{p} \\ I_{yy}\dot{q} \\ I_{zz}\dot{r} \end{cases} \qquad 4\text{-}3$$

In which, m, I_{xx}, I_{yy}, and I_{zz} are the rigid body mass and mass moments of inertia of the vessel, which follow from equation 4-1, x, v, w, p, q, and r are the ship and rotational velocities. The force vector $\boldsymbol{F}$ contains the fluid forces on the ship. Following the modular approach, see sections 3.1.2 and 3.1.3, these forces are assumed to be a superposition of the hydrodynamic forces on the hull F_H, the rudder forces F_R, the propeller forces F_P, and the environmental forces from waves F_W and wind F_A. Thereof, in vector representation, equation 2-7 can be represented as:

$$\boldsymbol{F} = \boldsymbol{F_R} + \boldsymbol{F_P} + \boldsymbol{F_A} + \boldsymbol{F_H} + \boldsymbol{F_W} \qquad 4\text{-}4$$

The wind, rudder and propeller models are presently implemented and are not considered in this study. Likewise, the implemented forces from the Kijima will be unaltered and the details on these models can be found in Kijima et al. (2004) and Sui (2021). Hence, the focus in this study is to improve the fidelity of hull forces and the wave excitation forces.

Tello Ruiz (2018) has demonstrated with model experiments that the steady hull forces measured in calm water differ to some extent to the hull forces in waves. Therefore, the forces can satisfactory be estimated by considering the viscous manoeuvring forces and wave induced forces independently. This method is supported by Fossen (2005) who sets the zero-frequency added mass and damping coefficients as the first order hydrodynamic derivatives, and mentions that the higher order force terms can be superimposed directly in the time domain. Therefore, the hull forces are decomposed in steady and an ideal force component:

$$\boldsymbol{F_H} = \boldsymbol{F_v} + \boldsymbol{F_{rad}} + \boldsymbol{F_{res}} \tag{4-5}$$

The steady contribution $\boldsymbol{F_v}$ comprises the viscous, cross flow, and lift forces on a manoeuvring ship. These forces on the hull are approximated with the Kijima model and are implemented in the original model (Sui, 2021). The origin of these forces is provided in section 2. The radiation force contribution $\boldsymbol{F_{rad}}$ originate from the body reaction forces due to the oscillatory motions of the ship in an ideal fluid. These forces will be taken into account based on the Cummins equation to include the memory effects:

$$\boldsymbol{F_{rad}} = -A_\infty \ddot{\boldsymbol{X}} - \int_0^t K(t-\tau)\dot{\boldsymbol{X}}(\tau)dt \tag{4-6}$$

$$\mathrm{A}_\infty = \begin{bmatrix} a_{11} & 0 & a_{13} & 0 & a_{15} & 0 \\ 0 & a_{22} & 0 & a_{24} & 0 & a_{26} \\ a_{31} & 0 & a_{33} & 0 & a_{35} & 0 \\ 0 & a_{42} & 0 & a_{44} & 0 & a_{46} \\ a_{51} & 0 & a_{53} & 0 & a_{55} & 0 \\ 0 & a_{62} & 0 & a_{64} & 0 & a_{66} \end{bmatrix} \tag{4-7}$$

$$\mathrm{K} = \begin{bmatrix} k_{11} & 0 & k_{13} & 0 & k_{15} & 0 \\ 0 & k_{22} & 0 & k_{24} & 0 & k_{26} \\ k_{31} & 0 & k_{33} & 0 & k_{35} & 0 \\ 0 & k_{42} & 0 & k_{44} & 0 & k_{46} \\ k_{51} & 0 & k_{53} & 0 & k_{55} & 0 \\ 0 & k_{62} & 0 & k_{64} & 0 & k_{66} \end{bmatrix} \tag{4-8}$$

The infinity added mass matrix A_∞ is computed with Ansys Aqwa and the convolution matrix $K(t-\tau)$ will be taken int account with a steady state approximation based on the damping coefficients obtained from Ansys Aqwa. A more elaboration on the state space approximation is provided in section 4.3.

The restoring forces $\boldsymbol{F_{res}}$ follow the hydrostatic and are provided as output from Ansys Aqwa.

$$\boldsymbol{F_{res}} = -C\boldsymbol{X}, \qquad C = \begin{bmatrix} 0 & 0 & 0 & 0 & 0 & 0 \\ 0 & 0 & 0 & 0 & 0 & 0 \\ 0 & 0 & c_{33} & 0 & 0 & 0 \\ 0 & 0 & 0 & c_{44} & 0 & 0 \\ 0 & 0 & 0 & 0 & c_{55} & 0 \\ 0 & 0 & 0 & 0 & 0 & 0 \end{bmatrix} \tag{4-9}$$

Lastly, the wave forces $\boldsymbol{F_W}$ are pressure forces on the ship due to waves, and, are decomposed in the Froude-Krylov force $\boldsymbol{F_{FK}}$, the diffraction force $\boldsymbol{F_D}$ and the second order wave forces $\boldsymbol{F_{2nd}}$.

$$\boldsymbol{F_W} = \boldsymbol{F_{FK}} + \boldsymbol{F_D} + \boldsymbol{F_{2nd}} = \boldsymbol{F_{FK,D}} + \boldsymbol{F_{2nd}} \tag{4-10}$$

These forces are computed with the force RAOs and the QTFs obtained from Ansys Aqwa. In the force RAO output the Froude-Krylov and diffraction effects are combined and therefore these forces are included in one term. More details on the wave force model follows in section 4.4. Eventually, the unified motion equation follows from the substitution of all the above in equation 4-3

In order to make the unified motion equation consistently, care must be given a transformation is needed of the obtained data from Ansys Aqwa. It can be noticed in figure 20 below, that the reference conventions of Ansys Aqwa make use of an upward z-axis whereas the Kijima model uses a downward axis figure 19. Besides this, there are no differences and therefore the models only differ a 180 degree rotation about the x-axes of the body frame. Therefore, the sway and the roll motions and forces remain the same, but are negative for sway, heave, pitch and yaw. Consequently, the generalized transformation matrix is:

$$T = \begin{bmatrix} 1 & 0 & 0 & 0 & 0 & 0 \\ 0 & -1 & 0 & 0 & 0 & 0 \\ 0 & 0 & -1 & 0 & 0 & 0 \\ 0 & 0 & 0 & 1 & 0 & 0 \\ 0 & 0 & 0 & 0 & -1 & 0 \\ 0 & 0 & 0 & 0 & 0 & -1 \end{bmatrix} \qquad 4\text{-}11$$

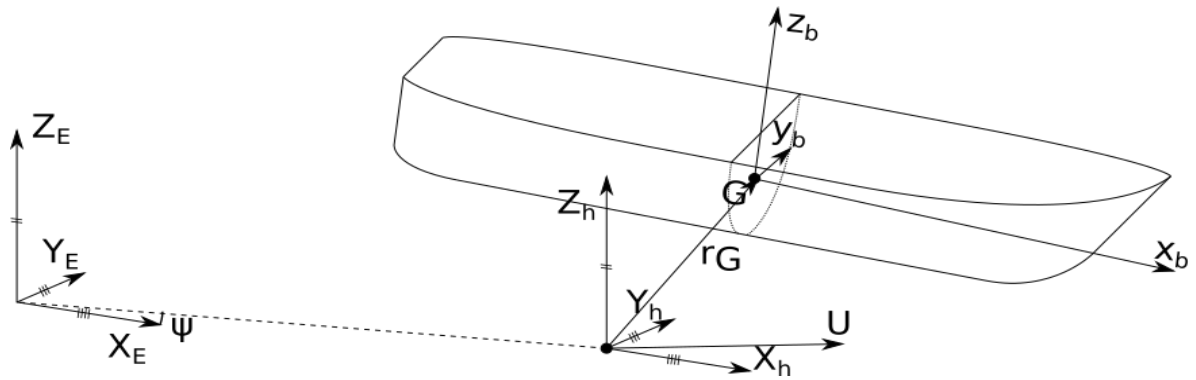

Figure 20: A 3D-representation of the coordinate systems adopted in ANSYS AQWA Notice that the position of the origin of the b-frame with respect to the origin of the h-frame are the surge, sway, and heave motions r̄_G=[ξ_1 ξ_2 ξ_3]. The differences in the orientations of the corresponding axes are the roll, pitch, and yaw motions $[\xi_4\ \xi_5\ \xi_6]$.

4.3 Parametric Identification of the Radiation Force Model

As shown in section 3.1.3 and 4.2, the radiation forces in the time domain can be represented into account based on convolution integrals of the Cummins equation, see equation 3-7. The radiation force contribution $\boldsymbol{F_{rad}}$ originate from the body reaction forces due to the oscillatory motions of the ship in an ideal fluid:

$$\boldsymbol{F_{rad}} = -A_{\infty}\ddot{\boldsymbol{X}} - \int_0^t K(t-\tau)\dot{\boldsymbol{X}}(\tau)d\tau \qquad 4\text{-}12$$

The infinity added mass A_{∞} is obtained from the diffraction analysis in Ansys Aqwa but the direct evaluation of convolution matrix $K(t-\tau)$ is more difficult. Generally, the terms of the convolution matrix are referred to as the retardation functions, fluid memory effects, or impulse response functions. For every time step in a simulation, the integrals needs to be evaluated and therefore the method is considered time and memory consuming (Taghipour et al., 2008). Therefore, the direct computation is circumvented with an approximation of the impulse response functions with state space representation or a sum of complex exponential functions using Prony's method (Armesto et al., 2015). The former will be applied in this study because method seem to be generally adapted in literature due to the computational performance in the time domain. Subsequently, the parametric identification method of Perez & Fossen (2009) is embedded which is included in the Marine Systems Simulator (Fossen, T & Perez, 2021). Hence, the convolution integral will be approximated with state space approximation:

$$\boldsymbol{\eta}(t) = \int_0^{\infty} \mathrm{K}(t-\tau)\dot{\boldsymbol{X}}(\tau)d\tau \approx \begin{matrix} \mathbf{x}(t) = \hat{A}\mathbf{x}(\mathrm{t}) + \hat{B}\dot{\mathbf{x}}(t) \\ \hat{\boldsymbol{\eta}}(t) = \hat{C}\mathbf{x}(t) \end{matrix} \qquad 4\text{-}13$$

In which, $\mathbf{x}$ is the state vector, $\dot{\boldsymbol{X}}$ the input vector, $\hat{A}$ is the state matrix, $\hat{B}$ the input matrix, $\hat{C}$ the output matrix, and $\hat{\boldsymbol{\eta}}$ the output vector of the state-space that approximates the convolution integral.

The basis for the identification method is the comparison of Oglivie (1964) of the Cummings equation and motion equation in the frequency domain:

$$[-\omega^2[\mathrm{M} + \mathrm{A}(\omega)] + i\omega\mathrm{B}(\omega) + \mathrm{G}]\boldsymbol{X}(i\omega) = \boldsymbol{\tau}_{exc}(i\omega) \qquad 4\text{-}14$$

From the comparison Oglivie obtained from a Fourier transformation the following equations:

$$A(\omega) = A_{\infty} - \frac{1}{\omega}\int_0^{\infty} \mathrm{K}(\tau)\sin(\omega\tau)\mathrm{d}\tau \qquad \textit{Repetition of 3-10}$$

$$B(\omega) = \int_0^{\infty} K(\tau)\cos(\omega\tau)\mathrm{d}\tau \qquad \textit{Repetition of 3-11}$$

The Fourier transform of Repetition of 3-11 can be used for the direct computation of the impulse response function. Moreover, the frequency domain representation of the retardation functions is derived from the substitution of 3-10 and 3-11:

$$\mathrm{K}(i\omega) = \int_0^{\infty} \mathrm{K}(\tau)\mathrm{e}^{-i\omega\tau}\mathrm{d}\tau = \mathrm{B}(\omega) + i\omega[\mathrm{A}(\omega) - \mathrm{A}(\infty)] \qquad 4\text{-}15$$

Thereof, the impulse response functions can be computed with the added mass and damping coefficients obtained from Ansys Aqwa, see section 4.1. This result is of utmost importance in identification problems as the fluid memory will be approximated with transfer functions.

For linear time-invariant systems, the state space representation 4-30 is restated in the frequency domain:

$$\mathrm{K}(\mathrm{j}\omega) \approx \hat{K}(s) = \hat{C}\left(i\omega I - \hat{A}\right)^{-1}\hat{B} \qquad 4\text{-}16$$

Where $\hat{K}(s)$ is a matrix containing transfer functions.

The identification problem focusses on approximating these transfer functions and to obtain the state space model with canonical realisations (Perez & Fossen, 2009; Taghipour et al., 2008).The main assumption to use the canonical realization is that the transfer function is strictly proper. Therefore, the transfer functions are expressed as a parametric functions with a relative degree of one:

$$\widehat{K}_{ik}(s) = \frac{P_{ik}(s)}{Q_{ik}(s)} = \frac{p_m s^m + p_{m-1}s^{m-1} + \ldots + p_0}{s^n + q_{n-1}s^{n-1} + \ldots + q_0} \qquad 4\text{-}17$$

Where s is the Laplace variable and p, q, m and n are the coefficients and the order of the nominator and denominator respectively. The coefficients of 4-17 can directly be inserted in the state space model when it is expressed in the controllable canonical form:

$$\dot{\mathbf{x}}(t) = \begin{bmatrix} -q_{n-1} & -q_n & \cdots & -q_0 \\ 1 & 0 & 0 & 0 \\ 0 & \ddots & 0 & 0 \\ 0 & 0 & 1 & 0 \end{bmatrix} \mathbf{x}(\mathrm{t}) + \begin{bmatrix} 1 \\ 0 \\ \vdots \\ 0 \end{bmatrix} \dot{\boldsymbol{X}}(t) \qquad 4\text{-}18$$

$$\widehat{\boldsymbol{\eta}}(t) = [p_m \quad p_{m-1} \quad \cdots \quad p_0]\, \mathbf{x}(t)$$

Subsequently, the identification, essentially, comes down to estimate the coefficients and order of equation 4-17. As mentioned in Taghipour et al. (2008), this parameter fitting can be done with impulse response curve fitting, realization theory, and regression in the frequency domain. The latter is applied in the method of Perez & Fossen (2009), presumably, because it is based on the non-linear least square function available in Matlab, named invfreqs, as stated by Taghipour et al. (2008). Therein, the 'true' impulse response functions $K_{ik}(j\omega_l)$ are constructed from equation 4-16 and the objective is to find the coefficients of impulse response function $\boldsymbol{\theta}$:

$$\boldsymbol{\theta} = [p_r, \ldots, p_0, q_{n-1}, \ldots, q_0]^T \qquad 4\text{-}19$$

$$\boldsymbol{\theta}^\star = \arg \min_{\boldsymbol{\theta}} \sum_i w_i \left| K_{ik}(j\omega_l) - \frac{P(\mathrm{j}\omega_i, \boldsymbol{\theta})}{Q(\mathrm{j}\omega_i, \boldsymbol{\theta})} \right|^2 \qquad 4\text{-}20$$

Where $\boldsymbol{\theta}^\star$ is the optimal solution, i.e. the minimum fit of the lowest order, and the weighting coefficients w_i are chosen to be $Q(\mathrm{j}\omega_i, \boldsymbol{\theta})$ to linearize the least square estimation (Taghipour et al., 2008):

$$\boldsymbol{\theta}^\star = \arg \min_{\boldsymbol{\theta}} \sum_l s_{i,k} |Q_{ik}(j\omega_l, \boldsymbol{\theta}) K_{ik}(j\omega_l) - P_{ik}(j\omega_l, \boldsymbol{\theta})|^2$$
$$s_{i,k} = \frac{1}{\left|Q_{ik}\left(j\omega_l, \widehat{\boldsymbol{\theta}}_{k-1}\right)\right|^2} \qquad 4\text{-}21$$

Then this is iteratively solved where the polynomial Q of the previous iteration is chosen for the following until $Q_{ik}\left(j\omega_l, \boldsymbol{\theta}_p\right) \approx Q_{ik}\left(j\omega_l, \boldsymbol{\theta}_{p-1}\right)$ and equation 4-20 is recuperated. With the coefficients the added mass and damping coefficients can be reconstructed:

$$\hat{A}_{ik}(\omega) = \mathrm{Im}\left\{\omega^{-1}\widehat{K}_{ik}(j\omega)\right\} + A_{\infty,ik} \qquad 4\text{-}22$$
$$\hat{B}_{ik}(\omega) = \mathrm{Re}\left\{\widehat{K}_{ik}(j\omega)\right\}$$

Hence, the minimum fit is found but the order is undetermined. Therefore, the order is determined via a subsequent routine. Due to the strictly proper property that is opposed on the transfer function 4-17, the minimum order transfer function is:

$$\widehat{K}_{ik}^{min}(s) = \frac{p_1 s}{s^2 + q_1 s + q_0} \qquad 4\text{-}23$$

Thereof, the approximation of the impulse response function is determined for the minimum possible order and the coefficient of determination is computed for both the added mass and the damping coefficients:

$$R^2 = 1 - \frac{\sum_k \left(X_k - \hat{X}_k\right)^2}{\sum_k \left(X_k - \bar{X}\right)^2}, 0 \leq R^2 \leq 1 \quad \text{4-24}$$

The order is increased until the result is satisfactory, i.e. $R^2 \geq 0.99$. Thereof, the coefficients are found and an approximation of the impulse response function is found and the state space model can be realized. Appendix A contains the figures of the convolution realizations and the reconstructed added mass and damping coefficients of the barge from Ansys Aqwa as described in section 4.1. As mentioned in section 4.1, the added mass and damping coefficients are smooth with some wild points for the pure motions. For the pure motions the wild points are removed and the approximated transfer functions are reasonable, see 0. However, most of the coupling terms are fluctuating and seem to consist of only wild points which is also reflected in the fits. Nevertheless, the order of magnitude of these added mass and damping are small and the influence will be small. Only the surge-pitch and sway-yaw couplings are significant and the estimates are satisfactory.

A final issue is that the influence of the viscosity is neglected in the diffraction analysis. This assumption has the most significant effect on the roll damping. Generally, the roll damping is predicted with the Ikeda method. The method is well described by ITTC (2017b). The roll damping is composed of wave, lift, friction, eddy, and bilge keel damping. The wave damping is included in the model as it is provided by the diffraction analysis. The other components can be computed with the empirical strip method of Ikeda. The skin friction generates 5 to 10 percent and the bilge keel creates 50 to 80 percent of the total roll damping (Kawahara et al., 2011). Thereof, the roll damping is at least underpredicted by 55%. Hence, the other damping components should be added in an external damping matrix in the time domain. However, due to time pressure, the damping and possible other viscous effects are omitted in this study and it is recommended to add these if the simulations are used in future.

4.4 Wave Excitation Forces

As mentioned in section 4.2, the wave excitation forces are included directly on the kinetic side of the motion equation 4-3. However, waves need to be defined in order to have excitation forces. Therefore, a sea state is selected to include corresponding wave forces in the simulation. Generally, a sea state is characterized by a wind force, mostly described on the Beaufort scale, and a significant wave height. The surface elevation is obtained from a wave spectrum which is defined by a significant wave height and a peak wave period.

As mentioned in section 2, the wave forces are computed from the non-dimensional time averaged wave coefficients in the original model. The forces therefore depend on the significant wave height and the peak period. The former is obtained from the regulations of the World Meteorological Organization (2017), see Appendix B. the ultimate objective of the study of Sui (2021) is to obtain insight in the required minimum power to maintain manoeuvre capabilities of the tanker in adverse weather conditions. These adverse conditions are defined in the research program SHOPERA from the IMO (Kanellopoulou et al., 2019; Shigunov et al., 2019). For ships with a length under 200 meters, the wind speed is 15.7 meters per second, a significant wave height of 4 meters and a peak period between 7 to 15 seconds. However, there seems to be no clear agreements on an appropriate peak period. Sui (2021) selected a wave period of 8 seconds which is a realistic period as it occurs often in the North Atlantic Scatter, see Appendix B.

Nonetheless, mostly accidents occur when the ship is waiting at anchor in an increasing storm and the anchor starts to drag and the ship master decides to late look for shelter or to go to open sea, as pointed out by Shigunov et al. (2019). Therefore, it is a reasonably to suppose that the waves are generated by the wind, but that the sea is not yet fully developed. When the wind blows over a fetch energy is transferred to the waves and the waves will grow. In the ideal situation, this growth will continue until it is limited by bottom friction and wave breaking for an infinite fetch. This condition is called a fully developed sea. For the situation of the increasing storm, the length of the fetch and hence the wave growth can be limited by an upwind shore, the duration of the storm, or both. The wave growth for these conditions are well predicted with wave growth curves. Therewith, proper peak period corresponding to the significant wave height for a certain wind velocity, fetch and duration of the storm can consistently be predicted.

The fetch limited wave growth is modelled with the method of Young and Verhagen (1996a), as described in Holthuijsen (2007). The method is applicable for all sea states and all water depths. The non-dimensional significant wave height and the non-dimensional peak period are predicted from a water depth and a fetch with the following empirical formulae:

$$\tilde{H} = \tilde{H}_{\infty}\left[\tanh\left(k_3\tilde{d}^{m_3}\right)\tanh\left(\frac{k_1\tilde{F}^{m_1}}{\tanh\left(k_3\tilde{d}^{m_3}\right)}\right)\right]^{p} \quad 4\text{-}25$$

$$\tilde{T} = \tilde{T}_{\infty}\left[\tanh\left(k_4\tilde{d}^{m_4}\right)\tanh\left(\frac{k_2\tilde{F}^{m_2}}{\tanh\left(k_4\tilde{d}^{m_4}\right)}\right)\right]^{q} \quad 4\text{-}26$$

The coefficients are provided in table 3 below, and the non-dimensional wave height, fetch, period, and water depth are:

$$\tilde{F} = \frac{gF}{U_{10}^2} \quad 4\text{-}27$$

$$\tilde{H}_{m_0} = \frac{gH_{m_0}}{U_{10}^2} \quad 4\text{-}28$$

$$\tilde{T}_{\text{peak}} = \frac{gT_{\text{peak}}}{U_{10}} \quad 4\text{-}29$$

$$\tilde{d} = \frac{gd}{U_{10}^2} \qquad 4\text{-}30$$

Where g is the gravitation constant, U_{10} is the wind speed at 10 meters height. Note that the fetch could be eliminated and the peak period can be computed directly. Thereof, no assumption needs to be made on a fetch.

Table 3: Growth curve coefficients in the method of Young and Verhagen (1996a).

$\tilde{H}_\infty$	0.24	$\tilde{T}_\infty$	7.69
k_1	$4.14 * 10^4$	k_2	$2.7 * 10^{-7}$
m_1	0.79	m_2	1.45
k_3	0.572	k_4	0.187
m_3	0.343	m_4	0.10
p	1.14	q	2.01

Multiple wave spectra exists based on the wind generated waves, like a Pierson-Moskowitz or a JONSWAP spectrum. Obviously, the growth curve is limited to the fully developed condition $\tilde{H}_\infty$. When the wave height exceeds this limit, the waves are not wind generated. For the wind velocity of 15.7 meters per second, the maximum significant wave height is 6 meters from equation 4-28. Thereof, roughly 99% of the occurring sea states worldwide are included in the definition of adverse weather conditions, see table 4. Anyhow, the wind velocity, significant wave height and the peak period are incorporated more consistently.

Table 4: Definition of the sea state and the probability of occurrence for the sea state (Fossen, 2011).

			Percentage probability		
Sea state code	Description of sea	Wave height observed (m)	World wide	North Atlantic	Northern North Atlantic
0	Calm (glassy)	0			
1	Calm (rippled)	0–0.1	11.2486	8.3103	6.0616
2	Smooth (wavelets)	0.1–0.5			
3	Slight	0.5–1.25	31.6851	28.1996	21.5683
4	Moderate	1.25–2.5	40.1944	42.0273	40.9915
5	Rough	2.5–4.0	12.8005	15.4435	21.2383
6	Very rough	4.0–6.0	3.0253	4.2938	7.0101
7	High	6.0–9.0	0.9263	1.4968	2.6931
8	Very high	9.0–14.0	0.1190	0.2263	0.4346
9	Phenomenal	Over 14.0	0.0009	0.0016	0.0035

In case the wind is blowing from open sea, the wave growth is limited by the duration of the storm. Nevertheless, the energy from the wind is transferred similar to the waves as for the fetch-limited case. Consequently, this can be described with the same power laws. Based on this premises, Dulov et al. (2020) derived an equation which relates the duration-limited to the fetch-limited case:

$$\chi_f = \left[\frac{R(1-q_x)}{4\pi\xi_{0x}}\tau\right]^{\frac{1}{1-q_x}} \qquad 4\text{-}31$$

In which, χ_f is the fetch, $\tau = \frac{tg}{U_{10}}$ is the non-dimensional time since the beginning of the storm, and R, ξ_{0x}, and q_x are constants which are respectively 0.76, 2.41, and 0.275.
As a result, a fetch length is obtained based on the duration of a storm. This can be provided to the model of Young and Verhagen to also include the influence of the water depth on the wave growth. Hence, a consistent peak period and significant wave height are obtained to define the wave spectrum in an increasing storm.

Thereafter, the wave spectrum can be used with in a random phase amplitude model to generate random realisations of a surface elevation by a superposition of a number N harmonic waves with an random frequency ω_i, amplitude ζ_i, and a random phase angle $\tilde{\varepsilon}_i$ between 0 and 2π (Journée & Massie, 2008):

$$\zeta(t) = \sum_{i=1}^{N} \zeta_i \cdot \cos\left(\omega_i t + \tilde{\varepsilon}_i\right) \qquad 4\text{-}32$$

Where t is the time. Thereof, the Response Amplitude Operatiors (RAOs) can be used to compute the Froude-Krylov and diffraction wave loads (De Jong et al., 2020; Fossen, 2005; Journée & Massie, 2008). Thereof, the total first order force $F_{FK,D}(t$ can be obtained from the superposition principle:

$$F_{FK,D}(t) = \sum_{i=1}^{N} \left(\frac{F_{wa_i}}{\zeta_{a_i}}\right) \cdot \cos\left(\omega_i t + \varepsilon_i + \varepsilon_{w\zeta_i}\right) \qquad 4\text{-}33$$

Where N is the number of wave components in the superposition, $\left(\frac{F_{wa_i}}{\zeta_{a_i}}\right)$ is the wave load transfer function, ω_i is the wave frequency, $\varepsilon_{w\zeta_i}$ is the phase shift of the wave load with respect to the wave elevation.

The wave drift forces of an irregular sea can be expressed as the superposition of regular waves pairs (ANSYS Inc., 2016; Journée & Massie, 2008; Pinkster, 1980):

$$\begin{aligned} F_{2nd}(t) = &\sum_{i=1}^{N}\sum_{j=1}^{N} \zeta_i\zeta_j \cdot P_{ij}^{-} \cdot \cos\left[\left(\omega_i - \omega_j\right)t + \left(\epsilon_i - \epsilon_j\right)\right] \\ &+ \sum_{i=1}^{N}\sum_{j=1}^{N} \zeta_i\zeta_j \cdot Q_{ij}^{-} \cdot \sin\left[\left(\omega_i - \omega_j\right)t + \left(\epsilon_i - \epsilon_j\right)\right] \\ &+ \sum_{i=1}^{N}\sum_{j=1}^{N} \zeta_i\zeta_j \cdot P_{ij}^{+} \cdot \cos\left[\left(\omega_i + \omega_j\right)t + \left(\epsilon_i + \epsilon_j\right)\right] \\ &+ \sum_{i=1}^{N}\sum_{j=1}^{N} \zeta_i\zeta_j \cdot Q_{ij}^{+} \cdot \sin\left[\left(\omega_i + \omega_j\right)t + \left(\epsilon_i + \epsilon_j\right)\right] \end{aligned} \qquad 4\text{-}34$$

In which ζ_i and ζ_j are the wave amplitudes of the regular wave pair, P_{ij}^{-} and $P_{ij}^{+}$is the in-phase difference and sum quadratic transfer functions (QTF), Q_{ij}^{-} and Q_{ij}^{+} is the out-of-phase quadratic transfer functions, ω_i and ω_j are the wave frequencies of the wave pair, and ϵ_i and ϵ_j are the corresponding phase angles (Pinkster, 1980). The sum frequency terms are neglected as the influences are small.

As explained in section 4.1, the RAOs and QFTs are obtained from the diffraction analysis in Ansys Aqwa. The RAOs and QFTs of the finest mesh of section 4.1 are converted to lookup tables and taken into account in the model. The RAOs are shown in section 4.1. The QTFs are not represented because these depend on the wave frequency and direction of wave pairs, see section 4.4. Therefore, there are 2220000 QTFs and it is tedious to find a clear way of representing them.

In this study, only the difference QTF are included as the sum QTFs are small. Furthermore, the diffraction analysis is performed at zero velocity. Unfortunately, the diffraction analysis needs to be run for a range of velocities because the QTFs are only provided for one velocity by ANSYS AQWA. Due to time pressure, the velocity dependency is omitted in this study and it is recommended to add it in future. The forward speed can be easily taken into account by with an extension of the lookup tables with a velocity dimension. The complication, however, is that this also holds for the radiation forces, see section 4.3. Therefore, a lot of lookup tables need to be realized or, more elegant, the state space

models can be realized with the damping coefficients of Söding that include forward speed (Fossen, 2005; Tello Ruiz, 2018).

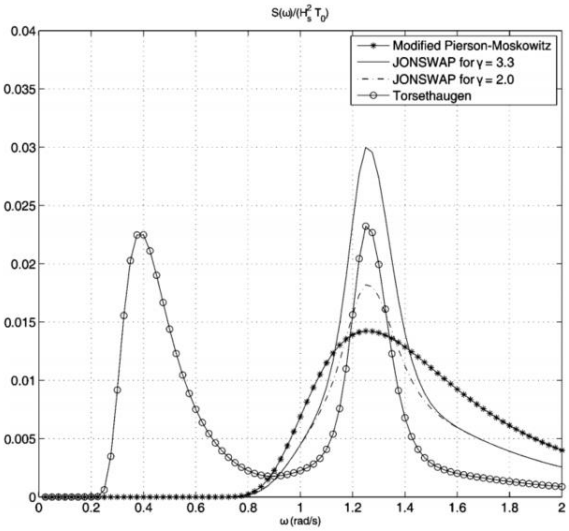

Figure 21: Comparison of wave spectra (figure 8.11, Fossen, 2011)

Accidentally, the QFTs are obtained only for unidirectional seas from Ansys Aqwa. Therefore, the study is limited to long crested waves. The waves are generated with the Wave_init.mat and Wavespec.mat functions from the MSS library (Fossen, 2011). The former contains the random phase amplitude model with which the wave realisation are created. The latter contains the functions that describe the different wave spectra and is called by the former. In the method, three wave spectra are included; the Modified Pierson-Moskowitz, the JONSWAP, and the Torsethaugen, see figure 21. The first is embedded in the ITTC recommendations, but is only applicable to fully developed seas. The JONSWAP is developed for growing undeveloped seas from measurements in the North Sea. Consequently, the peak is more steep. The Torsethaugen spectrum is developed also based on measurements in the North Sea. Likewise the JONSWAP, it describes a developing sea, but also includes the low frequency swell waves. Nonetheless, it is chosen to use the JONSWAP spectrum as the main focus is on regular waves.

In figure 22, a surface realisation of the adverse conditions as earlier defined can be seen. Based on the wind velocity of 15.7 meters per second and a fetch of 200 kilometres, a spectrum with a significant wave height of 3.85 meters with an corresponding peak period of 8.28 seconds is created. The non-dimensional wave height is 0.158 and hence the sea is not fully developed. Therefore, the method is more consistent.

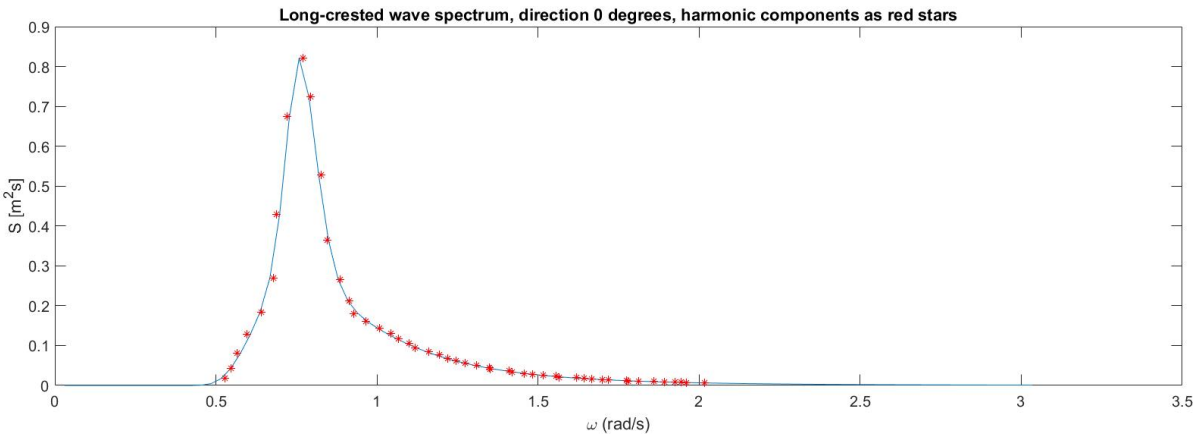

Figure 22A

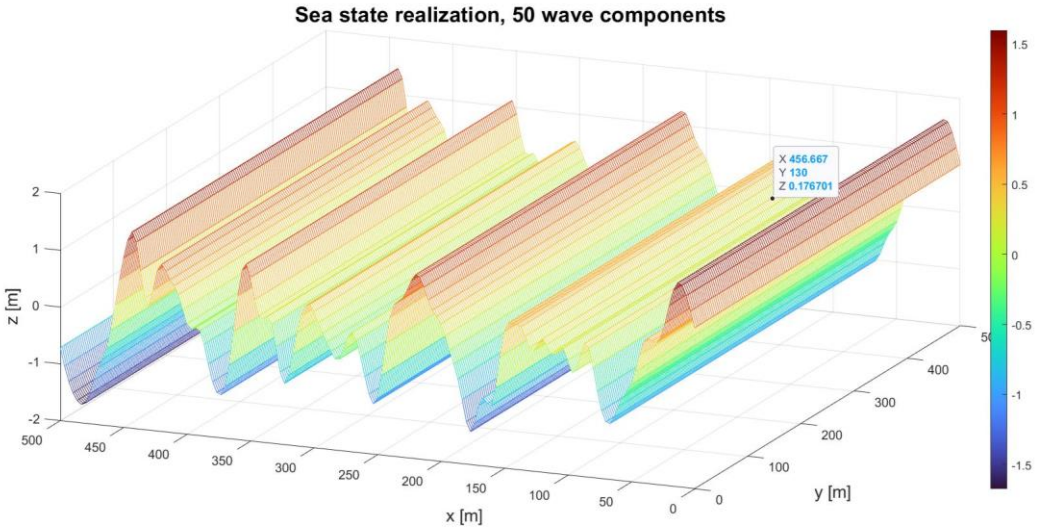

Figure 22B

Figure 22: A: The surface elevation for sea state 7 for a fetch of 200 kilo meters and a water depth of 75 meters. B: The harmonic wave components randomly generated from the JONSWAP spectrum The significant wave height is 3.85 meters with a peak period of 8.28 seconds.

4.5 Implementation of the model

With all the information of this chapter the motion equation is implemented as equations 4-35 to 4-40 below. In this equations, the convolution terms refer to the appropriate state space models as described in section 4.3, and, the hull forces refer to the Kijima model in section 2. The description of the rudder and propellor forces can be found in Sui (2021).

$$\dot{u} = \frac{1}{m_{RB11} + a_{11}}(m_{RB11}vr - m_{RB11}wq - a_{13}(\infty)\dot{w} - a_{15}(\infty)\dot{q}$$
$$- \int_0^\infty \mathrm{k}_{11}(t-\tau)u\,(\tau)d\tau - \int_0^\infty \mathrm{k}_{13}(t-\tau)\mathrm{w}(\tau)d\tau - \int_0^\infty \mathrm{k}_{15}(t-\tau)\mathrm{p}(\tau)d\tau$$
$$+ \sum_{i=1}^{N}\left(\frac{F_{wx_i}}{\zeta_{a_i}}\right)\cdot\cos(\omega_i t + \varepsilon_i + \varepsilon_{wx\zeta_i}) \qquad 4\text{-}35$$
$$+ \sum_{i=1}^{N}\sum_{j=1}^{N}\zeta_i\zeta_j \cdot \bar{P_{x}}_{ij}\cdot\sin[(\omega_i - \omega_j)t + (\epsilon_i - \epsilon_j)]$$
$$+ \sum_{i=1}^{N}\sum_{j=1}^{N}\zeta_i\zeta_j \cdot \bar{Q_{x}}_{ij}\cdot\sin[(\omega_i - \omega_j)t + (\epsilon_i - \epsilon_j)]$$
$$+X_{hull} + X_{rud} + X_{prop} + X_{wind}$$

$$\dot{v} = \frac{1}{m_{RB22} + a_{22}}(m_{RB22}wp - m_{RB22}ur - a_{24}(\infty)\dot{p} - a_{26}(\infty)\dot{r}$$
$$- \int_0^\infty \mathrm{k}_{22}(t-\tau)\mathrm{v}\,(\tau)d\tau - \int_0^\infty \mathrm{k}_{46}(t-\tau)\mathrm{p}(\tau)d\tau - \int_0^\infty \mathrm{k}_{26}(t-\tau)\mathrm{r}(\tau)d\tau$$
$$+ \sum_{i=1}^{N}\left(\frac{F_{wy_i}}{\zeta_{a_i}}\right)\cdot\cos(\omega_i t + \varepsilon_i + \varepsilon_{wx\zeta_i}) \qquad 4\text{-}36$$
$$+ \sum_{i=1}^{N}\sum_{j=1}^{N}\zeta_i\zeta_j \cdot \bar{P_{y}}_{ij}\cdot\sin[(\omega_i - \omega_j)t + (\epsilon_i - \epsilon_j)]$$
$$+ \sum_{i=1}^{N}\sum_{j=1}^{N}\zeta_i\zeta_j \cdot \bar{Q_{y}}_{ij}\cdot\sin[(\omega_i - \omega_j)t + (\epsilon_i - \epsilon_j)]$$
$$+Y_{hull} + Y_{rud} + Y_{wind}$$

$$\dot{w} = \frac{1}{m_{RB33} + a_{33}}(m_{RB33}uq - m_{RB33}vp - a_{31}(\infty)\dot{u} - a_{35}(\infty)\dot{q}$$
$$- \int_0^\infty \mathrm{k}_{13}(t-\tau)\mathrm{u}(\tau)d\tau - \int_0^\infty \mathrm{k}_{33}(t-\tau)\mathrm{w}(\tau)d\tau - \int_0^\infty \mathrm{k}_{35}(t-\tau)\mathrm{q}(\tau)d\tau$$
$$+ \sum_{i=1}^{N}\left(\frac{F_{wz_i}}{\zeta_{a_i}}\right)\cdot\cos(\omega_i t + \varepsilon_i + \varepsilon_{wx\zeta_i}) \qquad 4\text{-}37$$
$$+ \sum_{i=1}^{N}\sum_{j=1}^{N}\zeta_i\zeta_j \cdot \bar{P_{z}}_{ij}\cdot\sin[(\omega_i - \omega_j)t + (\epsilon_i - \epsilon_j)]$$
$$+ \sum_{i=1}^{N}\sum_{j=1}^{N}\zeta_i\zeta_j \cdot \bar{Q_{z}}_{ij}\cdot\sin[(\omega_i - \omega_j)t + (\epsilon_i - \epsilon_j)]$$

$$\dot{p} = \frac{1}{I_{44} + a_{44}}(-a_{42}(\infty)\dot{v} - a_{46}(\infty)\dot{r}$$
$$-\int_0^\infty \mathrm{k}_{42}(t-\tau)\mathrm{v}(\tau)d\tau - \int_0^\infty \mathrm{k}_{44}(t-\tau)\mathrm{p}(\tau)d\tau - \int_0^\infty \mathrm{k}_{46}(t-\tau)\mathrm{r}(\tau)d\tau$$
$$+\sum_{i=1}^{N}\left(\frac{F_{wk_i}}{\zeta_{a_i}}\right)\cdot\cos\left(\omega_i t + \varepsilon_i + \varepsilon_{wx\zeta_i}\right) \qquad 4\text{-}38$$
$$+\sum_{i=1}^{N}\sum_{j=1}^{N}\zeta_i\zeta_j\cdot\bar{P_{k_{ij}}}\cdot\sin\left[\left(\omega_i-\omega_j\right)t + \left(\epsilon_i-\epsilon_j\right)\right]$$
$$+\sum_{i=1}^{N}\sum_{j=1}^{N}\zeta_i\zeta_j\cdot\bar{Q_{k_{ij}}}\cdot\sin\left[\left(\omega_i-\omega_j\right)t + \left(\epsilon_i-\epsilon_j\right)\right]$$
$$\dot{q} = \frac{1}{I_{55} + a_{55}}(-a_{51}(\infty)\dot{u} - a_{53}(\infty)\dot{w}$$
$$-\int_0^\infty \mathrm{k}_{51}(t-\tau)\mathrm{u}\,(\tau)d\tau - \int_0^\infty \mathrm{k}_{53}(t-\tau)\mathrm{w}(\tau)d\tau - \int_0^\infty \mathrm{k}_{55}(t-\tau)\mathrm{q}(\tau)d\tau$$
$$+\sum_{i=1}^{N}\left(\frac{F_{wm_i}}{\zeta_{a_i}}\right)\cdot\cos\left(\omega_i t + \varepsilon_i + \varepsilon_{wx\zeta_i}\right) \qquad 4\text{-}39$$
$$+\sum_{i=1}^{N}\sum_{j=1}^{N}\zeta_i\zeta_j\cdot\bar{P_{m_{ij}}}\cdot\sin\left[\left(\omega_i-\omega_j\right)t + \left(\epsilon_i-\epsilon_j\right)\right]$$
$$+\sum_{i=1}^{N}\sum_{j=1}^{N}\zeta_i\zeta_j\cdot\bar{Q_{m_{ij}}}\cdot\sin\left[\left(\omega_i-\omega_j\right)t + \left(\epsilon_i-\epsilon_j\right)\right]$$
$$\dot{r} = \frac{1}{I_{66} + a_{66}}(-a_{62}(\infty)\dot{v} - a_{64}(\infty)\dot{p}$$
$$-\int_0^\infty \mathrm{k}_{62}(t-\tau)\dot{v}\,(\tau)d\tau - \int_0^\infty \mathrm{k}_{44}(t-\tau)\dot{p}(\tau)d\tau - \int_0^\infty \mathrm{k}_{64}(t-\tau)\dot{r}(\tau)d\tau$$
$$+\sum_{i=1}^{N}\left(\frac{F_{wn_i}}{\zeta_{a_i}}\right)\cdot\cos\left(\omega_i t + \varepsilon_i + \varepsilon_{wx\zeta_i}\right) \qquad 4\text{-}40$$
$$+\sum_{i=1}^{N}\sum_{j=1}^{N}\zeta_i\zeta_j\cdot\bar{P_{n_{ij}}}\cdot\sin\left[\left(\omega_i-\omega_j\right)t + \left(\epsilon_i-\epsilon_j\right)\right]$$
$$+\sum_{i=1}^{N}\sum_{j=1}^{N}\zeta_i\zeta_j\cdot\bar{Q_{n_{ij}}}\cdot\sin\left[\left(\omega_i-\omega_j\right)t + \left(\epsilon_i-\epsilon_j\right)\right]$$
$$+N_{hull} + N_{rud} + N_{wind}$$

5 Validation of the Model

Since the introduction of the EEDI, concerns have been raised to the survivability of ships with small engine power to maintain manoeuvre capabilities in adverse weather conditions. Therefore, this study is conducted in order to improve the fidelity of hydrodynamics in the original manoeuvring model of the Castillo de Tebra created by Sui (2021). Presently, the manoeuvring forces are modelled with the Kijima model and it is extended with the steady wave forces of a VVLC tanker. In chapter 3, it was concluded that a unified model includes the physics more consistently as all degrees of freedom are included and the seakeeping and manoeuvring theory are solved in a generic set of motion equations . Hence, it is chosen to establish a unified approach to include the wave forces in the manoeuvring model. The unified approach is based on the Cummins equations and the convolution integrals are represented by state space models. The original model is extended from a three to a six degrees of freedom and the non-linear manoeuvring forces are superimposed in the time domain. The unified model is extensively described in chapter 4. Subsequently, the aim in this chapter is to validate the new model.

In order to validate the new model, it is chosen to run a simulation of the portside turning trail in described in 5.5.1 by Sui (2021). The propellor revolutions and pitch is controlled with a single lever command which is set to 85. The rudder angle is set to -35 degrees. The environmental and load conditions are described in table 5. As described in section 4.4, the wave growth can be fetch limited, duration limited, or both. In the East China sea, a 950 kilo meter fetch can be assumed, see figure 23. This, however, is an enormous distance over which a constant wind travels. Therefore, it is more likely that the wave growth is duration limited and a constant sea state of 3 hours is assumed. In order to guarantee smooth wave signals the maximum limit of the variable time step is set to 0.1 second. Subsequently, the new model can be validated to the measurements of the full scale trail and compared to the results as provided by the original model.

Table 5: Sea trail conditions (table 5.4, Sui, 2021)

Geographic position	East China Sea	Wind scale	3-4 Bft.	Draft TF	8.50 m
Weather	Cloudy	Wind Direction	NE	Draft TM	8.55 m
Depth of Water	75 m	Sea state	Douglas 2-3	Draft TA	8.60 m

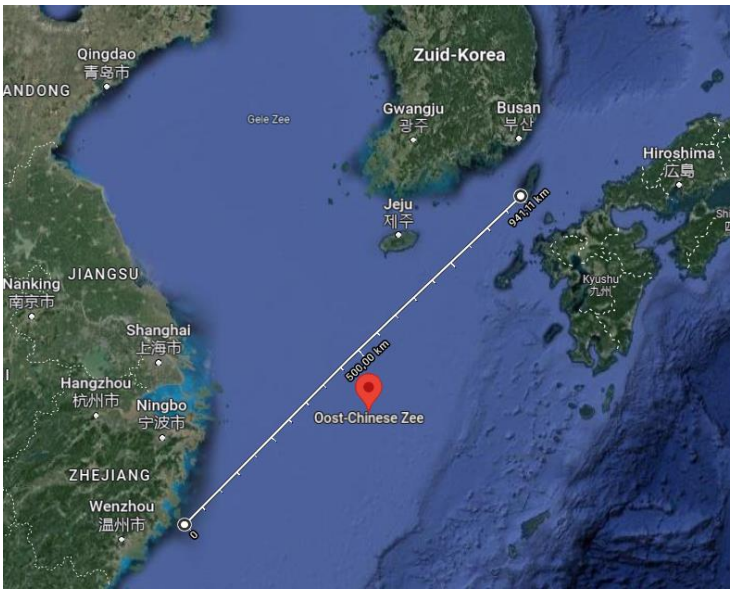

Figure 23: largest likely fetch for a North Eastern wind in the East China Sea (Google Maps, n.d.).

5.1 Results of the Original Model

The results of the original model are provided in figure 24 and figure 25. There seem to be overshoot in the advance course before turning, but overall the results is acceptable. A difference is that the model predicts a smooth line whereas the measurement fluctuates considerably. The reason is that the time averaged steady wave forces coefficients are multiplied with the significant wave height and a peak period. Thereof, the result is valid for an effective regular wave. Moreover, the measurements might subjected to errors due to the relative accelerations onboard. No additional information on the measurements is provided and questions can be raised on the reliability. Yet few measurements exists of full sea trails and therefore the data are used. In the turning cycle, the surge wave forces mostly opposes the motion even in quartering and following seas, see figure 25. This, however, is supported by the results of provided in figure 3 in chapter 2. For low speeds a sign change appears whereas for higher velocity the time averaged steady wave forces act as additional resistance. The forces also increase with the velocity. Moreover, the steady hull forces can be found in figure 26. It can be seen that the drift angle is introduced by the rudder and that the ship starts to drift until the force equilibrium is found and thereof the ship is turning steadily. It, however, is remarkable that the surge hull force becomes zero while the ship resistance is included in this component.

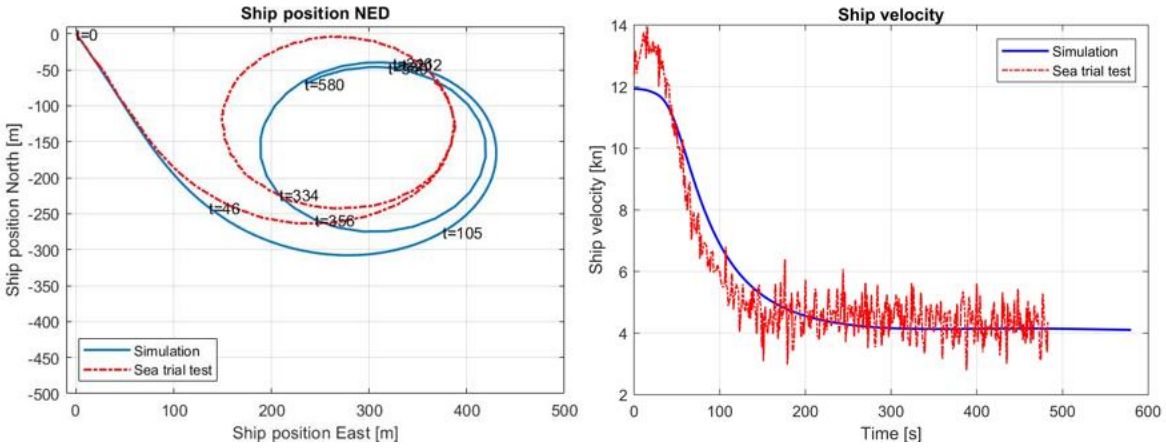

Figure 24: Validation turning circle results of the original model.

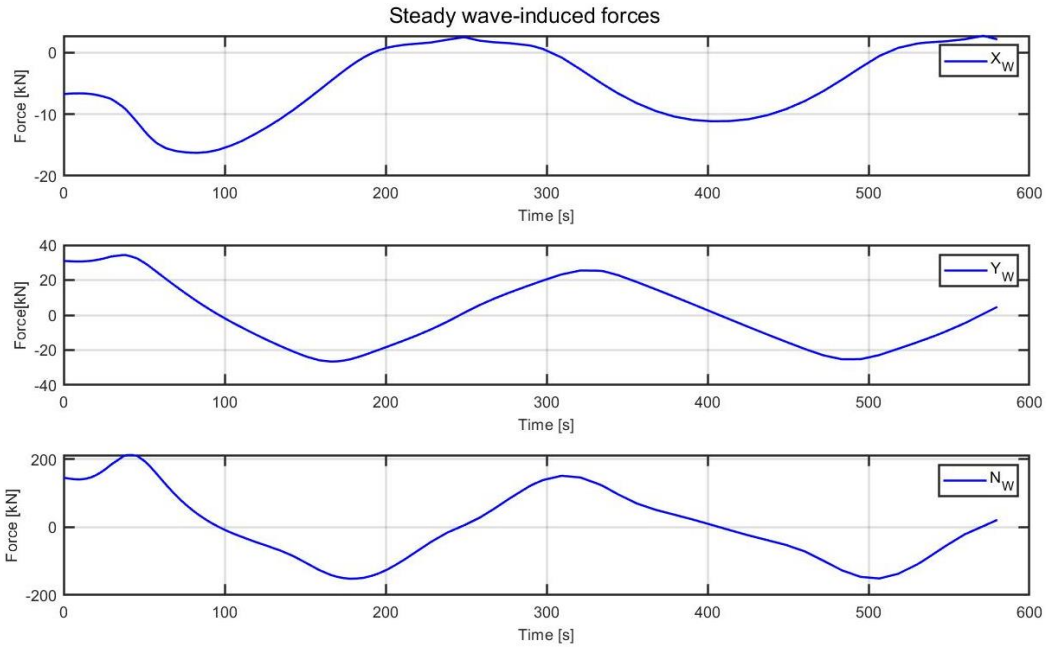

Figure 25: Time series of the time averaged steady wave-induced forces in the turning trail of figure 24.

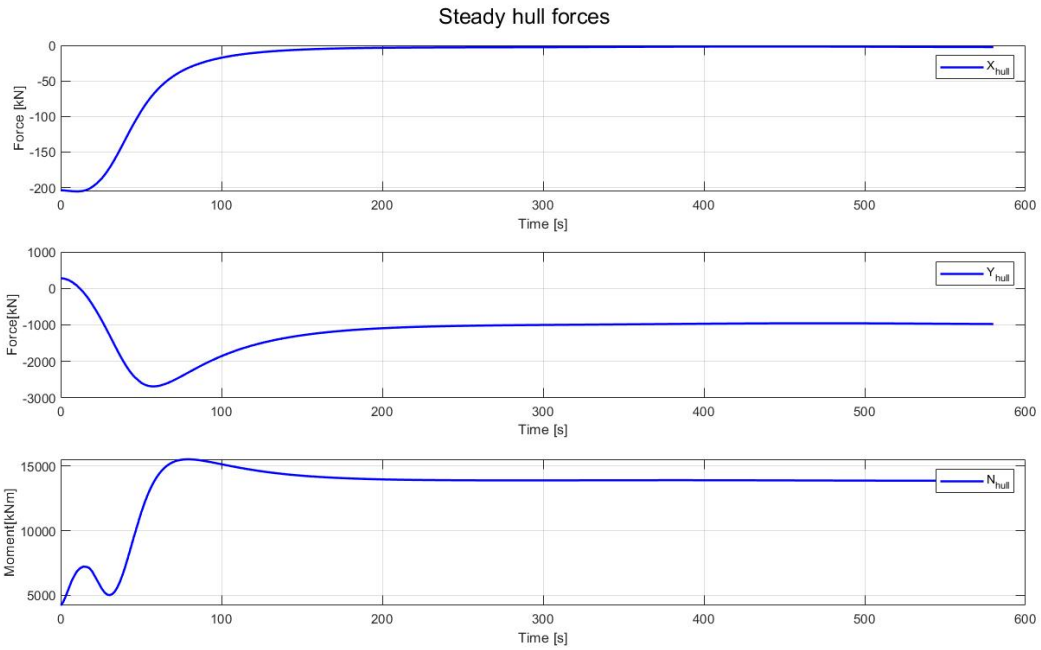

Figure 26: Time series of the steady hull forces in the turning trail of figure 24.

5.2 Results of the New Model

The results of the new model are shown in figure 27 to figure 33 below. First and foremost, the result is slightly larger than the turning cycle of the original model and larger in the simulation than in reality. The velocity drops slower and remains higher than the real sea trail test and the original model. Hence, the original model is slightly more accurate than the new model. Likewise, the result is considered to be acceptable. Recall that the wind and waves are coming in from Northeast and the simulation therefore starts with roughly beam sea. To ease the comparison of the forces, the sailing time is included figure 27. Hence, the ship experiences head sea at about 100s and it sails in following seas again at 190s, and so forth. In figure 28, the wave components of the long crested waves in the simulation are presented in the spectrum and a realization is given. The significant wave height and the peak period are 0.45 meters and 2.6 seconds, respectively.

In figure 29, the first order wave excitation forces are given. The forces are significantly larger than the wave-induced forces and moment of the original model, see figure 27. The sway, heave, and roll forces and moment seem to have expected behaviour. The magnitude appears in beam waves and the magnitude decreases in head waves. Contrary, the sway force and roll moment have distinct minima in beam seas. It is remarkable that the heave and pitch behaviour seem to be reversed for head and beam seas. Also, the yaw moment seem to increase in beam seas and decrease in head seas. The reason could be that the roll motion is not damped properly as the vicious damping is not implemented. Thereof, the motions can be large when roll is excited in the natural frequency. The pitch and yaw moment have significantly larger magnitude than the other components. No different behaviour appears for head or following waves because of the symmetry of the barge.

In figure 30 the second order wave forces are plotted. The forces are in the same order of magnitude as the time averaged steady forces. However, the forces are fluctuating significantly. The order of magnitude of the surge, sway and roll forces and moment are roughly 10 times smaller than the first order wave forces, whereas; the heave, pitch and yaw force and moments are a factor 1000 smaller. The behaviour of the forces is similar as described for the first order forces above.

The first and second order forces show the same general behaviour as the time averaged wave-induced forces and moment of the original model, see figure 27. The forces are, however, fluctuating significantly. For surge, the maximum forces are found in head waves and reduced towards beam waves. The sway force behaves opposite. When time average is taken a similar result might be expected for the new model. On the contrary, this is hard to conceive for the yaw moment.
The time series of the radiation added mass forces seem somewhat awkward and are difficult to interpretate, see figure 31.

The radiation added mass and damping force seem only important in the first 100 seconds of the simulation, see figure 31 and figure 32. Thereafter, the forces all tent to zero except for the roll moments. There seems to be an initiation issue in the simulation and especially the surge, sway and yaw forces and moments seem to be responsible for the course deviation in the beginning of the turning circle. The surge radiation damping force peak enhances the forward velocity impulse. The sway and yaw radiation damping force and moment opposes the steady hull force, see figure 33. These latter force and moment are the fluid reaction forces that cause the ships manoeuvre.

To conclude, the order of magnitude of the forces is similar but the magnitude of the forces is not. When the time average is taken of the forces, the same behaviour of the forces might appear. The radiation forces in the initiation stage of the turn seem responsible for the difference in the turning trajectory and velocity in figure 27. Therefore, it is concluded that the original and the new model perform similarly acceptable.

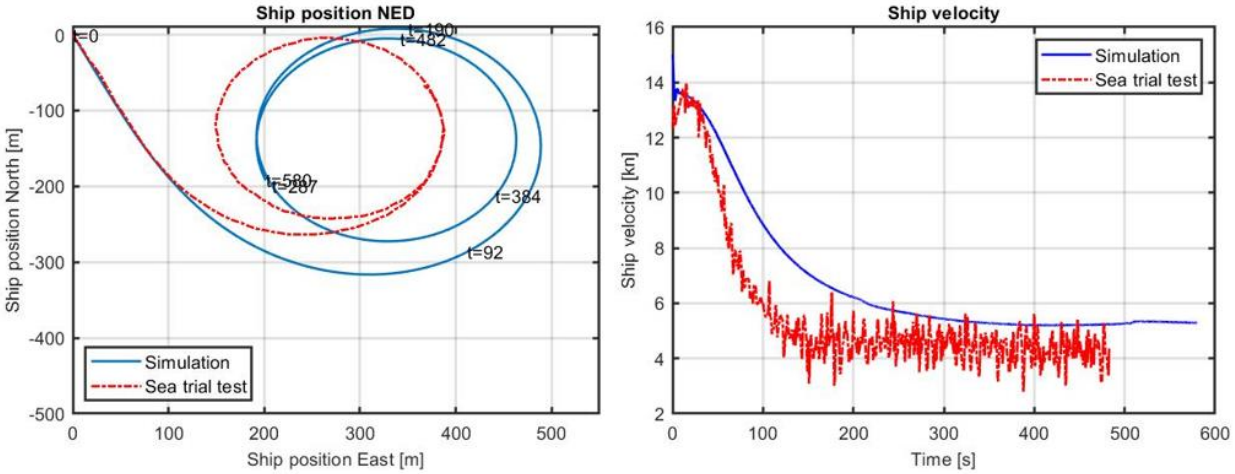

Figure 27: Validation turning circle results of the new model.

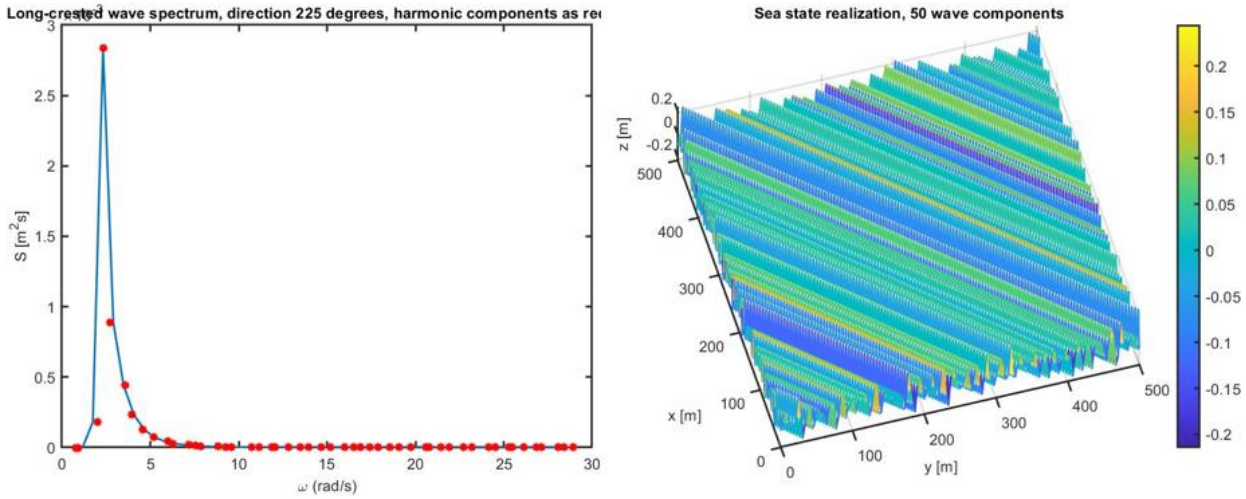

Figure 28: Wave spectrum and surface elevation in the turning cycle trail for 3 hours constant sea state 4.

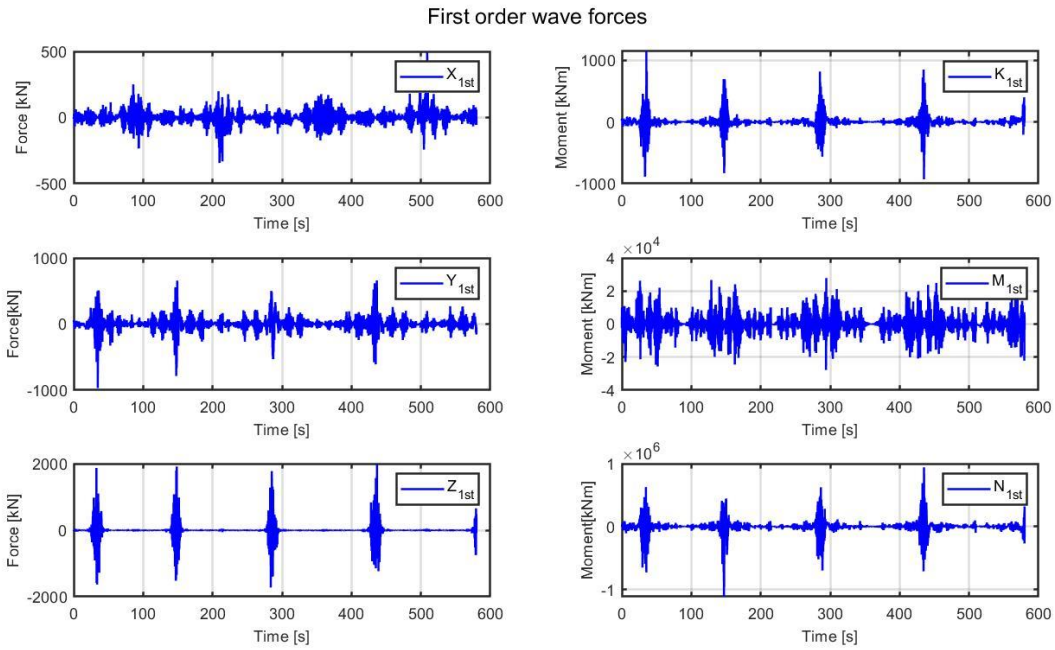

Figure 29: First order excitation forces in the turning cycle trail.

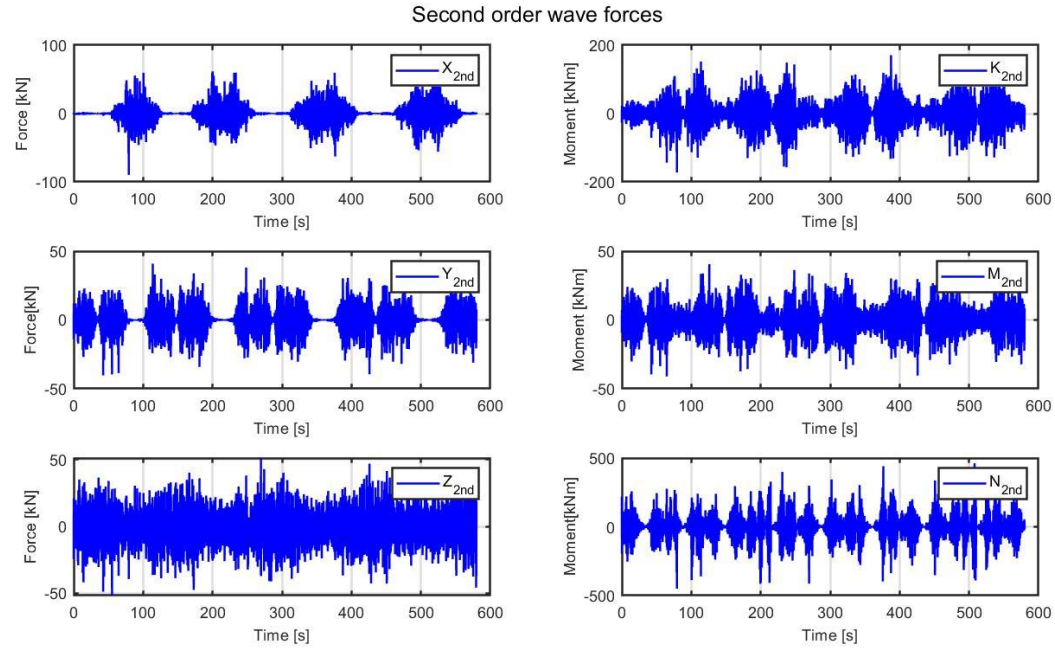

Figure 30: Second order wave excitation forces in the turning cycle trail.

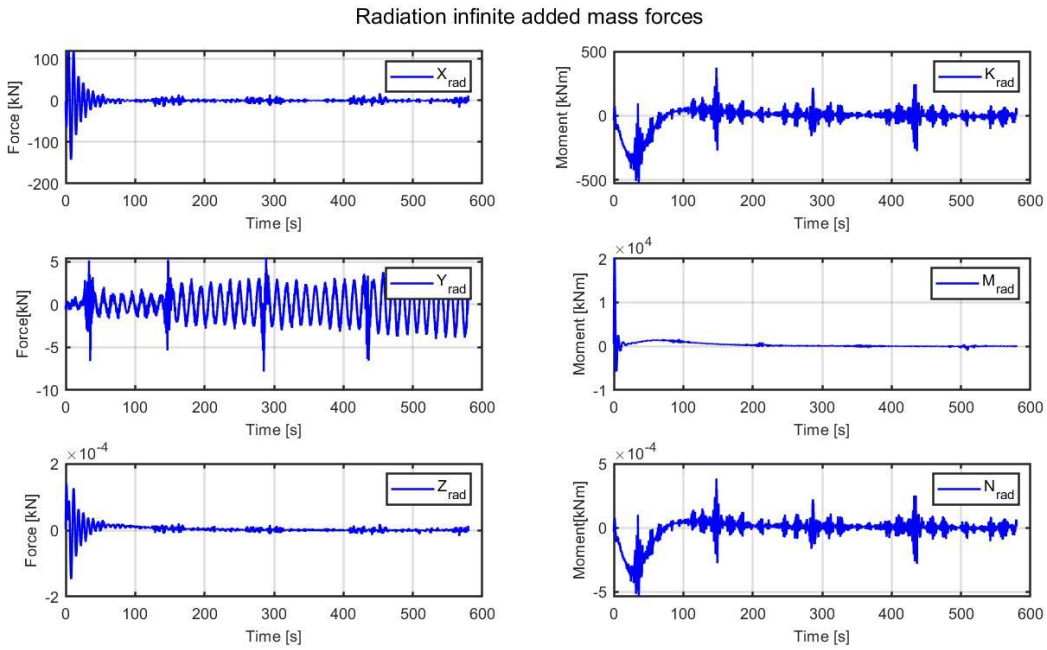

Figure 31: Results of the radiation infinite added mass forces in the turning cycle trail.

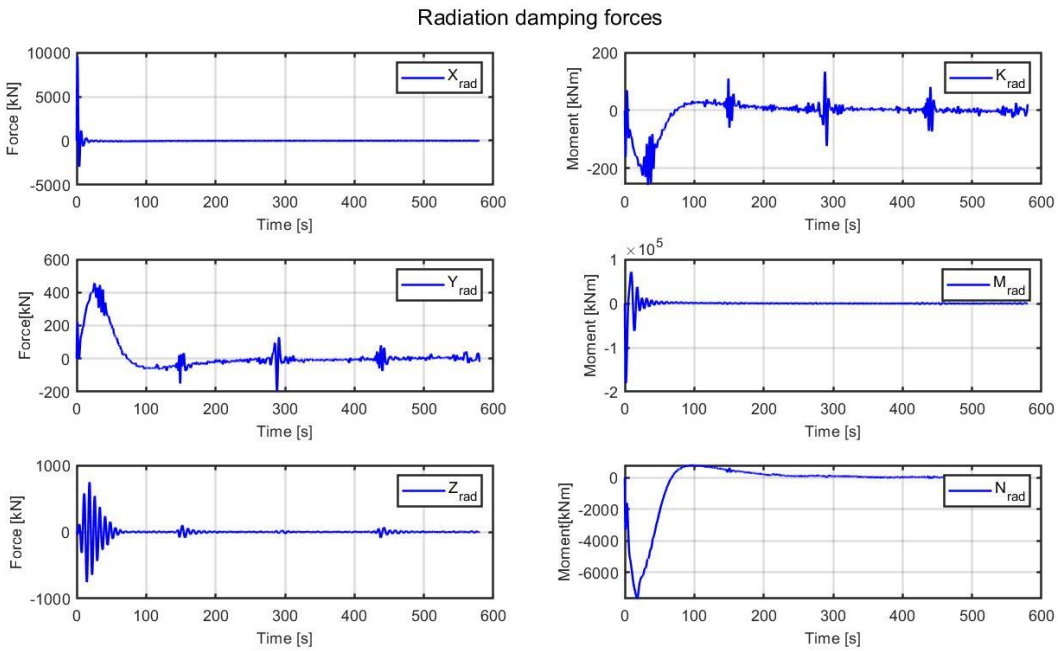

Figure 32: Results of the radiation damping forces in the turning cycle trail.

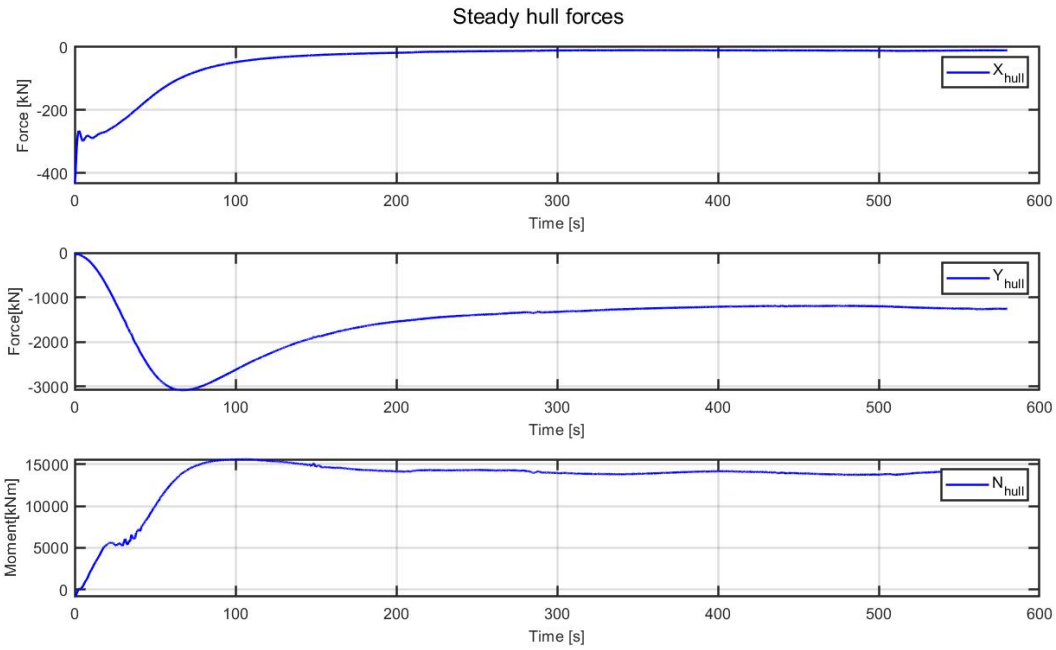

Figure 33: Hull forces in the turning cycle trail.

5.3 Engine Power Trajectory

In figure 34 and figure 35, the power trajectory of the turning trail of the original and the new model are given. As can be seen the power rise during the turning trajectory appears lower in the engine envelope for the new model. In the original model, the power rise approaches the mechanical limit of the engine closer than the new model. This can be seen in the close ups as the vertical distance between the top of the power trajectory and the green line is larger for the new model. In the original model a small decrease in engine speed appears at the beginning when the turning is initiated and during the power rise. In the new model, an initiation fluctuation appears in the bottom followed by a straight line. Yet, the fluctuations are small. Subsequently, it can be concluded that the varying wave forces have little influence on the engine performance. Therefore, the assumption, that only the time averaged wave forces have to be included, of the authors of the two time-scale approach seems to confirmed. Nevertheless, the Kijima steady hull forces could be corrected for the actual trim and heave during sailing. This, however, is not included due to time constraints on the thesis.

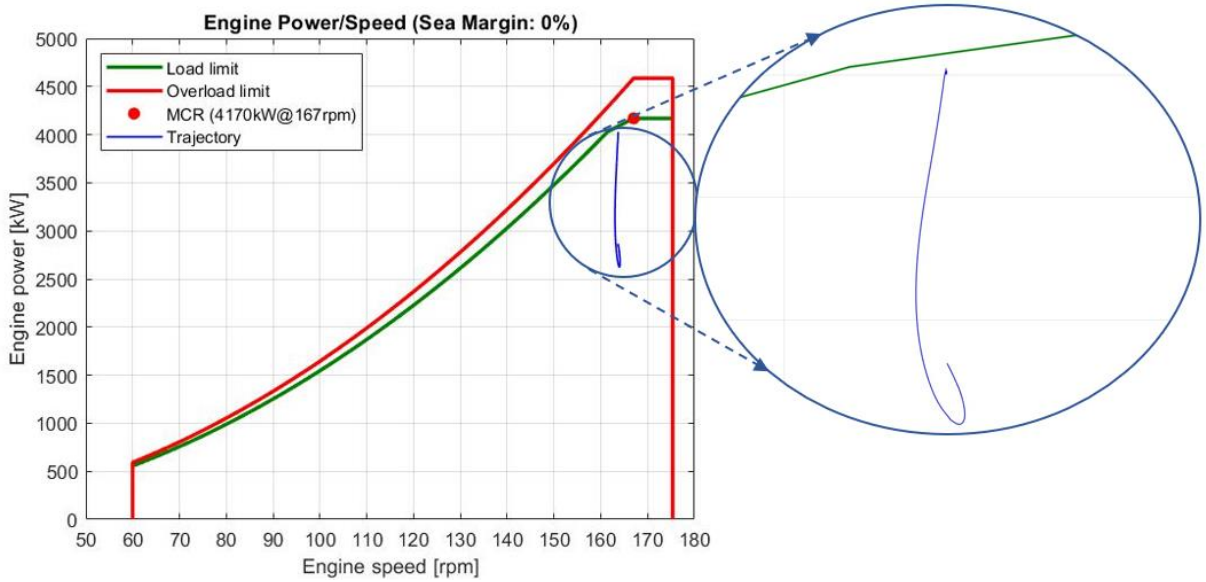

Figure 34: The power trajectory of the engine of the turning trail of figure 24 plotted in the engine envelop with thermal and mechanical limits of the original model.

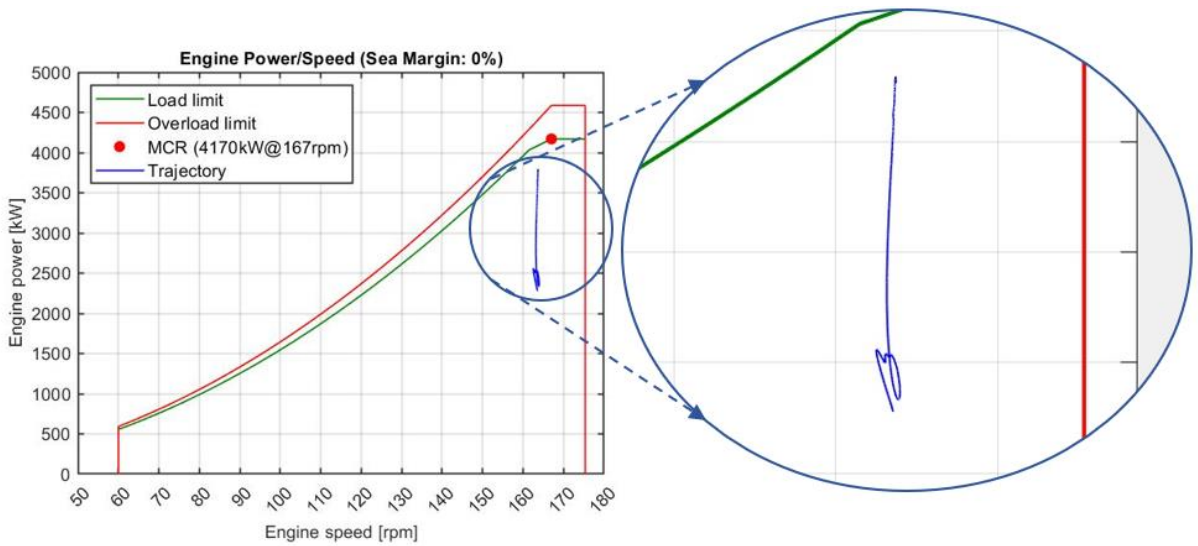

Figure 35:The power trajectory of the engine of the turning trail of figure 27 plotted in the engine envelop with thermal and mechanical limits of the new model.

6 Turning into head waves in a storm

As introduced in chapter 1, concerns have been raised regarding the operational safety of new built ships in adverse weather conditions (SHOPERA, 2016). For new built ships, the most effective solution to comply with the Energy Efficiency Design Index (EEDI) is slow steaming and hence to install smaller engine powers. These ships are expected to sail with insufficient propulsion and steering capability to maintain speed and manoeuvrability in adverse weather conditions. This hypothesis is proven by the statistical study conducted by Ventikos et al. (2018).

The new built ships will perform outstanding in the sea trails after launched and comply with the safety regulations. In general sailing conditions, the ships are safe. However, the ships are jeopardized when the ships are waiting to berth anchoring off shore. A storm approaches and the wind force increases significantly while the growing waves are mild. The ship masters rely on capabilities of the ship and the anchor to survive these conditions and no shelter is searched until the anchor starts to drag. While the ship is dragging and the master applies full engine power, the ship is not able to accelerate and overcome the environmental conditions. Consequently, groundings and collisions occur which might have been prevented with more engine power. Examples are the grounding of Pacha Bulker in Newcastle, Australia, in 2007, the collision of Bungo Princess and a bridge in Yokohama, Tokyo Bay, in 2019, and the collision of Julietta D with the Pechora Star and an offshore wind park transformer tower in Ijmuiden, Netherlands.

The Pasha Bulker accidents, has been most profoundly in the news and the storm is named after it. The accident is reported by NSW Maritime (2007). The Pasha Bulker was anchoring roughly 5 nautical miles from Nobbys Beach on the 7th of June 2007. A weather warning was provided, but the captain decided to stay relying fully on the capabilities of the anchor holding of the young ship. Yet, an additional two shackles of anchor line had been released, but no ballast water was taken in. At 7:00PM, the weather starts to deteriorate until a sea state 10 at 12:30AM on the 8th of June. At 7:10, the Pasha bulker starts to drag and the attempt to run for open sea leads to the grounding at 9:50 in sea state 9 from South-east (NSW Maritime, 2007). In figure 36, the sailed trajectory of the Pasha Bulker can be seen. The ships drags to the shore, probably with head waves as the bow is attached to the anchor. Then it starts course in beam waves with a velocity between 1 and 1.5 knots. According to NSW Maritime (2007), a heading change to head waves is commanded to negate the northerly drift. The steering control is lost and the wind blows the bow to the coast and the ships runs aground. Thereof, it is concluded that the ship had insufficient propulsion and steering capability to maintain speed and manoeuvrability in adverse weather conditions.

In order to investigate the minimum power limit with the Castillo de Tebra, a similar scenario is simulated. The ship will start in beam waves while sailing North whereafter a turn into head waves is engaged to the West in storms of sea states 7, 8 and 9

Figure 36: Sailing trajectory of the Pasha Bulker before grounding in pink (NSW Maritime, 2007).

6.1 Turn Into Head Waves of the Original Model

In this section, the results of the benchmark ship are presented in figure 37 to figure 44 obtained with the original model. The significant wave height in the original model was 4, 5.5, and 7 meters for sea state 7, 8, and 9, and the wave period was 8 seconds. The ship is able to accomplish the turn in sea state 7 and 8, but that it does not in sea state 9. The turn is executed within the first 150 seconds. The engine runs in the same operation conditions for sea state 8 and 9. From the comparison of the environmental forces and moment on the ship, it is seen that the magnitude increases with roughly a half between sea state 8 and 9. The wind forces are smaller than the wave forces, but the steady hull forces are the largest.

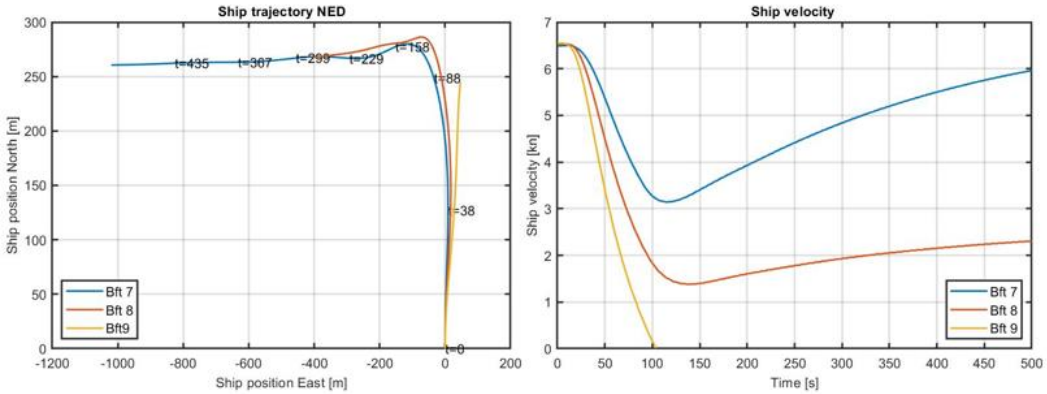

Figure 37: The sailing trajectory and velocity of the simulation of the turn into head waves trail in sea state 7, 8, and 9 Beaufort of the original model of Sui (2021).

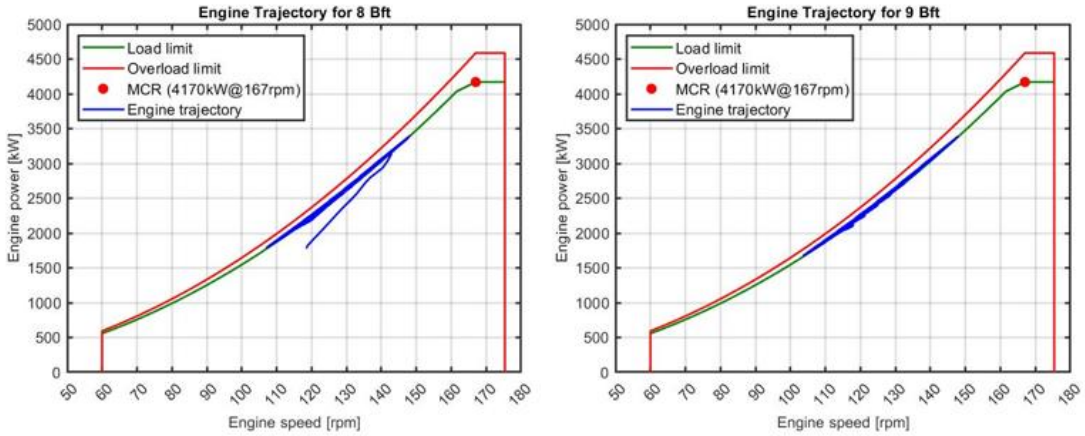

Figure 38: The engine trajectory in the simulation of the turn into head waves trail of the original model in sea state 8 on the left and sea state 9 on the right.

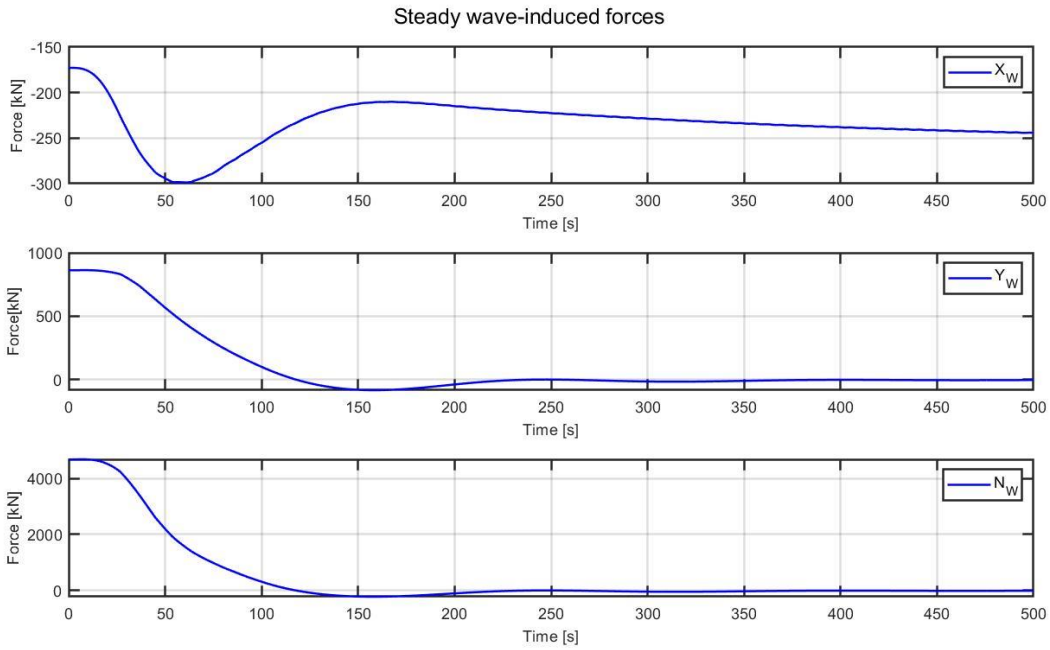

Figure 39: Time averaged stead wave-induced forces of the original model in the simulation of the turn into head waves trail in Beaufort 8.

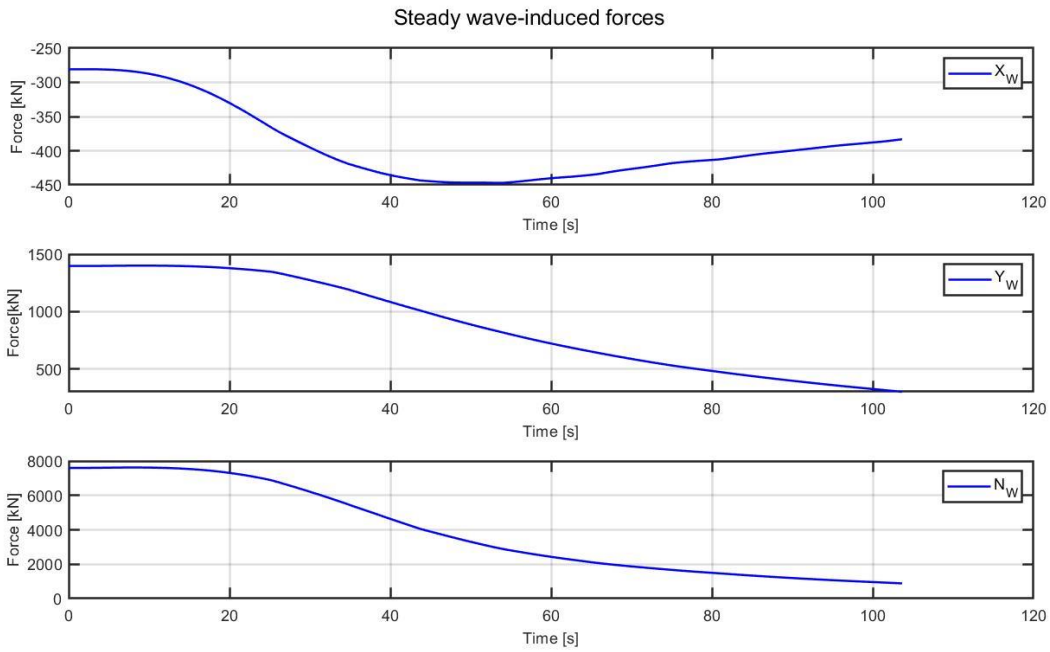

Figure 40: Time averaged stead wave-induced forces of the original model in Beaufort 9 in the simulation of the turn into head waves trail.

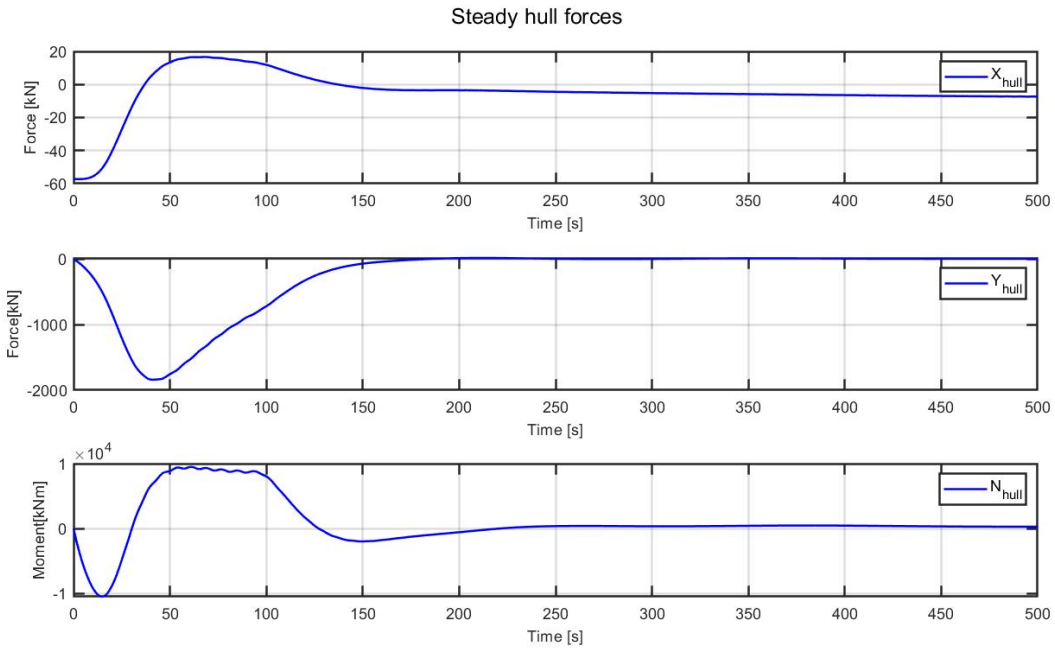

Figure 41: The steady hull forces of the original model in the simulation of the turn into head waves trail in Beaufort 8.

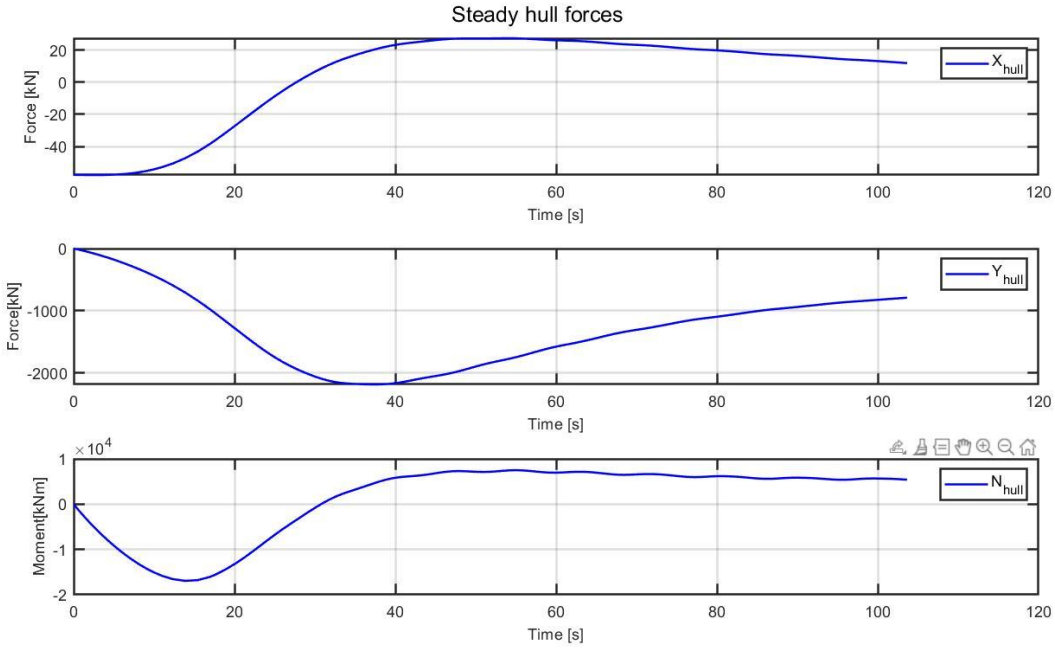

Figure 42: The steady hull forces of the original model in the simulation of the turn into head waves trail in Beaufort 9.

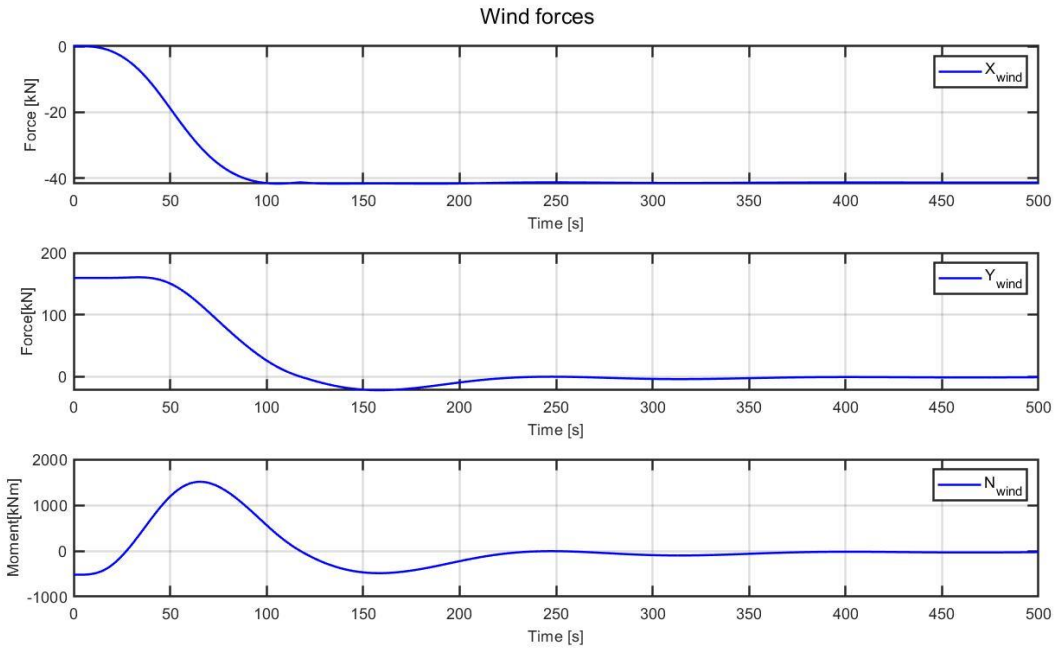

Figure 43: Wind forces of the original model in the simulation of the turn into head waves trail in Beaufort 8.

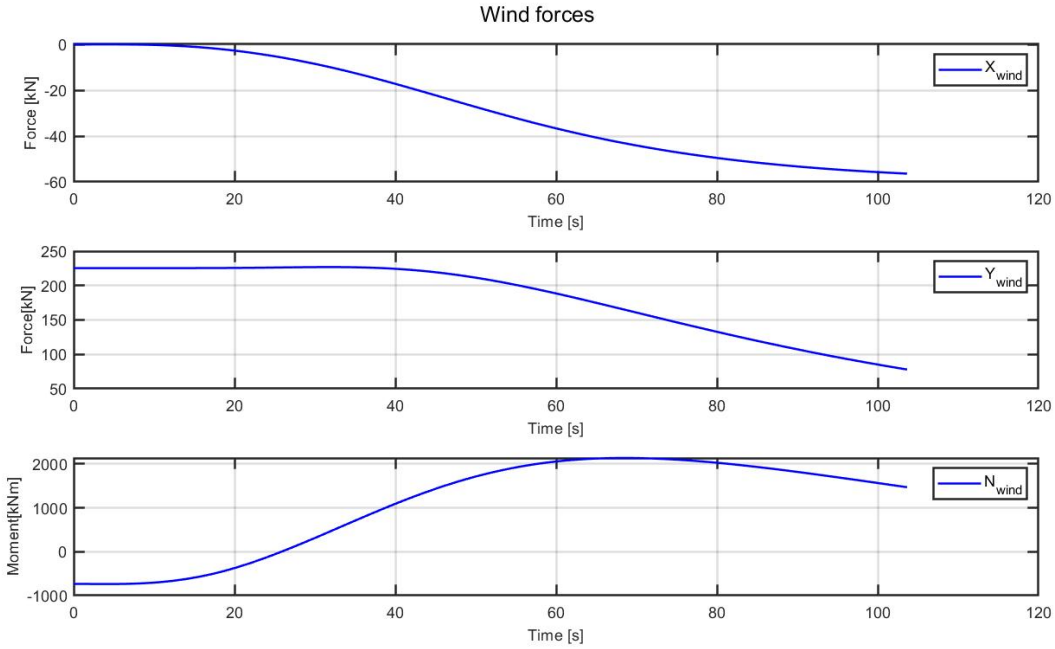

Figure 44: Wind forces of the original model in the simulation of the turn into head waves trail in Beaufort 9.

6.2 Turn Into Head Waves of the New Model

Like the original model, the turn into head waves simulations are carried out with the new model. The ship starts in beam waves and sail to the North and make a turn to the West in storms of sea states 7, 8 and 9 with a duration of 9, 12, 18 and 24 hours. Contrary to the simulations in the original model, the initial velocity is lower following the Pasha Bulker events. The corresponding wave height and peak periods for the sea states can be seen in figure 45 below.

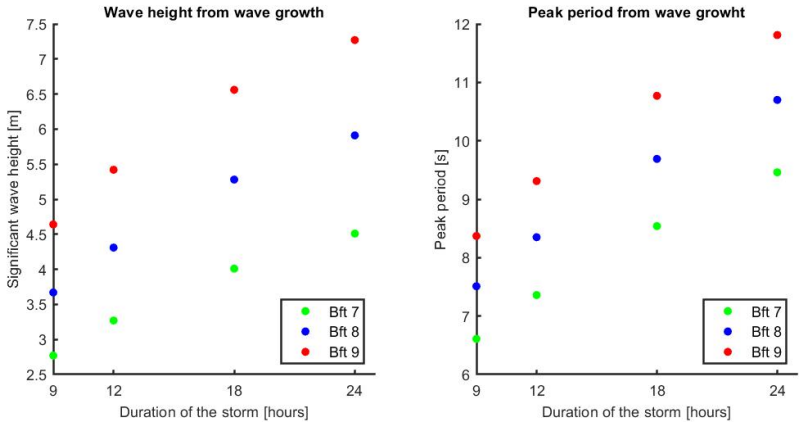

Figure 45: Sea state properties for the duration limited seas for Beaufort 7, 8, and 9.

The results of the trajectories are provided in figure 46, figure 47,and figure 48 below. As immediately can be seen is that the ship is able to turn into head waves and to speed up to the design speed in all sea states. Thereof it must be concluded that the ship is not underpowered. It is important to mention that the heading change is engaged after 20 seconds. The acceleration is inverse proportional with increasing weather conditions. It would be expected that for milder sea conditions the yaw rate would be higher. This, however, cannot be observed in the trajectories. The same behaviour is found in the power trajectories of the engine in figure 49, figure 50, and figure 51. The engine starts at a small speeds where it provides small power. Then it accelerates and more power can be supplied due to the higher efficiency of the turbo. Thereof, it is able to speed up to the design point of the engine, the maximum continuous rating (MCR). Contrary in the sea states of 7 and 8 Beaufort, the engine provides already more power at the low velocity. Nevertheless, it also accelerates to full power.

In order to understand the differences, the forces of the original and the new model are compared for 8 and 9 Beaufort. Therefore, the storm of 18 hours for sea state 8 and 24 hour storm for sea state 9 are selected as these produce the most similar significant wave heights as considered in the original model. The results are provided in figure 52 to figure 57. The most significant difference is found in the wave forces. In the new model, the wave forces and moment are between a factor 4 and 10 larger and fluctuate significantly. In the original model, high wave forces are induced in beam and bow waves, whereas in the new model these are small. As can be seen in figure 3, this is due to the high forward speed. Thereof, it seems that the added resistance in the original model is over predicted in beam waves compared to the hazard situations as the Pacha Bulker event. The velocity effect is not taken into account in the new model. The behaviour of the steady hull forces seem corresponding. The original model starts at a high velocity whereas the new model starts at a low velocity. This is seen in the longitudinal component which contains the ship resistance. The transverse and yaw components correspond to the transverse velocity and heading changes. All components are distorted by the wave induced velocity fluctuations. Lastly, the wind forces are altered by the differences in heading between the original and new model which is expected.

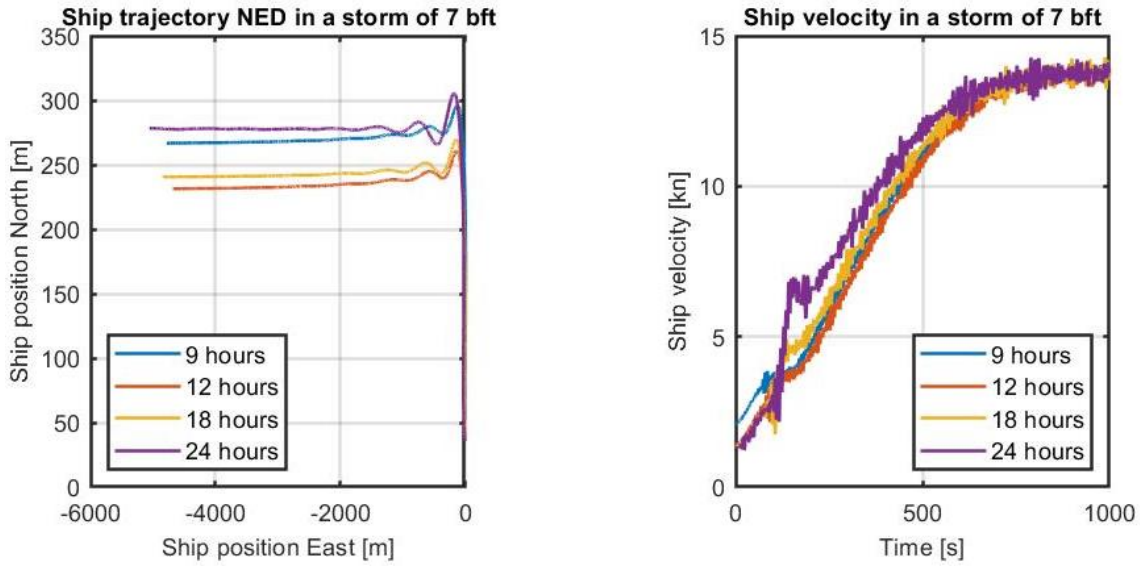

Figure 46: Ship trajectory and velocity in the head turn trail for 7 Beaufort.

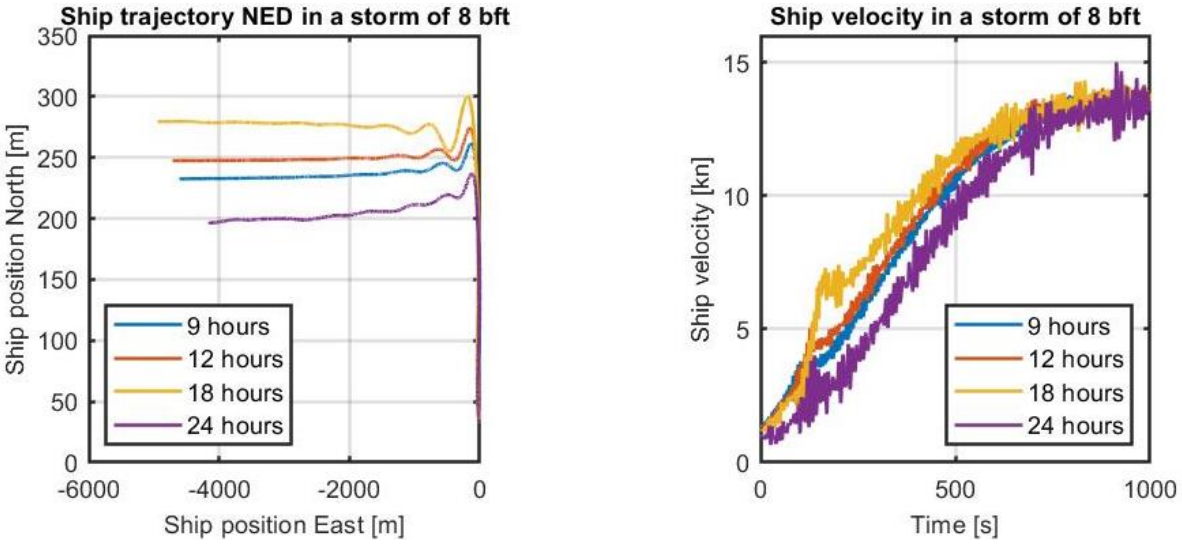

Figure 47: Ship trajectory and velocity in the head turn trail for 8 Beaufort.

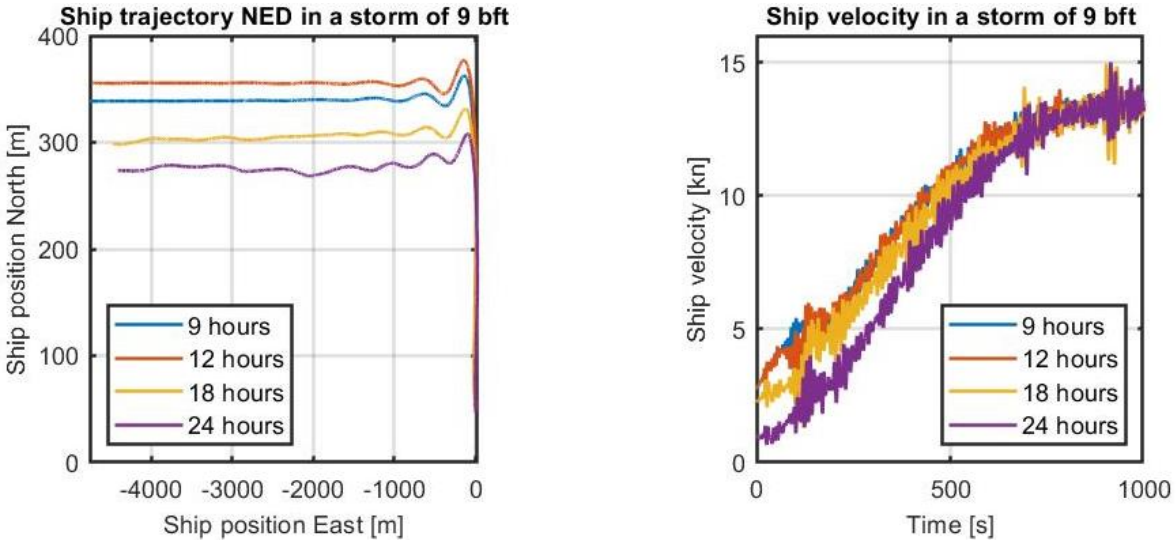

Figure 48: Ship trajectory and velocity in the head turn trail for 9 Beaufort.

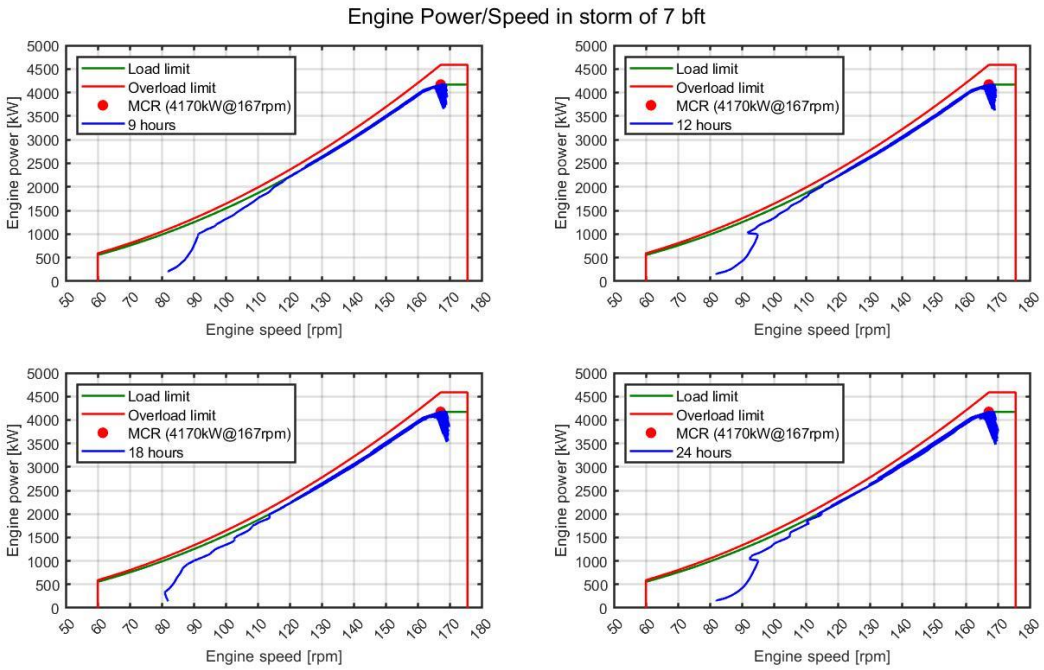

Figure 49: The power trajectory of the engine of the turn against the wind experiment corresponding to figure 46 plotted in the engine envelop with thermal and mechanical limits.

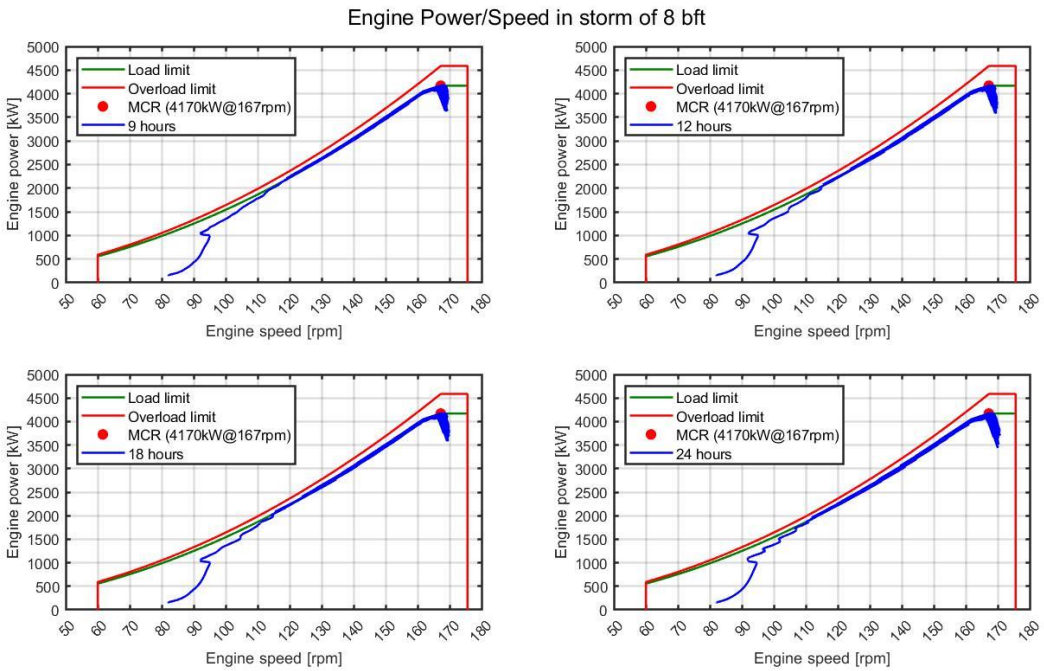

Figure 50: The power trajectory of the engine of the turn against the wind experiment corresponding to figure 47 plotted in the engine envelop with thermal and mechanical limits.

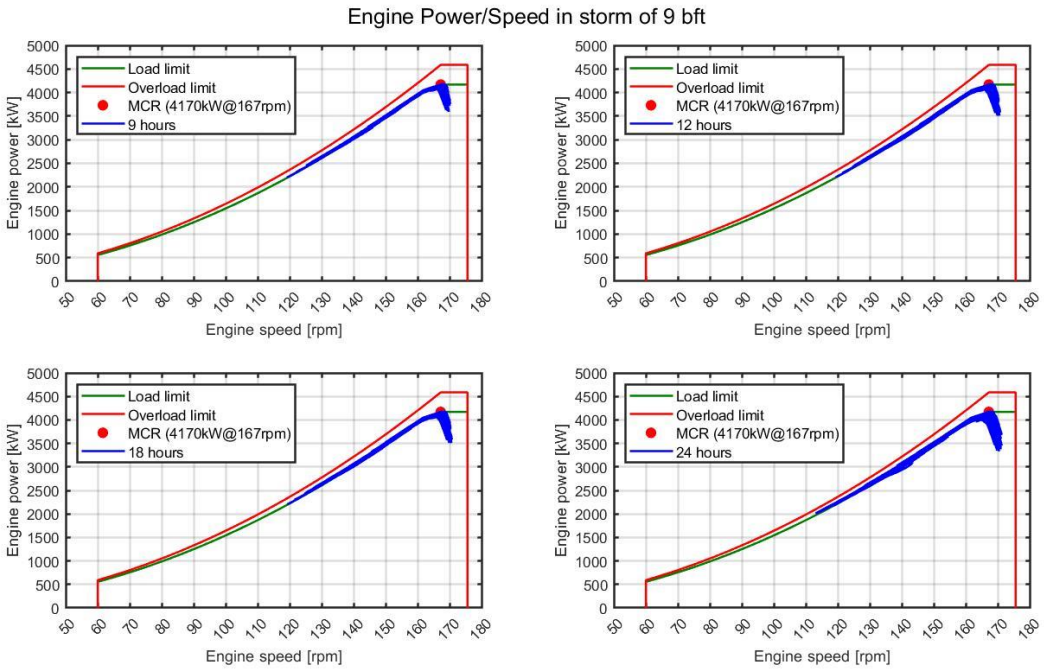

Figure 51: The power trajectory of the engine of the turn against the wind experiment corresponding to figure 48 plotted in the engine envelop with thermal and mechanical limits.

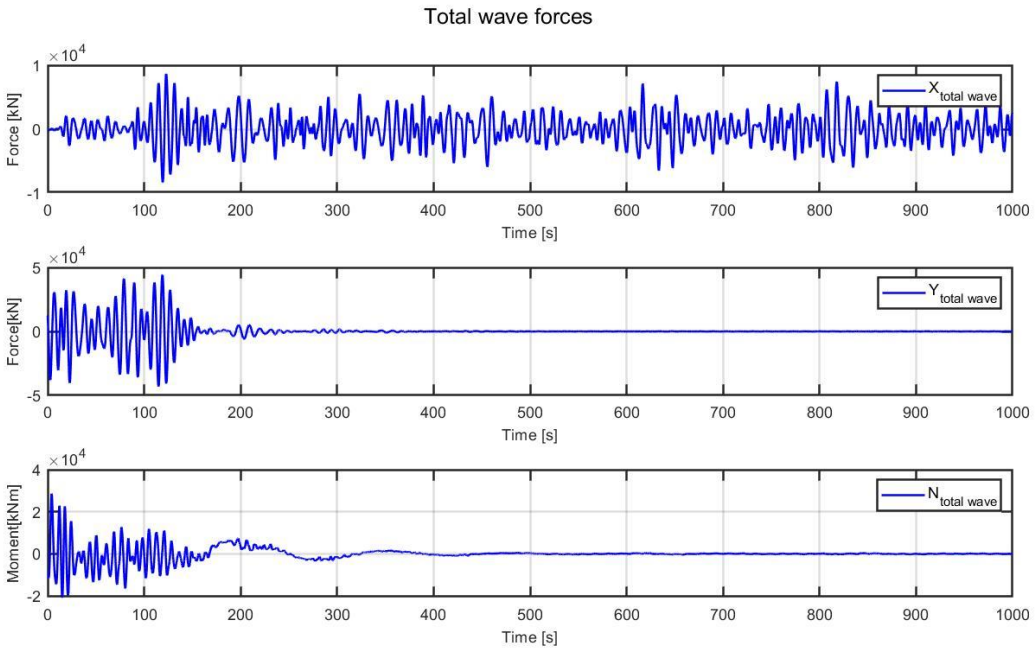

Figure 52: The total forces in the new model in Beaufort 8 in the simulation of the turn into head waves trail. The total wave force contains the 1st and 2nd order wave forces and the radiation forces.

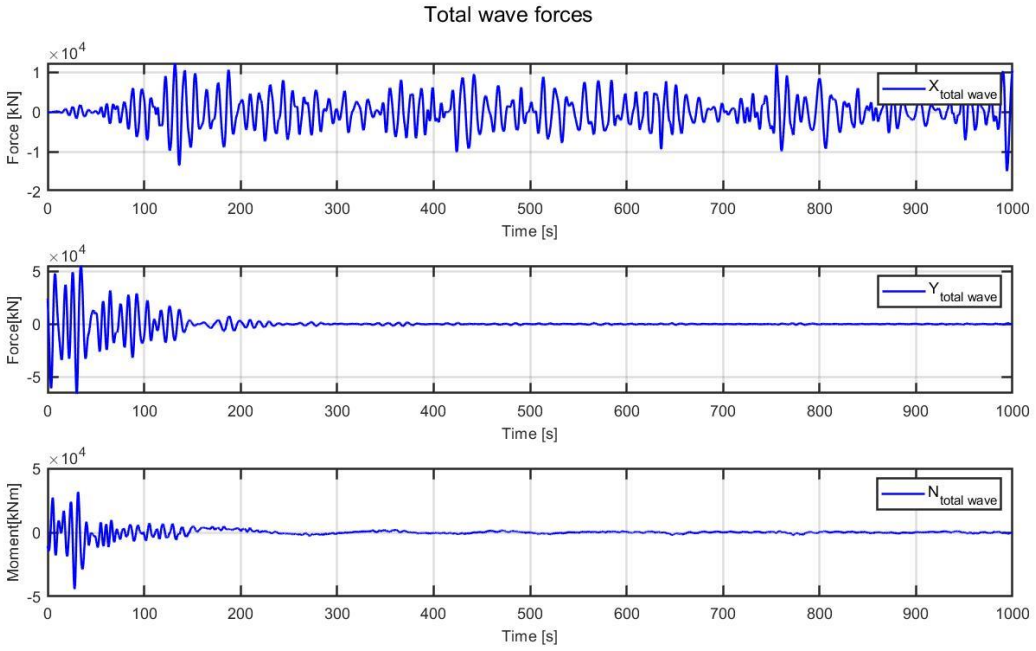

Figure 53: The total forces in the new model in Beaufort 9 in the simulation of the turn into head waves trail. The total wave force contains the 1st and 2nd order wave forces and the radiation forces.

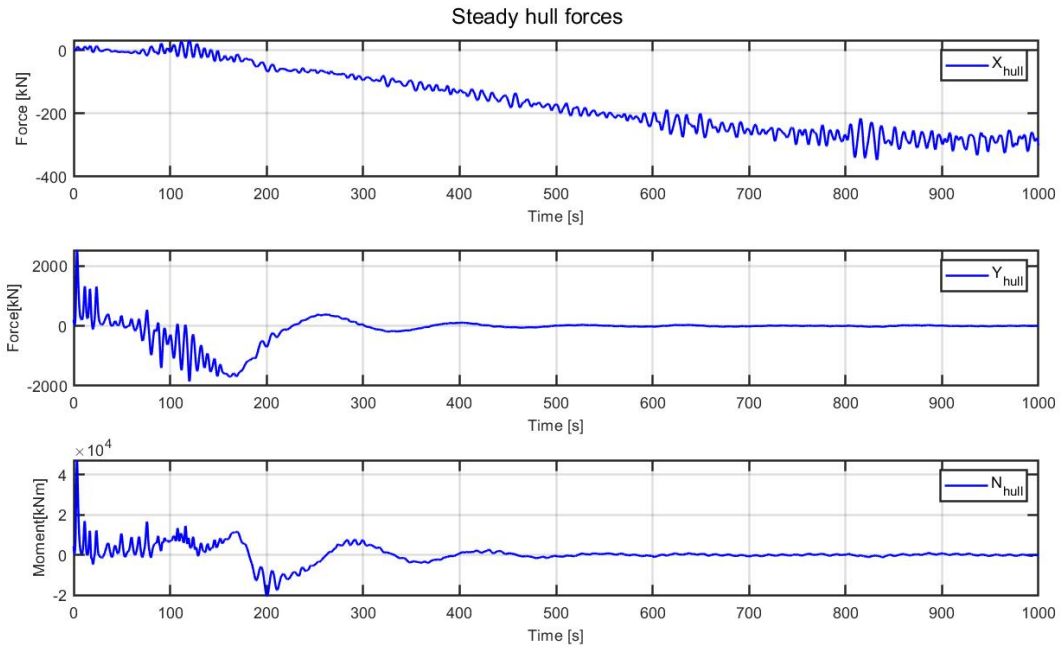

Figure 54: The steady hull forces of the new model in the simulation of the turn into head waves trail in Beaufort 8.

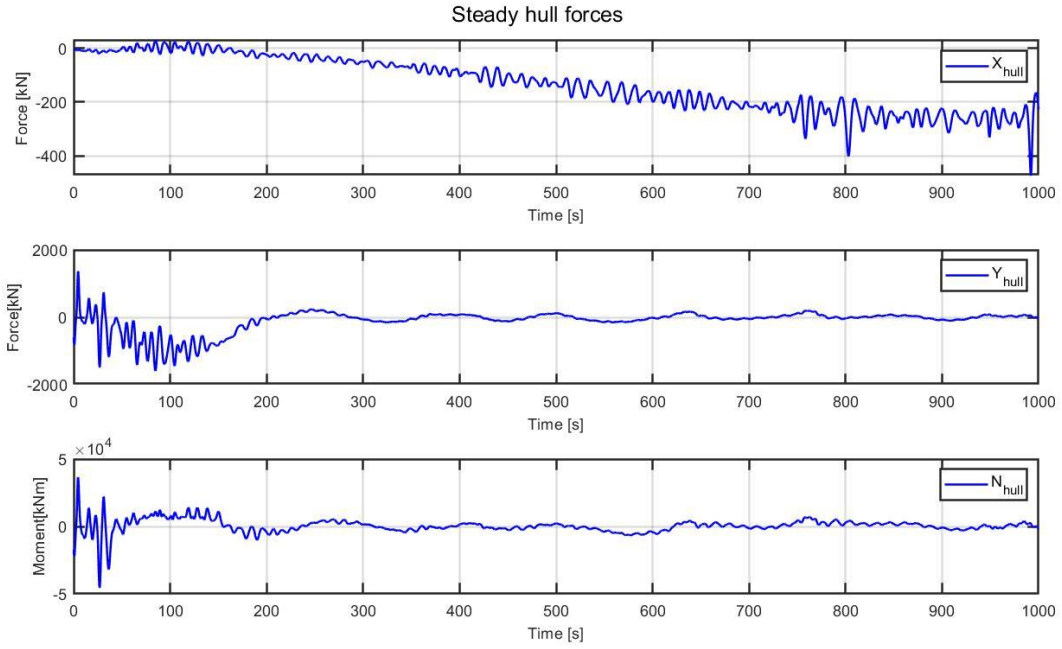

Figure 55: The steady hull forces of the new model in the simulation of the turn into head waves trail in Beaufort 9.

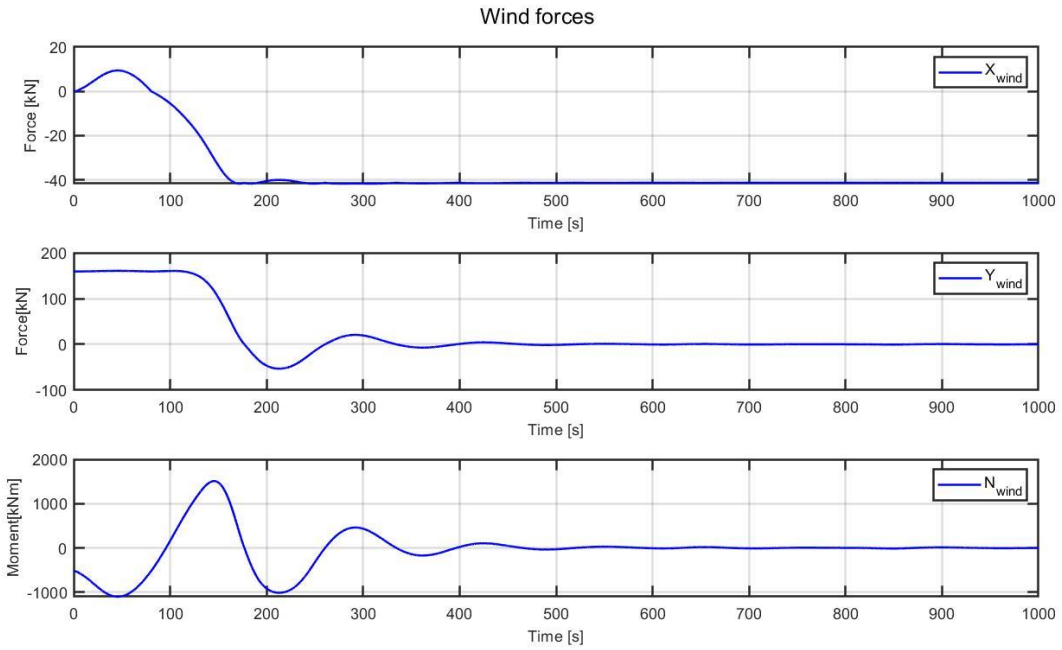

Figure 56: Wind forces of the new model in the simulation of the turn into head waves trail in Beaufort 8.

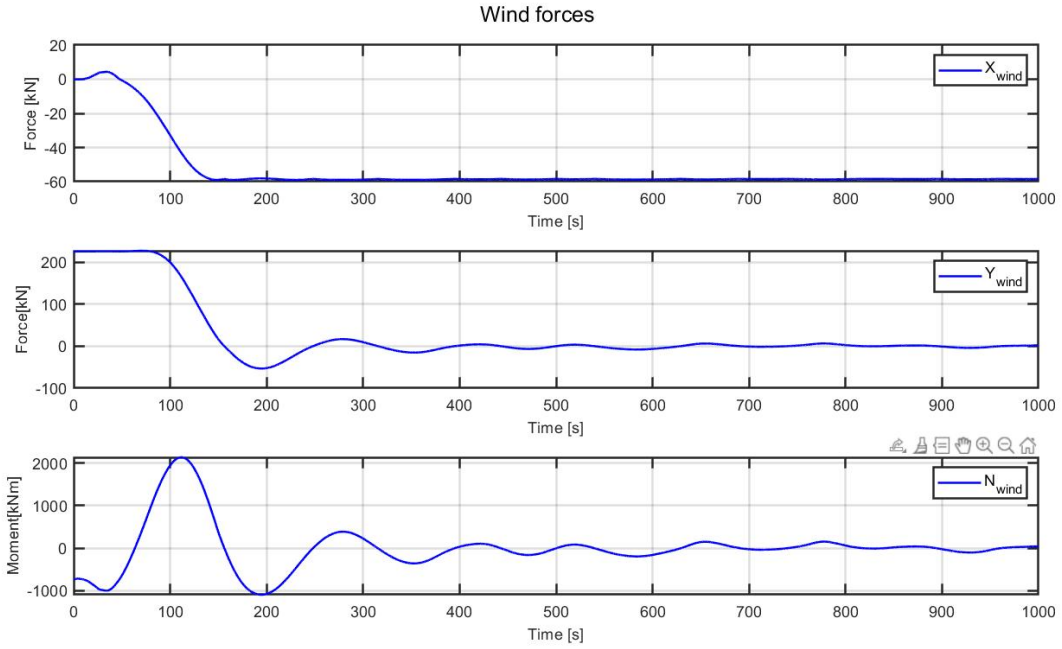

Figure 57: Wind forces of the new model in the simulation of the turn into head waves trail in Beaufort 9.

6.3 Turn into head waves with Reduced Engine Power

In the previous paragraph, it was found that the ship is not low powered as the added resistance in beam waves was over predicted in the original model. Thereof, the question arises what the minimum installed power is to jeopardize the ship. This is investigated by reducing the engine power from 4170kW to subsequently 3170kW, 2670kW, and 2160kW. The simulation as described in the previous section 6.1 is repeated for sea state 9. The results are provided in figure 58 and figure 59. The simulation stops when a negative velocity encountered. With 3170kW, the ship is able to escape the storm. With 2650kW installed, the ship reverses after 265 seconds. This, however, is induced by the wave forces and considering the trend it might have escaped at low speed. With 2170kW installed, a negative trend can be seen in the ships velocity and zero is encountered after 182 seconds. Therefore, it is likely that the ship has insufficient power. It, however, is questionable if the ship is able to reach the design speed with this engine. Therefore, it is concluded that the concerns regarding the underpowering in adverse sea conditions can be relieved.

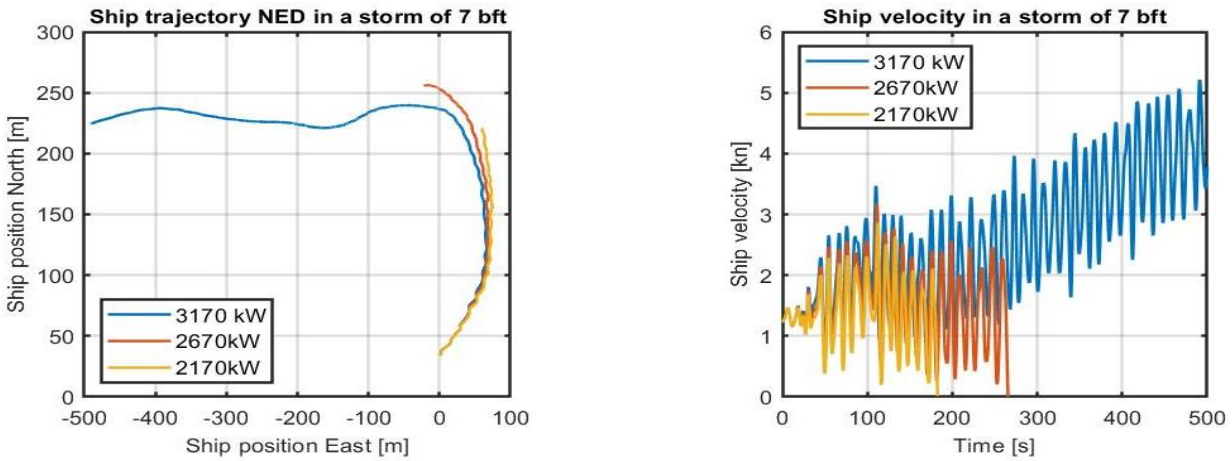

Figure 58: Ship trajectory and velocity in the head turn trail in 9 Beaufort with reduced engine powers.

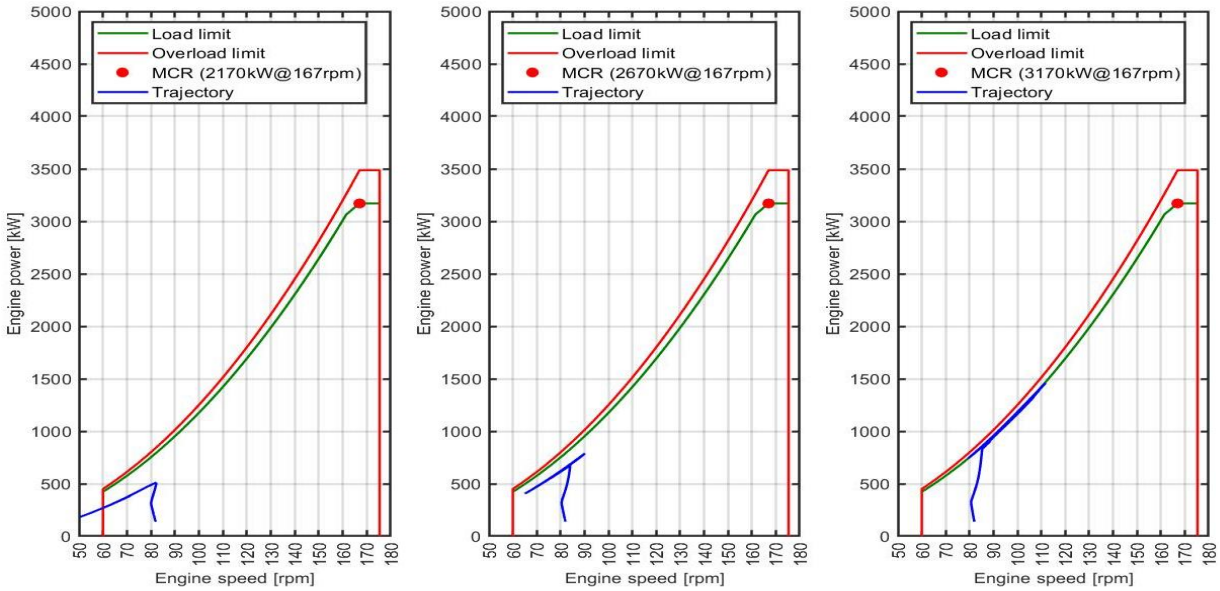

Figure 59: The power trajectory of the engine of the turn against the wind experiment corresponding to figure 58 plotted in the engine envelop with thermal and mechanical limits.

7 Conclusion and Recommendations

This study is conducted as part of a study conducted by Sui (2021) on the required minimum power to maintain manoeuvre capabilities on a benchmark tanker in adverse weather conditions. Therefore, a first principle model is developed from 'tank to wheel'. This model contains sophisticated models to simulate the behaviour of the propulsion system, the electric power generation system, and the hydrodynamics of the ship hull. Subsequently, different propulsion control and energy management configurations can be analysed on their transport performances. The hydrodynamics are modelled with the Kijima model extended with time averaged steady wave forces taken into account as tabular coefficients adopted from Yasukawa et al. (2019). As sophisticated methods are used to model the propulsion system, the desire to improve the fidelity of the hydrodynamic model has been risen. Therefore, the main goal in this thesis is to improve the fidelity of this hydrodynamic model of the Castillo de Tebra created by Sui (2021). The main challenge is that the exact hull geometry is unknown while the wave forces originate from the pressure distribution on the hull wetted surface and thus depend principally on the hull form.

In doing so, the state-of-the-art of combined manoeuvring and seakeeping theory has been scrutinized and four approaches are distinguished; model tests, computational fluid dynamics (CFD), two time-scale approach, and unified approach. To select the method two criteria are formulated:

- The method should improve the fidelity compared to the present wave forces in the manoeuvring model.
- The method should be applicable in the framework of the present model.

The model tests are expensive while the hull geometry is unknown. Presently, it is not possible to perform CFD analysis of ship manoeuvring in waves due to insufficient computational power. Therefore these methods do not meet the second criterion. It is concluded that the two time-scale approaches and the unified approach are applicable. In the two time-scale approaches, the two seakeeping and manoeuvring theory are artificially coupled in different models. The main advantage of this separation is that accurate models of both disciplines can be used without limitations. As a consequence, the selection of the methods seem to be based on availability and not suitability. The unified approaches strive to an amalgamation of the manoeuvring and seakeeping motions in a generic set of rigid body motion equations. Hence, the radiation forces are more consistently included in the unified approach. Thereof, it can be deducted that the decoupling in the two time-scale approaches is inherently a limitation. Therefore, is concluded that a unified approach should be established as the wave forces are taken into account more consistently.

Subsequently, a modular unified approach is established based on the Cummins equation. The steady manoeuvring forces from the Kijima model are taken into account as non-linear damping in the motion equation. The model is extended from three to six degrees of freedom. The first and second order wave excitation forces, the radiation forces, and the hydrodynamic stiffness are implemented. The convolution integrals of the radiation damping forces are circumvented with state space models with the identification method of Perez & Fossen (2009). The input of the forces are the force response amplitude operators, the quadratic transfer functions, and the added mass and damping coefficients in the frequency domain obtained from the diffraction analysis performed in Ansys Aqwa. Moreover, a wave generation model is capable of generating sea surface realizations for irregular waves from multiple wave spectra. In this study irregular long crested waves are generated from a JONSWAP spectrum. The JONSWAP spectrum is generated based on the growth curves of Young and Verhagen (1996a) for fetch limited conditions. Duration limited sea are converted to fetch limited sea based on the study of Dulov et al. (2020). Consequently, the significant wave height and the peak period of the spectrum are taken into account consistently. Thereof, it is concluded that the fidelity of the simulation of the sea conditions is improved.

The new model is validated against the measurements of the turning trail of the full scale benchmark tanker and compared to the original model of Sui (2021). The original model is slightly more accurate, but both results are acceptable. Unfortunately, it must be concluded that the shape of the turning cycle is correct, but that the velocity is slightly overpredicted in the new model. The reason might be the behaviour of the radiation forces when the turning cycle is engaged. The surge, sway and yaw radiation forces and moment opposes the steady hull reaction forces of the fluid. Thereof, the forward velocity is increased and yaw rate are reduced. Hence, the turning cycle is also slightly larger. Nevertheless, the results seem equally acceptable and therefore it is concluded that the models perform equally well.

The ultimate aim in this thesis is to improve the fidelity of the wave model of the simulation of the Castillo de Tebra. The wave forces of the original model are taken into account of a VLCC and in the new model for a barge with the same dimensions of the Castillo de Tebra. The irregular wave forces of the original model are the result of a of model test data in regular waves. The latter can be seen as measured force RAOs. These are used to obtain the steady wave-induced force and moment coefficients which can be seen as wave force spectra. Thereof, these are multiplied with the significant wave height and a peak period. Thereof, the wave conditions involved is an effective regular wave in the time domain. The forces in the new model are derived from the RAOs which are computed with a 3D panel method based on potential flow in the frequency domain. Hence these are also the result of regular waves. The main difference is that the wave forces in the time domain are computed for a large summation of different regular waves. Consequently, the results are for irregular waves. This leads to the conclusion that the fidelity of the measured hydrodynamic forces in regular waves is higher, but that behaviour of the wave forces in the new model is more consistent.

Thereof, the model is used to simulate the conditions in which low powered ships are in danger. Following the Pacha Bulker events, the simulations are compared of a ship that turns from beam waves to head waves at low velocity. The expected result was that in sea state 7 and 8 the ship would survive, but that the ship would fail in sea state 9 as was concluded in Sui (2021). With the new model is was seen that the ship could survive all conditions. The reason is that in the original simulation the ship has a high initial velocity leading to a significant added resistance in beam waves. This effect is not seen in the new model where the added resistance is small in head waves. Therefore, the ship can accelerate and reach the design speed. Consequently, it is concluded that the ship is not underpowered. In order to investigate the minimum power, the engine power is reduced. It was found that the ship became underpowered when half of the original engine power is installed. Consequently, it is questionable if the ship in normal conditions could even reach the design speed.

This result was found for the ship at the design draught. Thereof, the survivability of the ship is increased compared to the reported situations of accidents involving underpowered ships. The endangered ships are waiting to berth and are lightly ballasted. Moreover, the propeller breaks to the water surface and the engine revolutions is manually slowed down to prevent the engine for over speeding (NSW Maritime, 2007). Thereof, the simulation should be executed in ballast conditions with limited engine revolutions. This requires adaptations in the wind model and the Kijima model input, and different results from Ansys Aqwa. Due to the time constraints in finishing this thesis, this is not done. To find the actual minimum power for regulation purposes, it is recommended to do this in the near future.

The new model showed that the fluctuating behaviour of the wave forces have a small effect on the trajectory and the engine power. The fluctuating behaviour is seen in the velocity. Therefore, it could be argued that do not have a zero time average are required. The aim of implementing all the wave forces and to extent the degrees of freedom was to correct the steady manoeuvring forces of the Kijima model for the actual orientation of the ship, i.e. trim and heave. Due to the time frame of the study this goal is not met and it is recommended to do this in the future. Besides, similar forces as in the Kijima model might exist for the heave, roll, and pitch degree of freedom.

Moreover, limited time is spend on discovering the versatile options of Ansys Aqwa. Consequently, the diffraction analysis is performed for deep water at zero speed. Therefore, the simulation can be improved when the diffraction results are obtained for a range of velocities and water depths. Also, the quality of the results can improved when the frequency range is increased.

For the roll motion, the damping is vicious dominated and only the potential damping obtained from Ansys Aqwa is included in the model. Therefore, this damping is underpredicted. The natural period of roll is generally in the wave frequency range and therefore large motions and forces are introduced. Via the hydrodynamic coupling this also leads to large motions and forces in other degrees of freedom. Therefore, it is recommended to include viscous roll damping based on the Ikeda method as the roll motions are overpredicted.

Moreover, instabilities in the new model might appear as no attention is given to the navigation controls. The engine, propeller pitch and heading control acts on all variations in velocity and heading. In example, the rudder angle does not have to be controlled for all first order heading changes, although it might be used as motion reducing device in large waves. Nevertheless, all models are influenced by these fluctuations and this might affect the accuracy of some models. Therefore, the results might improve when the PID-controllers are tuned and a wave filter is implemented.

Lastly, a recommendation for a future study is to validate the simulation with another ship of which hull form is known, in example the KVLCC2. This is ship model developed for study purposes and extensive literature is available on this ship. The lines plan is available and the ship can be made underpowered by selecting the engine parameters accordingly. Thereof, all models in the simulation can be validated based on the results of the other studies.

Appendix A

This appendix contains plots of the convolution realizations from equation 4-15 and 4-17 and the reconstructed added mass and damping from equation 4-22 below. Due to the symmetry only the coefficients of the upper half of the added mass and damping matrix are provided, see equations 4-7 and 4-8.

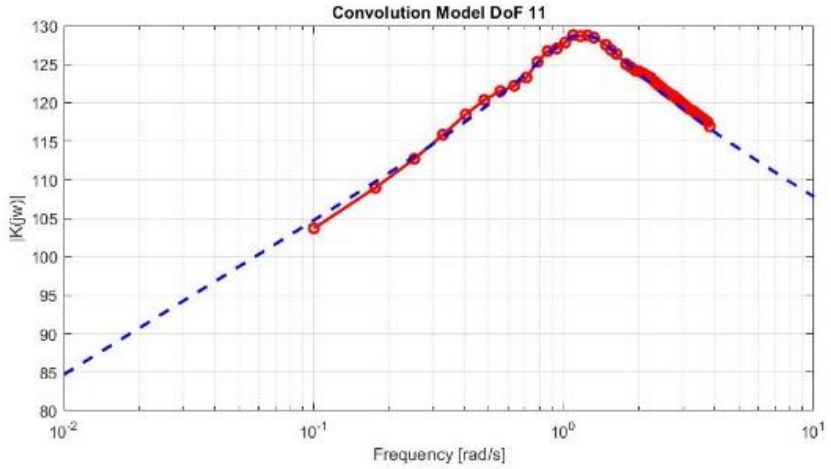
Convolution Model DoF 11
|K(jw)|
Frequency [rad/s]

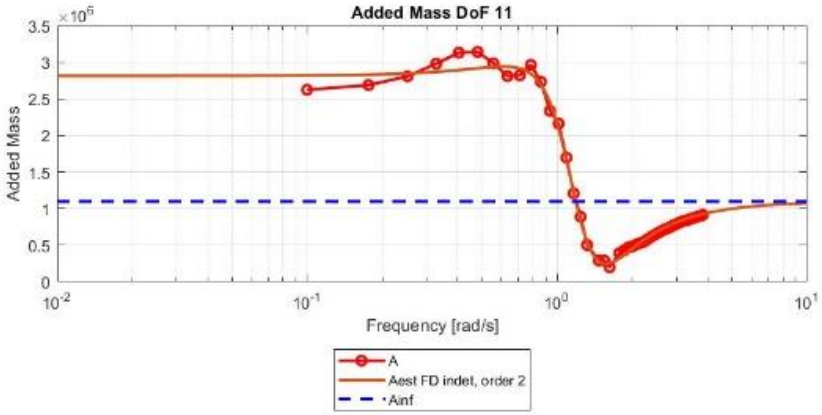
Added Mass DoF 11
Added Mass
Frequency [rad/s]
A
Aest FD indet, order 2
Ainf

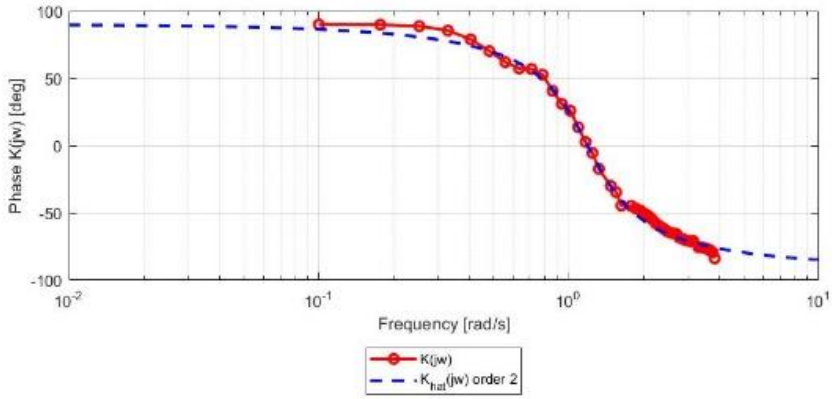
Phase K(jw) [deg]
Frequency [rad/s]
K(jw)
K_hat(jw) order 2

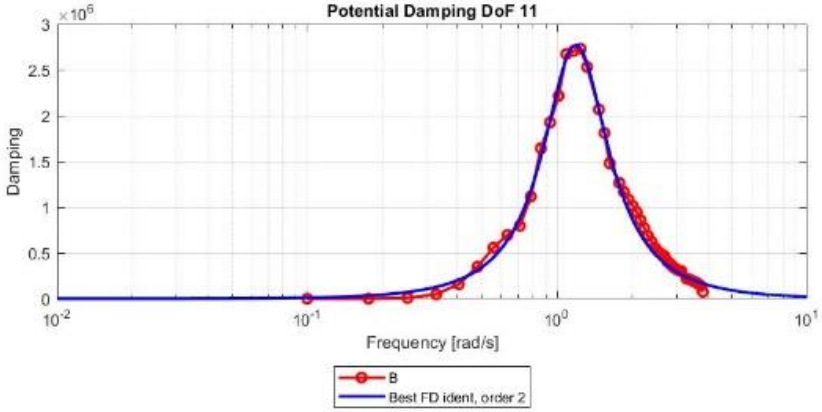
Potential Damping DoF 11
Damping
Frequency [rad/s]
B
Best FD ident, order 2

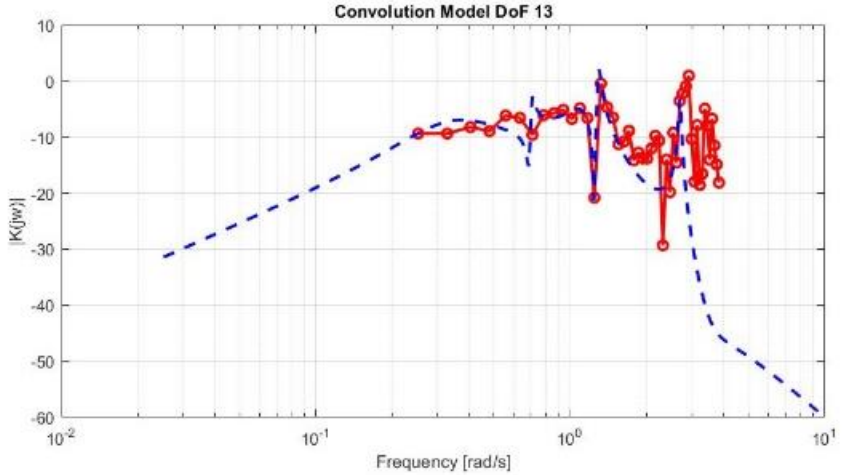
Convolution Model DoF 13
|K(jw)|
Frequency [rad/s]

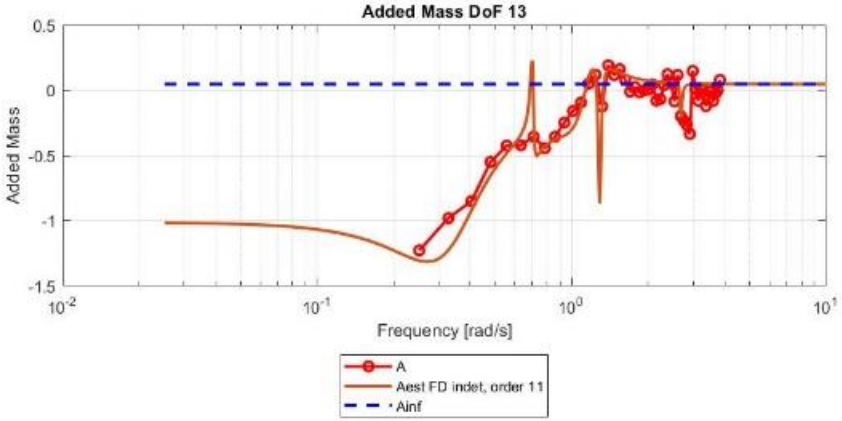
Added Mass DoF 13
Added Mass
Frequency [rad/s]
A
Aest FD indet, order 11
Ainf

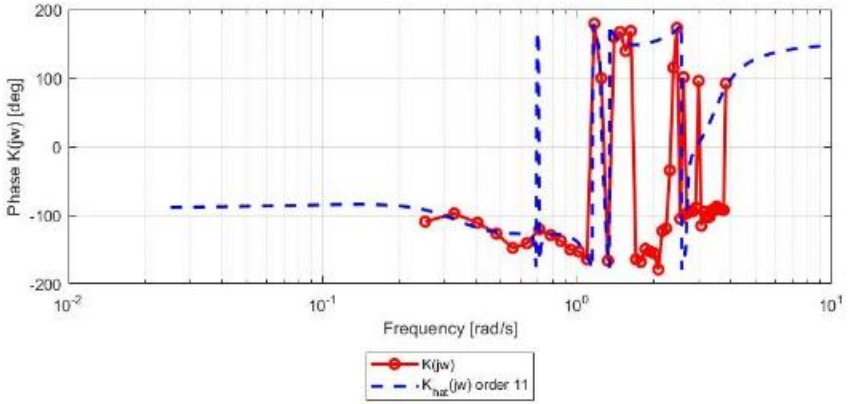
Phase K(jw) [deg]
Frequency [rad/s]
K(jw)
K_hat(jw) order 11

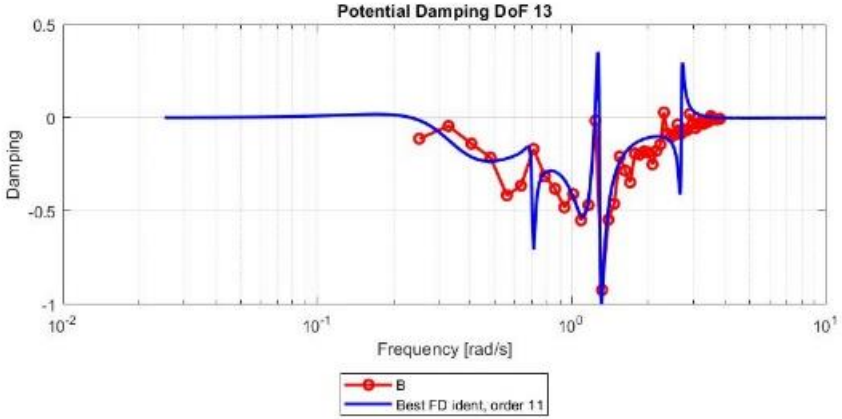
Potential Damping DoF 13
Damping
Frequency [rad/s]
B
Best FD ident, order 11

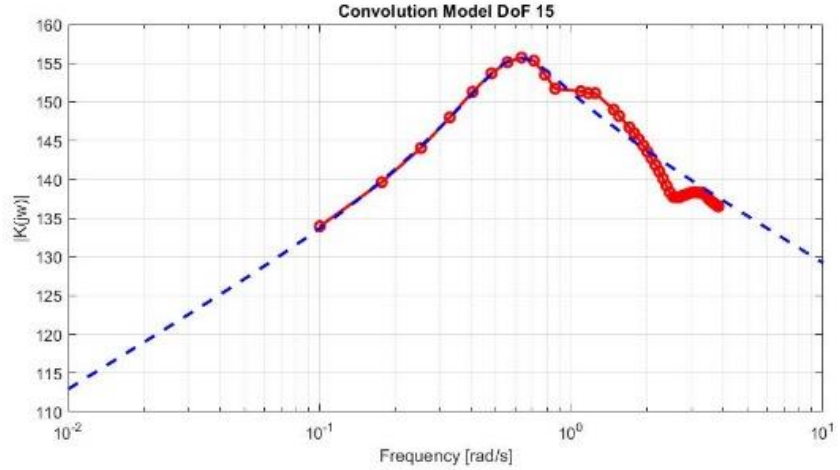
Convolution Model DoF 15
|K(jw)|
Frequency [rad/s]

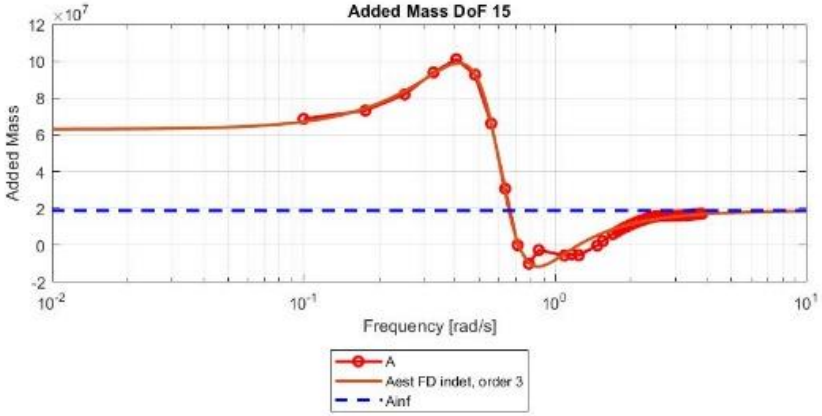
Added Mass DoF 15
Added Mass
Frequency [rad/s]
A
Aest FD indet, order 3
Ainf

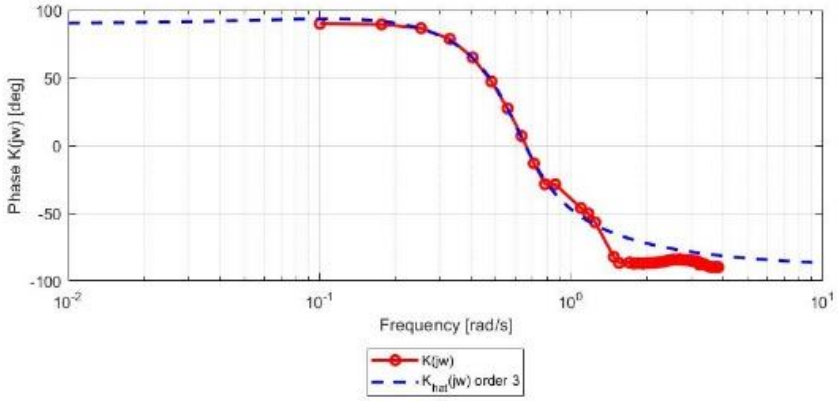
Phase K(jw) [deg]
Frequency [rad/s]
K(jw)
K_hat(jw) order 3

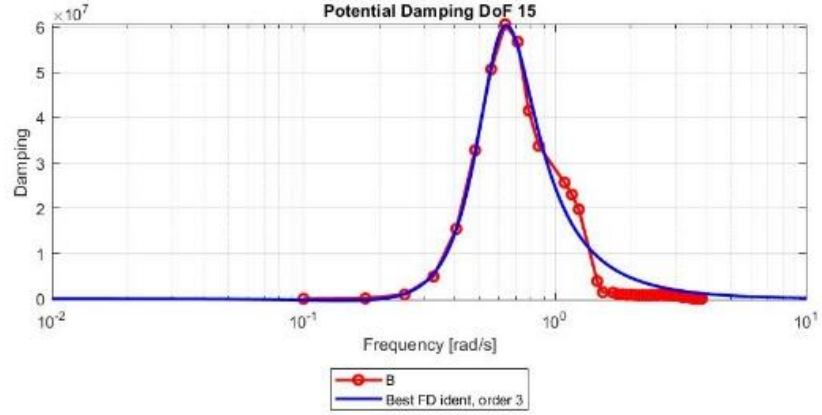
Potential Damping DoF 15
Damping
Frequency [rad/s]
B
Best FD ident, order 3

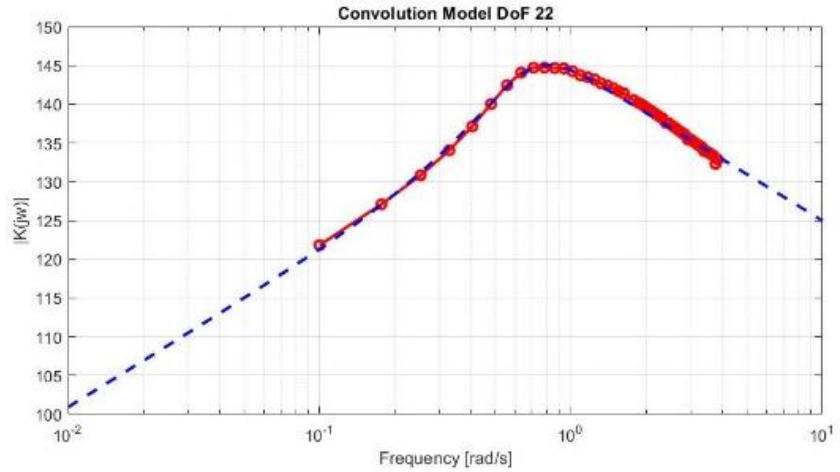
Convolution Model DoF 22
|K(jw)|
Frequency [rad/s]

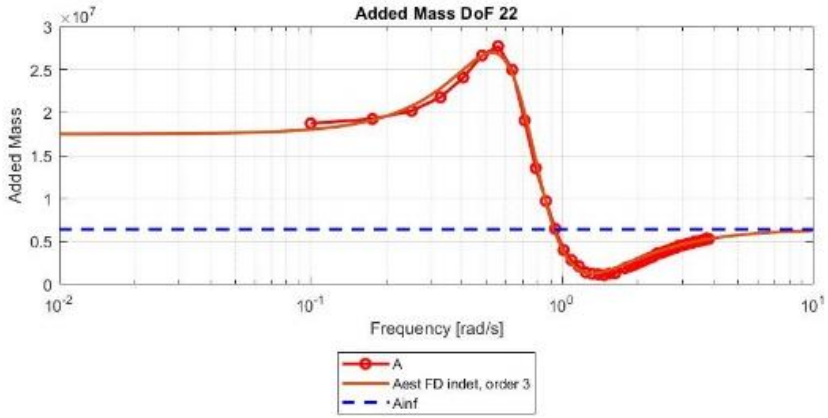
Added Mass DoF 22
Added Mass
Frequency [rad/s]
A
Aest FD indet, order 3
Ainf

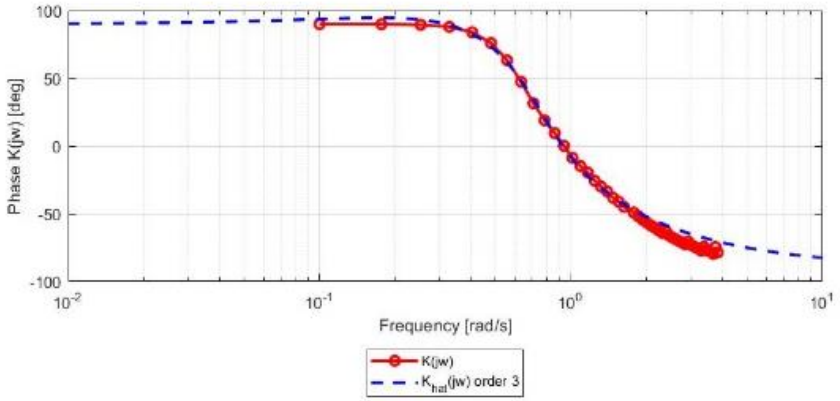
Phase K(jw) [deg]
Frequency [rad/s]
K(jw)
K_hat(jw) order 3

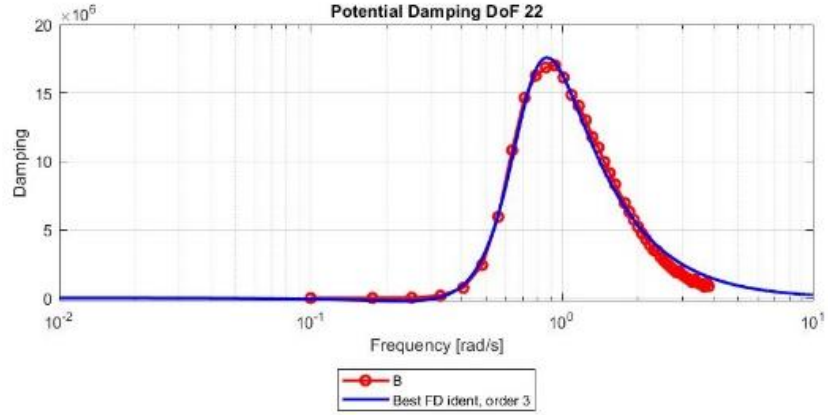
Potential Damping DoF 22
Damping
Frequency [rad/s]
B
Best FD ident, order 3

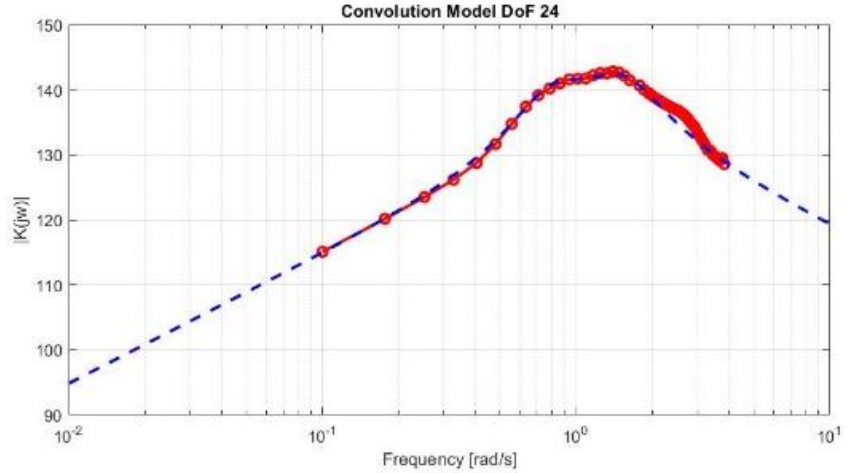
Convolution Model DoF 24
|K(jw)|
Frequency [rad/s]

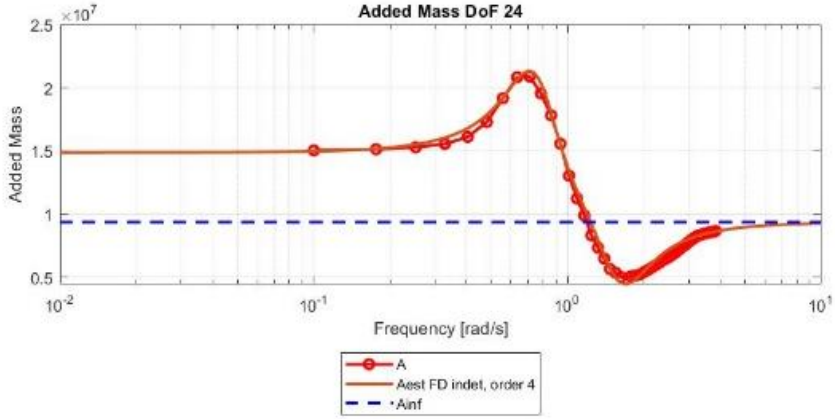
Added Mass DoF 24
Added Mass
Frequency [rad/s]
A
Aest FD indet, order 4
Ainf

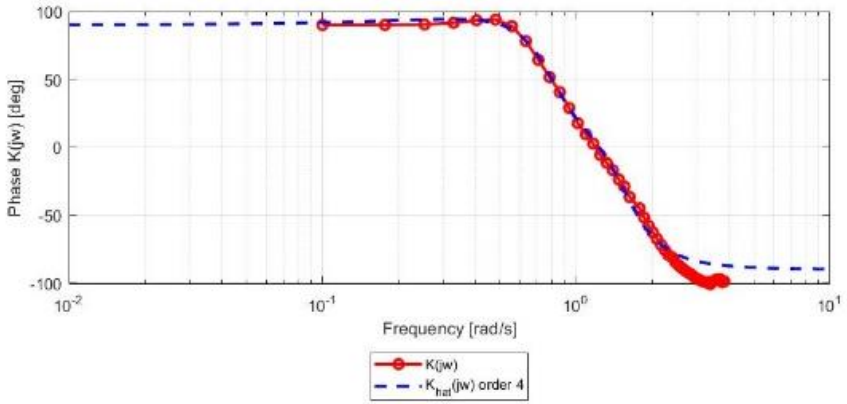
Phase K(jw) [deg]
Frequency [rad/s]
K(jw)
K_hat(jw) order 4

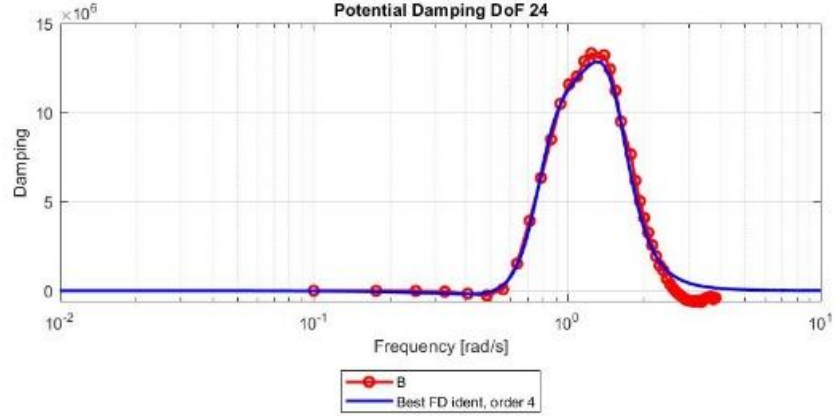
Potential Damping DoF 24
Damping
Frequency [rad/s]
B
Best FD ident, order 4

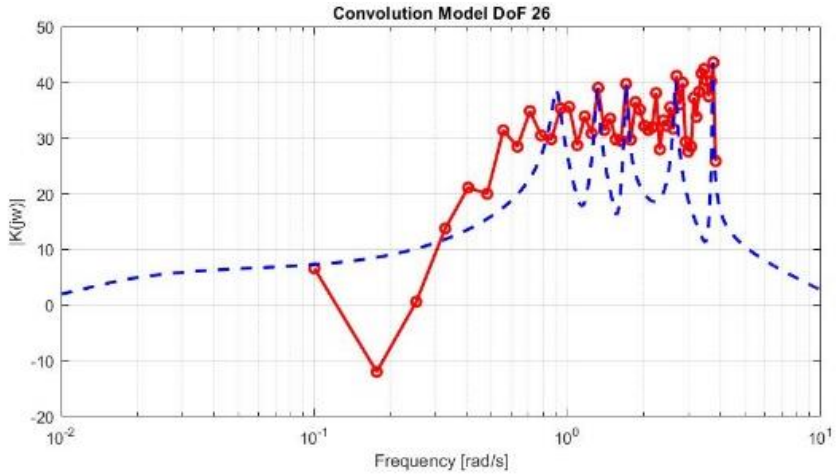
Convolution Model DoF 26
|K(jw)|
Frequency [rad/s]

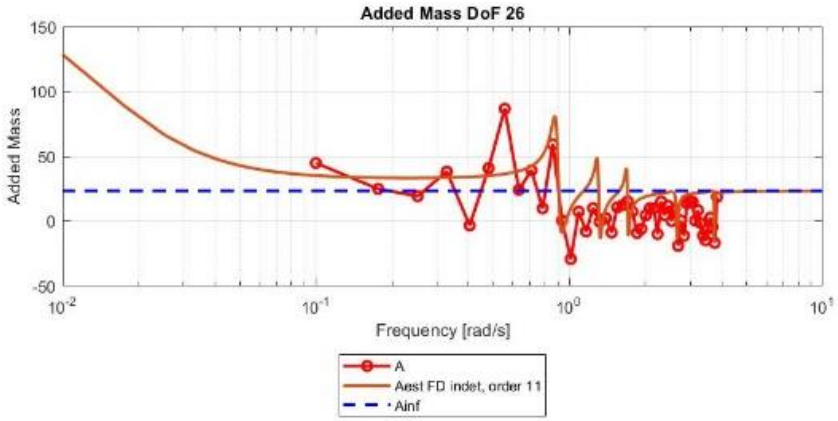
Added Mass DoF 26
Added Mass
Frequency [rad/s]
A
Aest FD indet, order 11
Ainf

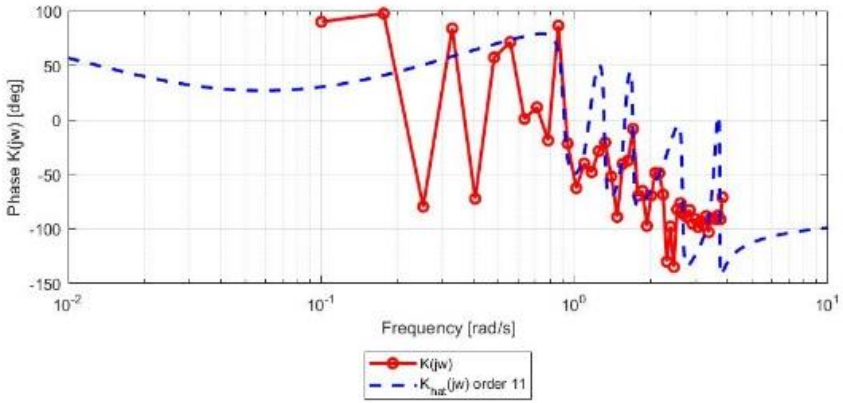
Phase K(jw) [deg]
Frequency [rad/s]
K(jw)
K_hat(jw) order 11

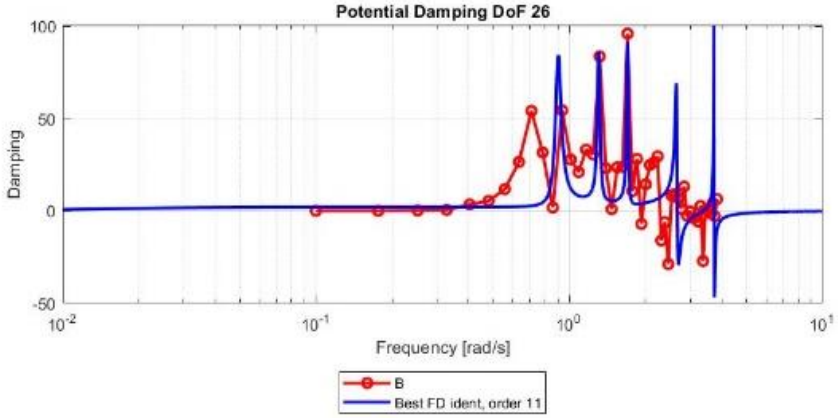
Potential Damping DoF 26
Damping
Frequency [rad/s]
B
Best FD ident, order 11

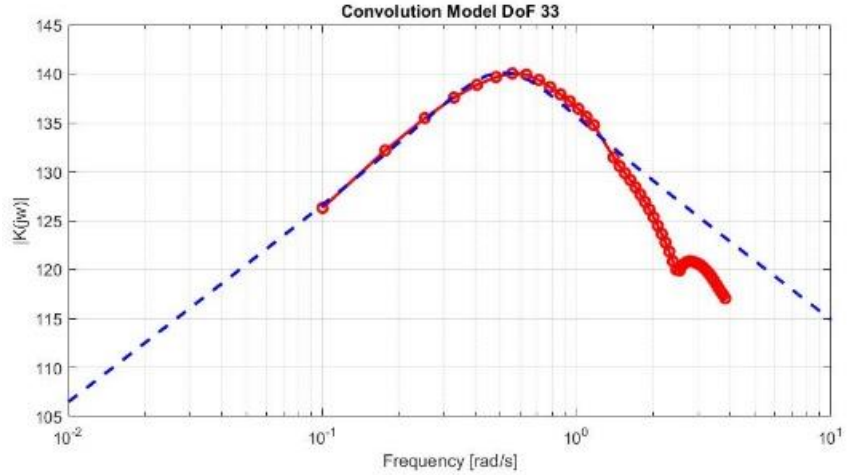
Convolution Model DoF 33
|K(jw)|
Frequency [rad/s]

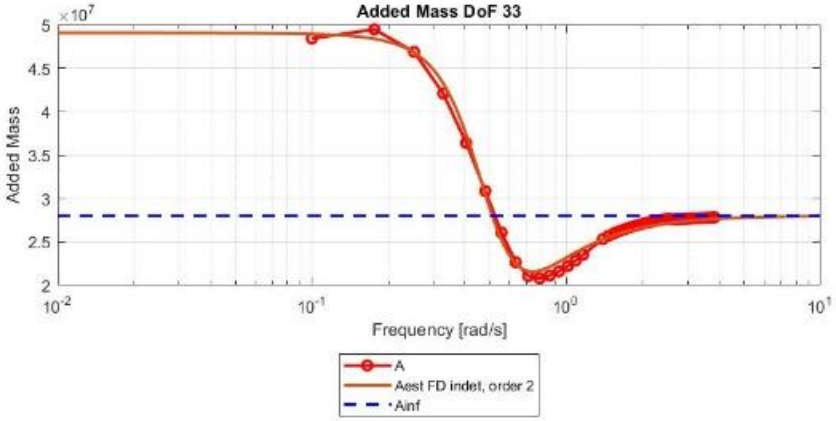
Added Mass DoF 33
Added Mass
Frequency [rad/s]
A
Aest FD indet, order 2
Ainf

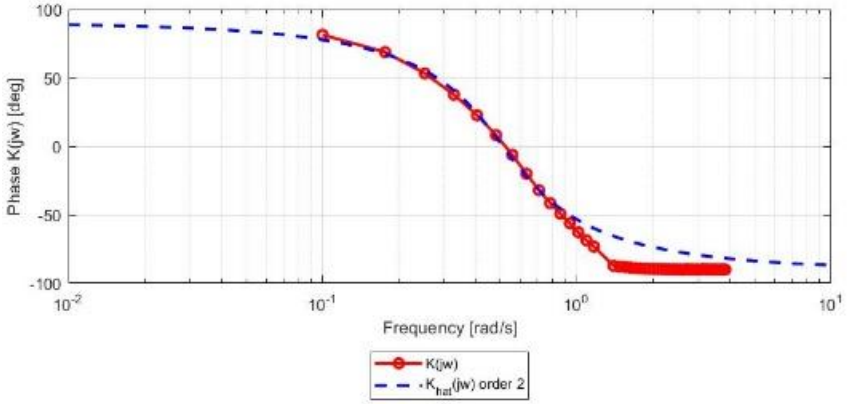
Phase K(jw) [deg]
Frequency [rad/s]
K(jw)
K_hat(jw) order 2

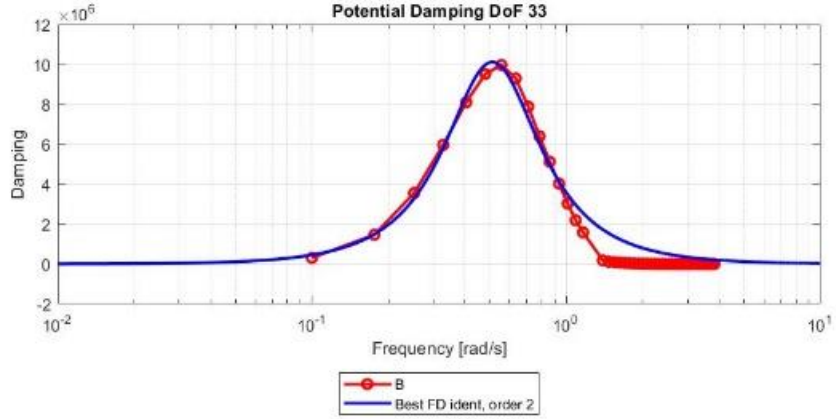
Potential Damping DoF 33
Damping
Frequency [rad/s]
B
Best FD ident, order 2

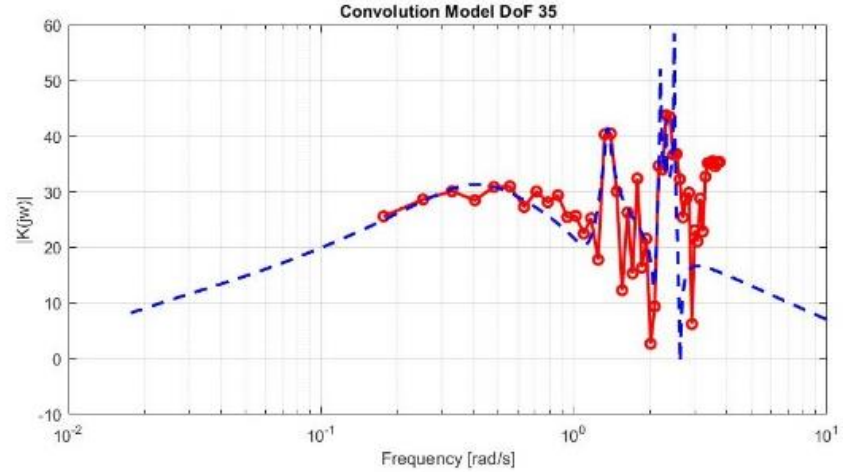
Convolution Model DoF 35
|K(jw)|
Frequency [rad/s]

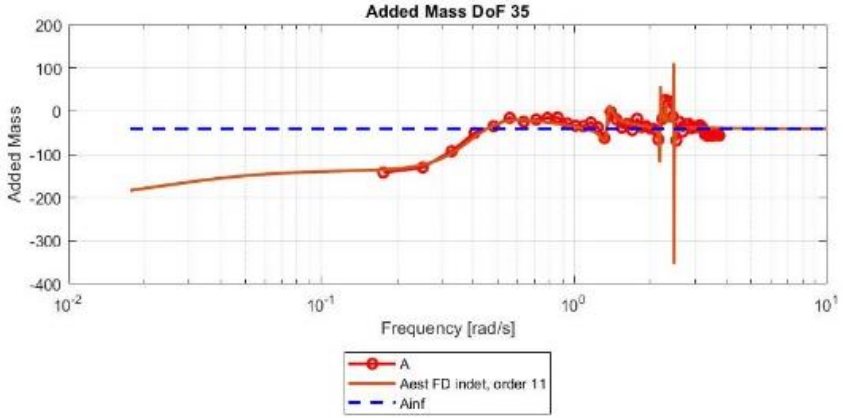
Added Mass DoF 35
Added Mass
Frequency [rad/s]
A
Aest FD indet, order 11
Ainf

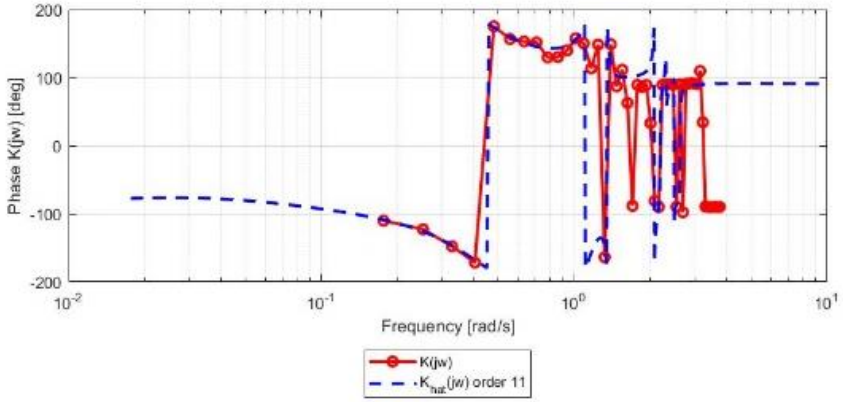
Phase K(jw) [deg]
Frequency [rad/s]
K(jw)
K_hat(jw) order 11

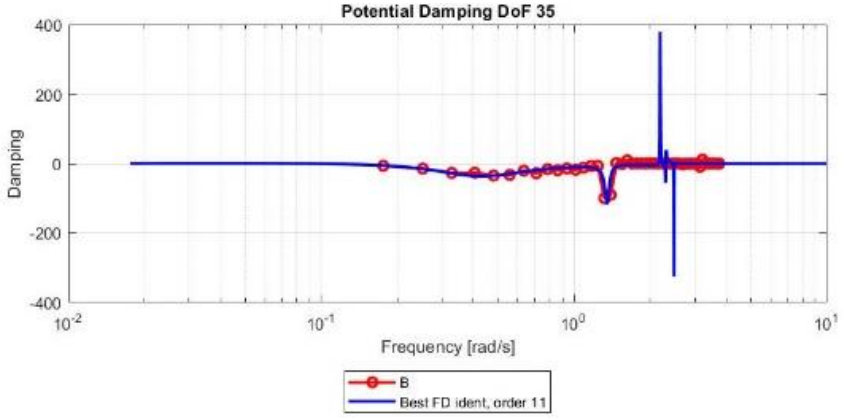
Potential Damping DoF 35
Damping
Frequency [rad/s]
B
Best FD ident, order 11

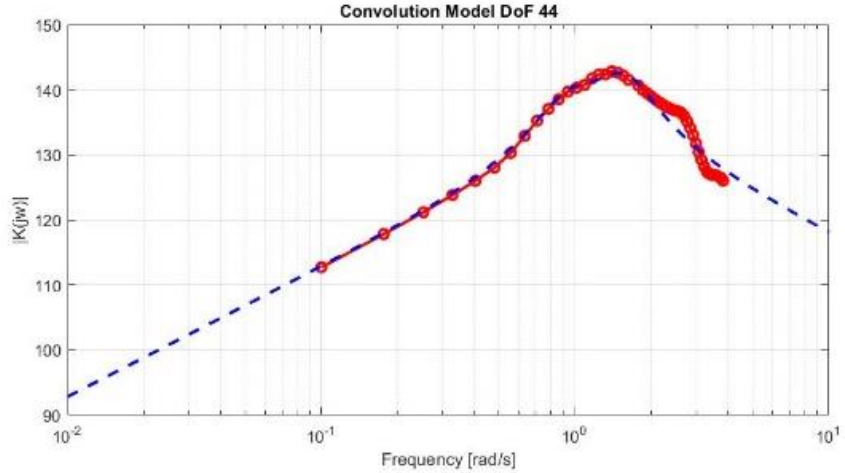
Convolution Model DoF 44
|K(jw)|
Frequency [rad/s]

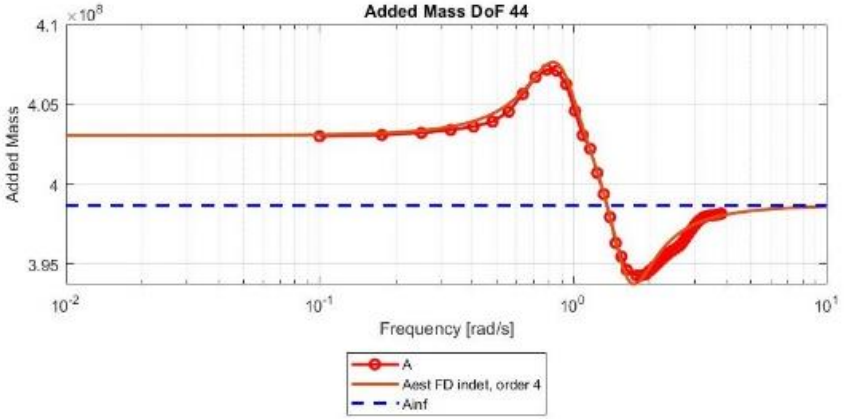
Added Mass DoF 44
Added Mass
Frequency [rad/s]
A
Aest FD indet, order 4
Ainf

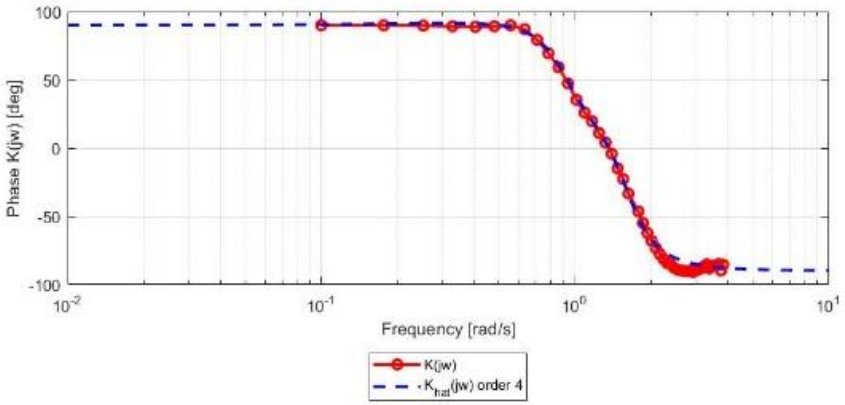
Phase K(jw) [deg]
Frequency [rad/s]
K(jw)
K_hat(jw) order 4

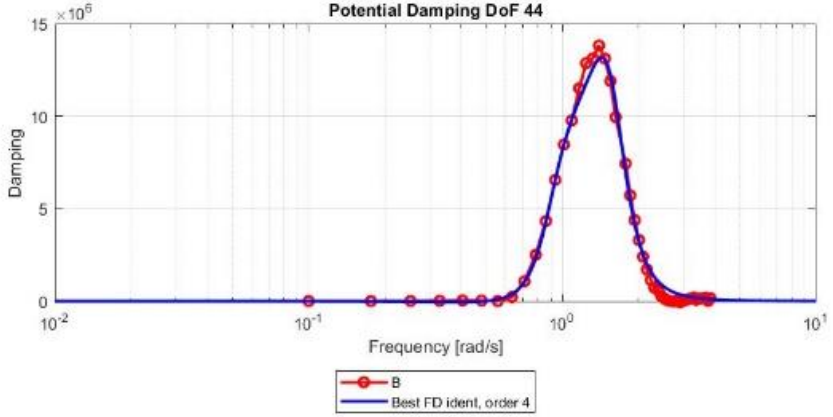
Potential Damping DoF 44
Damping
Frequency [rad/s]
B
Best FD ident, order 4

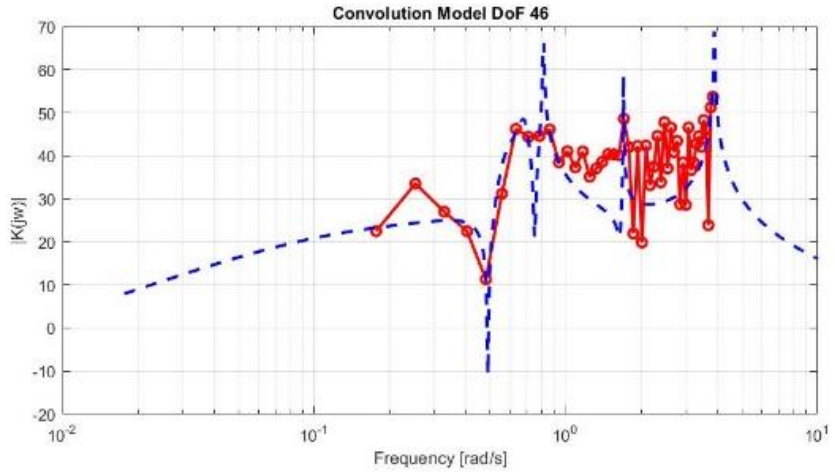
Convolution Model DoF 46
|K(jw)|
Frequency [rad/s]

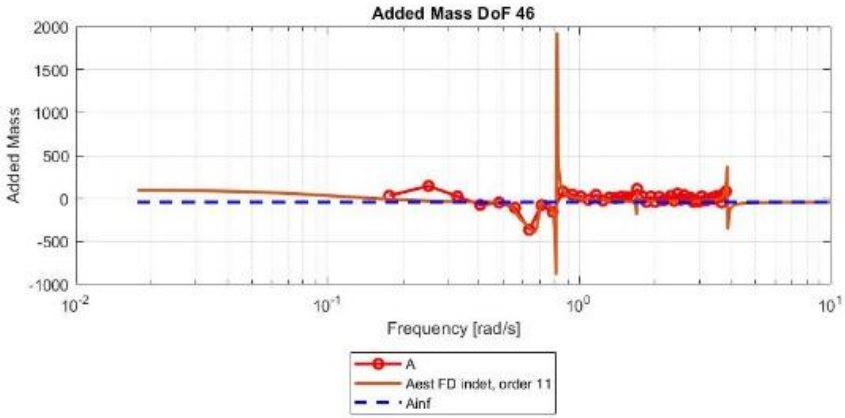
Added Mass DoF 46
Added Mass
Frequency [rad/s]
A
Aest FD indet, order 11
Ainf

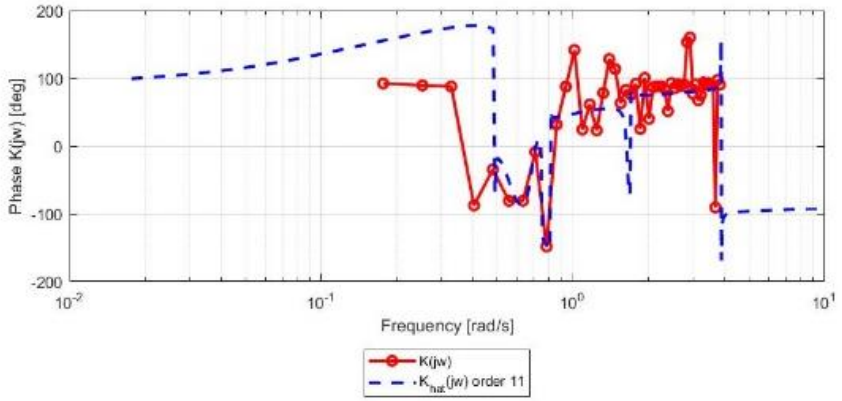
Phase K(jw) [deg]
Frequency [rad/s]
K(jw)
K_hat(jw) order 11

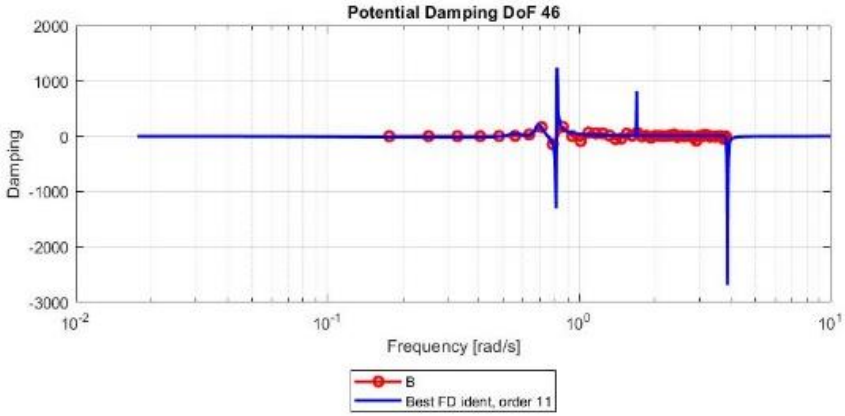
Potential Damping DoF 46
Damping
Frequency [rad/s]
B
Best FD ident, order 11

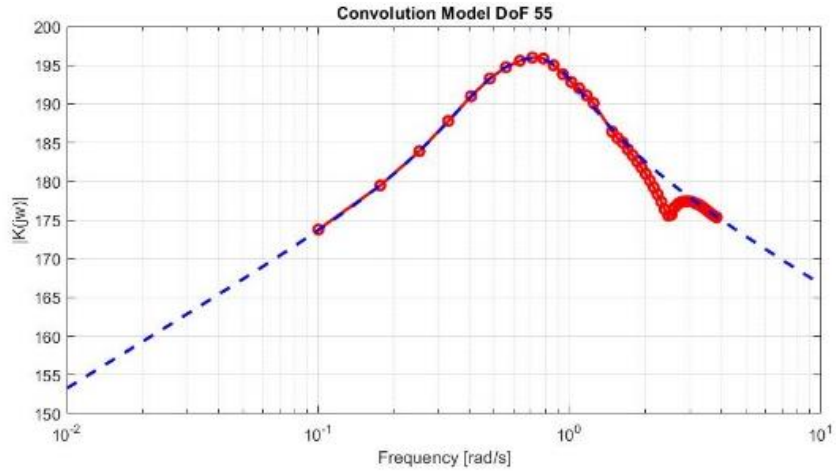
Convolution Model DoF 55
|K(jw)|
Frequency [rad/s]

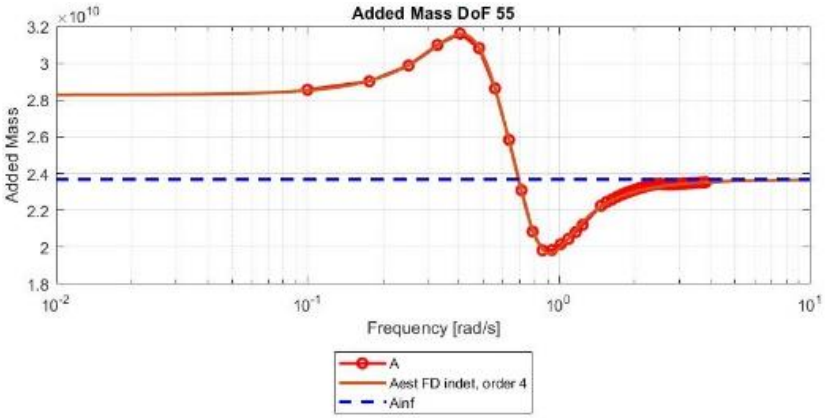
Added Mass DoF 55
Added Mass
Frequency [rad/s]
A
Aest FD indet, order 4
Ainf

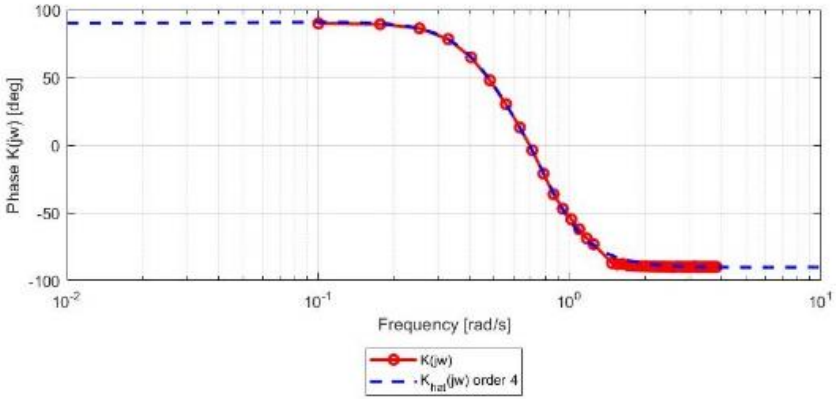
Phase K(jw) [deg]
Frequency [rad/s]
K(jw)
K_hat(jw) order 4

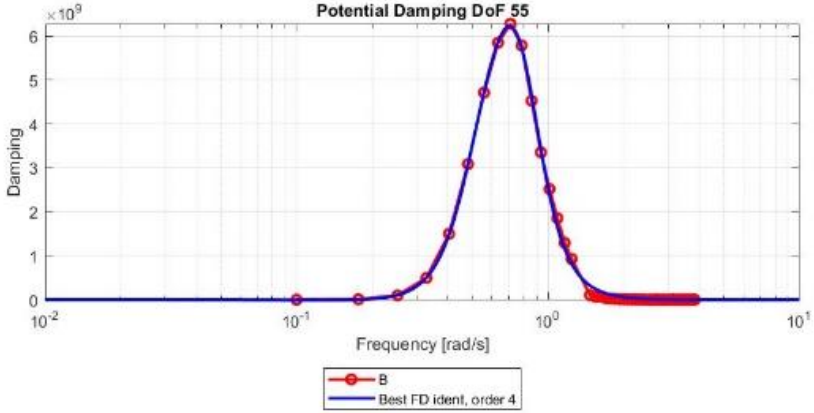
Potential Damping DoF 55
Damping
Frequency [rad/s]
B
Best FD ident, order 4

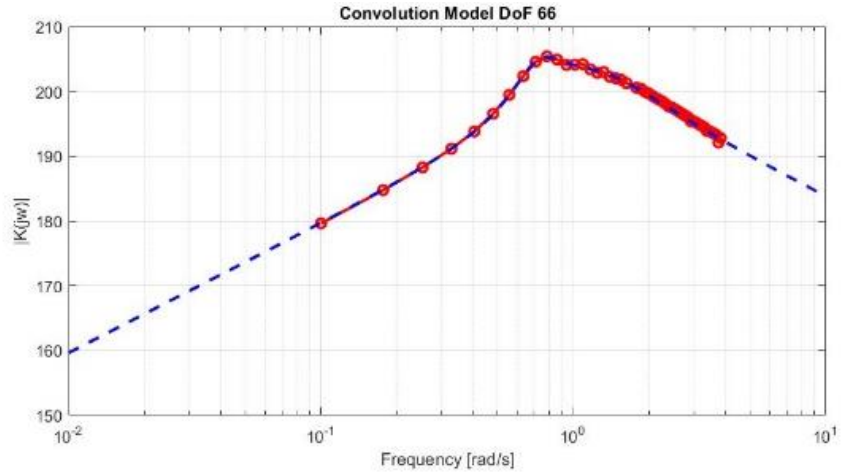
Convolution Model DoF 66
|K(jw)|
Frequency [rad/s]

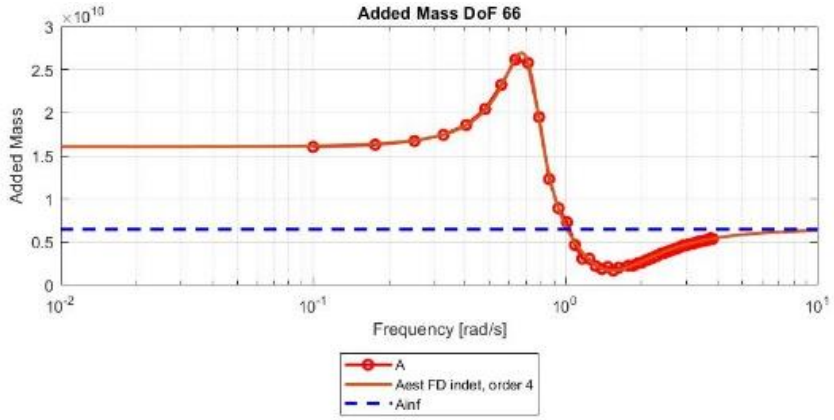
Added Mass DoF 66
Added Mass
Frequency [rad/s]
A
Aest FD indet, order 4
Ainf

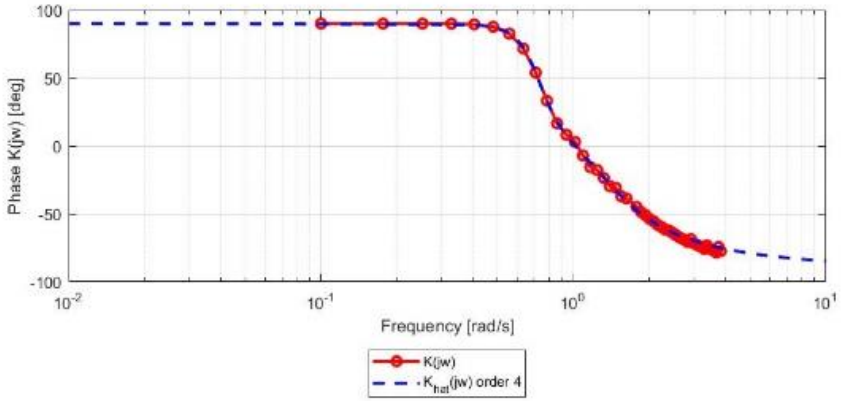
Phase K(jw) [deg]
Frequency [rad/s]
K(jw)
K_hat(jw) order 4

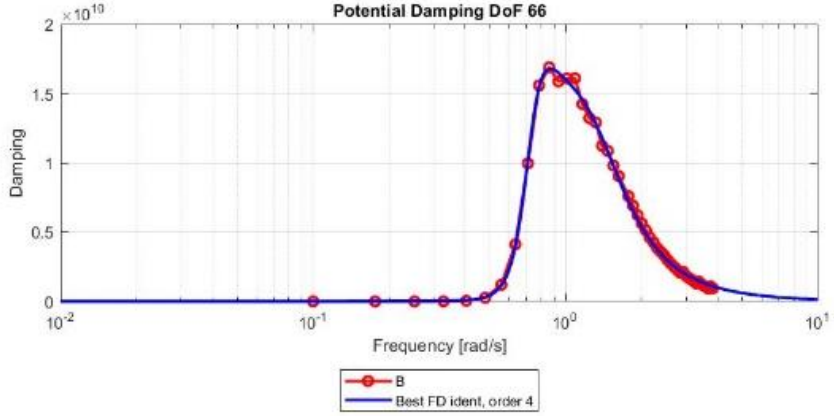
Potential Damping DoF 66
Damping
Frequency [rad/s]
B
Best FD ident, order 4

Appendix B

This appendix shows wind velocity and significant wave height included in the wind and wave model of Sui (2021) and the North Atlantic Scatter.

BEAUFORT SCALE OF WIND

BEAUFORT NUMBER	DESCRIPTIVE TERM	VELOCITY EQUIVALENT AT A STANDARD HEIGHT OF 10 METRES ABOVE OPEN FLAT GROUND				SPECIFICATIONS			Probable wave height* in metres	Probable wave height* in feet
		Mean velocity in knots	m s^{-1}	km h^{-1}	m.p.h.	Land	Sea	Coast		
0	Calm	< 1	0–0.2	< 1	< 1	Calm; smoke rises vertically	Sea like a mirror	Calm	—	—
1	Light air	1–3	0.3–1.5	1–5	1–3	Direction of wind shown by smoke drift but not by wind vanes	Ripples with the appearance of scales are formed, but without foam crests	Fishing smack just has steerage way	0.1 (0.1)	1/4 (1/4)
2	Light breeze	4–6	1.6–3.3	6–11	4–7	Wind felt on face; leaves rustle; ordinary vanes moved by wind	Small wavelets, still short but more pronounced; crests have a glassy appearance and do not break	Wind fills the sails of smacks which then travel at about 1–2 knots	0.2 (0.3)	1/2 (1)
3	Gentle breeze	7–10	3.4–5.4	12–19	8–12	Leaves and small twigs in constant motion; wind extends light flag	Large wavelets; crests begin to break; foam of glassy appearance; perhaps scattered white horses	Smacks begin to careen and travel about 3–4 knots	0.6 (1)	2 (3)
4	Moderate breeze	11–16	5.5–7.9	20–28	13–18	Raises dust and loose paper; small branches are moved	Small waves, becoming longer; fairly frequent white horses	Good working breeze, smacks carry all canvas with good list	1 (1.5)	3 1/2 (5)
5	Fresh breeze	17–21	8.0–10.7	29–38	19–24	Small trees in leaf begin to sway; crested wavelets form on inland waters	Moderate waves, taking a more pronounced long form; many white horses are formed (chance of some spray)	Smacks shorten sail	2 (2.5)	6 (8 1/2)
6	Strong breeze	22–27	10.8–13.8	39–49	25–31	Large branches in motion; whistling heard in telegraph wires; umbrellas used with difficulty	Large waves begin to form; the white foam crests are more extensive everywhere (probably some spray)	Smacks have double reef in mainsail; care required when fishing	3 (4)	9 1/2 (13)
7	Near gale	28–33	13.9–17.1	50–61	32–38	Whole trees in motion; inconvenience felt when walking against wind	Sea heaps up and white foam from breaking waves begins to be blown in streaks along the direction of the wind	Smacks remain in harbour and those at sea lie to	4 (5.5)	13 1/2 (19)
8	Gale	34–40	17.2–20.7	62–74	39–46	Breaks twigs off trees; generally impedes progress	Moderately high waves of greater length; edges of crests begin to break into the spindrift; the foam is blown in well-marked streaks along the direction of the wind	All smacks make for harbour, if near	5.5 (7.5)	18 (25)
9	Strong gale	41–47	20.8–24.4	75–88	47–54	Slight structural damage occurs (chimney pots and slates removed)	High waves; dense streaks of foam along the direction of the wind; crests of waves begin to topple, tumble and roll over; spray may affect visibility	—	7 (10)	23 (32)
10	Storm	48–55	24.5–28.4	89–102	55–63	Seldom experienced inland; trees uprooted; considerable structural damage occurs	Very high waves with long overhanging crests; the resulting foam, in great patches, is blown in dense white streaks along the direction of the wind; on the whole, the surface of the sea takes on a white appearance; the tumbling of the sea becomes heavy and shock-like; visibility affected	—	9 (12.5)	29 (41)
11	Violent storm	56–63	28.5–32.6	103–117	64–72	Very rarely experienced; accompanied by widespread damage	Exceptionally high waves (small and medium-sized ships might be for a time lost to view behind the waves); the sea is completely covered with long white patches of foam lying along the direction of the wind; everywhere the edges of the wave crests are blown into froth; visibility affected	—	11.5 (16)	37 (52)
12	Hurricane	64 and over	32.7 and over	118 and over	73 and over	—	The air is filled with foam and spray; sea completely white with driving spray; visibility very seriously affected	—	14 (—)	45 (—)

* This table is only intended as a guide to show roughly what may be expected in the open sea, remote from land. It should never be used in the reverse way; i.e., for logging or reporting the state of the sea. In enclosed waters, or when near land, with an offshore wind, wave heights will be smaller and the waves steeper. Figures in brackets indicate the probable maximum height of waves.

Volume I.1 **A–379**

Figure 60: The Beaufort wind scale as defined in section 3 of the regulations of World Meteorological Organization (2017).

Table 1, Probability of sea-states in the North Atlantic described as occurrence per 100000 observations.
Derived from BMT's Global Wave Statistics

Hs/Tz	1.5	2.5	3.5	4.5	5.5	6.5	7.5	8.5	9.5	10.5	11.5	12.5	13.5	14.5	15.5	16.5	17.5	18.5	SUM
0.5	0.0	0.0	1.3	133.7	865.6	1186.0	634.2	186.3	36.9	5.6	0.7	0.1	0.0	0.0	0.0	0.0	0.0	0.0	3050
1.5	0.0	0.0	0.0	29.3	986.0	4976.0	7738.0	5569.7	2375.7	703.5	160.7	30.5	5.1	0.8	0.1	0.0	0.0	0.0	22575
2.5	0.0	0.0	0.0	2.2	197.5	2158.8	6230.0	7449.5	4860.4	2066.0	644.5	160.2	33.7	6.3	1.1	0.2	0.0	0.0	23810
3.5	0.0	0.0	0.0	0.2	34.9	695.5	3226.5	5675.0	5099.1	2838.0	1114.1	337.7	84.3	18.2	3.5	0.6	0.1	0.0	19128
4.5	0.0	0.0	0.0	0.0	6.0	196.1	1354.3	3288.5	3857.5	2685.5	1275.2	455.1	130.9	31.9	6.9	1.3	0.2	0.0	13289
5.5	0.0	0.0	0.0	0.0	1.0	51.0	498.4	1602.9	2372.7	2008.3	1126.0	463.6	150.9	41.0	9.7	2.1	0.4	0.1	8328
6.5	0.0	0.0	0.0	0.0	0.2	12.6	167.0	690.3	1257.9	1268.6	825.9	386.8	140.8	42.2	10.9	2.5	0.5	0.1	4806
7.5	0.0	0.0	0.0	0.0	0.0	3.0	52.1	270.1	594.4	703.2	524.9	276.7	111.7	36.7	10.2	2.5	0.6	0.1	2586
8.5	0.0	0.0	0.0	0.0	0.0	0.7	15.4	97.9	255.9	350.6	296.9	174.6	77.6	27.7	8.4	2.2	0.5	0.1	1309
9.5	0.0	0.0	0.0	0.0	0.0	0.2	4.3	33.2	101.9	159.9	152.2	99.2	48.3	18.7	6.1	1.7	0.4	0.1	626
10.5	0.0	0.0	0.0	0.0	0.0	0.0	1.2	10.7	37.9	67.5	71.7	51.5	27.3	11.4	4.0	1.2	0.3	0.1	285
11.5	0.0	0.0	0.0	0.0	0.0	0.0	0.3	3.3	13.3	26.6	31.4	24.7	14.2	6.4	2.4	0.7	0.2	0.1	124
12.5	0.0	0.0	0.0	0.0	0.0	0.0	0.1	1.0	4.4	9.9	12.8	11.0	6.8	3.3	1.3	0.4	0.1	0.0	51
13.5	0.0	0.0	0.0	0.0	0.0	0.0	0.0	0.3	1.4	3.5	5.0	4.6	3.1	1.6	0.7	0.2	0.1	0.0	21
14.5	0.0	0.0	0.0	0.0	0.0	0.0	0.0	0.1	0.4	1.2	1.8	1.8	1.3	0.7	0.3	0.1	0.0	0.0	8
15.5	0.0	0.0	0.0	0.0	0.0	0.0	0.0	0.0	0.1	0.4	0.6	0.7	0.5	0.3	0.1	0.1	0.0	0.0	3
16.5	0.0	0.0	0.0	0.0	0.0	0.0	0.0	0.0	0.0	0.1	0.2	0.2	0.2	0.1	0.1	0.0	0.0	0.0	1
SUM:	0	0	1	165	2091	9280	19922	24879	20870	12898	6245	2479	837	247	66	16	3	1	100000

The Hs and Tz values are class midpoints.

Figure 61: North Atlantic long term wave scatter (International Association of Classification Societies, 2001).

List of Figures

List of Tables

Bibliography

Abhiroop, K., Saidas, V., & Shameem, B. . (2018). *A review on the advancement of CFD technique in ship hydrodynamics*. *8*(12), 2250–3005.

ANSYS Inc. (2016). AQWA Theory Manual. *Ansys*, *15317*(January), 174.

Armesto, J. A., Guanche, R., Jesus, F., Iturrioz, A., & Losada, I. J. (2015). Comparative analysis of the methods to compute the radiation term in Cummins' equation. *Journal of Ocean Engineering and Marine Energy*, *1*(4), 377–393. https://doi.org/10.1007/s40722-015-0027-1

Ayaz, Z., Vassalos, D., & Spyrou, K. J. (2006). Manoeuvring behaviour of ships in extreme astern seas. *Ocean Engineering*, *33*(17–18), 2381–2434. https://doi.org/10.1016/j.oceaneng.2005.10.023

Bailey, P., Hudson, D., Price, W., & Temarel, P. (2001). Time simulation of manoeuvring and seakeeping assessments using a unified mathematical model. *Transactions of the Royal Institution of Naval Architects*, *144*(February), 27–48.

Bunnik, T. H. J., van Daalen, E., Kapsenberg, G., Shin, Y., Huijsmans, R. H. M., Deng, G., Delhommeau, G., Kashiwagi, M., & Beck, B. (2010). A comparative study on state-of-the-art prediction tools for seakeeping. *28th Symposium on Naval Hydrodynamics*, *September*, 12–17.

Clarke, D. (2003). The foundations of steering and maneuvering. *Proceedings of Sixth Conference on Maneuvering and Control of Marine Crafts (MCMC 2003), Girona, Spain*, 2–16.

Cummins, W. E. (1962). The Impulse Response Function and Ship Motions. *Schiffstechnik*, *9*.

D.Clarke, P.Gelding, & G.Hine. (1982). The Application of Manoeuvring Criteria in Hull Design Using Linear Theory. In *Rina Conference* (pp. 45–68). https://www.researchgate.net/publication/281709616_The_Application_of_Manoeuvring_Criteria_in_Hull_Design_Using_Linear_Theory

de Jong, R. G. (2018). *3DP A control system model for combined DP station keeping and active roll reduction*. Technical University Delft.

De Jong, R. G., Vos, T. G., Beindorff, R., & Wellens, P. R. (2020). A control strategy for combined DP station keeping and active roll reduction. *International Shipbuilding Progress*, *66*(4), 345–372. https://doi.org/10.3233/ISP-200280

Dirix, T. (2002). *Renewed Concept Exploration Model for Manoeuvring Table*. Delft University of Technology.

Dulov, V., Kudryavtsev, V., & Skiba, E. (2020). On fetch- and duration-limited wind wave growth: Data and parametric model. *Ocean Modelling*, *153*(July 2019), 101676. https://doi.org/10.1016/j.ocemod.2020.101676

Fossen, T, I., & Perez, T. (2021). *Marine Systems Simulator (MSS)*. https://github.com/cybergalactic/MSS

Fossen, T. I. (2005). A nonlinear unified state-space model for ship maneuvering and control in a seaway. *International Journal of Bifurcation and Chaos in Applied Sciences and Engineering*, *15*(9), 2717–2746. https://doi.org/10.1142/S0218127405013691

Fossen, T. I. (2011). Handbook of Marine Craft Hydrodynamics and Motion Control. In *Handbook of Marine Craft Hydrodynamics and Motion Control*. https://doi.org/10.1002/9781119994138

Google Maps. (n.d.). *East China Sea*. Retrieved July 29, 2022, from https://www.google.com/maps/place/Oost-Chinese+Zee/@32.4024705,123.9090473,1726605m/data=!3m1!1e3!4m5!3m4!1s0x34589c6ea58

f4e61:0xb703d43857ef6c4!8m2!3d30.3953462!4d125.9152074

Ibinabo, I., & Tamunodukobipi, D. T. (2019). Determination of the Response Amplitude Operator(s) of an FPSO. *Engineering*, *11*(09), 541–556. https://doi.org/10.4236/eng.2019.119038

International Association of Classification Societies. (2001). *Standard Wave Data (North Atlantic Scatter Diagram)* (Vol. 34, Issue 34).

ITTC. (2002). The Specialist Committee on Esso Osaka Final Report and Recommendations to the 23rd ITTC. *23 Internatinal Towing Tank Conference*, *II*.

ITTC. (2011). *The Manoeuvring Committee Final report and recommendations to the 26th ITTC*.

ITTC. (2014). *The Manoeuvring Committee Final report and recommendations to the 27th ITTC*.

ITTC. (2017a). *The Manoeuvring Committee Final report and recommendations to the 28th ITTC*.

ITTC, Q. S. G. of the 28th. (2017b). *ITTC – Recommended Procedures and Guidelines ITTC Quality System Manual Recommended Procedures and Guidelines Numerical Estimation of Roll Damping ITTC – Recommended Procedures and Guidelines*.

Journée, J. M. ., & Massie, W. . (2008). *OFFSHORE HYDROMECHANICS* (second edi). Delft University of Technology.

Kanellopoulou, A., Kytariolou, A., Papanikolaou, A., Shigunov, V., & Zaraphonitis, G. (2019). Parametric ship design and optimisation of cargo vessels for efficiency and safe operation in adverse weather conditions. *Journal of Marine Science and Technology (Japan)*, *24*(4), 1223–1240. https://doi.org/10.1007/s00773-018-00620-1

Kawahara, Y., Maekawa, K., & Ikeda, Y. (2011). A simple prediction formula of roll damping of conventional cargo ships on the basis of Ikeda's method and its limitation. *Fluid Mechanics and Its Applications*, *97*(1), 465–486. https://doi.org/10.1007/978-94-007-1482-3_26

Kijima, K., Nakiri, Y., & Furukawa, Y. (2004). *On a Prediction Method for Ship Manoeuvrability*.

Kim, D. J., Yun, K., Yeo, D. J., & Kim, Y. G. (2020). Initial and steady turning characteristics of KCS in regular waves. *Applied Ocean Research*, *105*(October), 102421. https://doi.org/10.1016/j.apor.2020.102421

Larsson, L., & Raven, H. C. (2010). *The Principles of Naval Architecture Series: Ship Resistance and Flow*.

Lee, J., & Kim, Y. (2020). Study on steady flow approximation in turning simulation of ship in waves. *Ocean Engineering*, *195*, 106645. https://doi.org/10.1016/j.oceaneng.2019.106645

NSW Maritime. (2007). *INVESTIGATION REPORT INTO THE GROUNDING OF MV PASHA BULKER AND NEAR GROUNDING OF MV SEA CONFIDENCE AND MV BETIS OFF NEWCASTLE* (Issue DECEMBER).

Papanikolaou, A. (2014). Ship Design. In *Journal of the Japan Welding Society*. Springer Dordrecht Heidelberg New York London. https://doi.org/10.2207/jjws.81.251

Pérez Arribas, F. (2007). Some methods to obtain the added resistance of a ship advancing in waves. *Ocean Engineering*, *34*(7), 946–955. https://doi.org/10.1016/j.oceaneng.2006.06.002

Perez, T., & Fossen, T. I. (2009). A Matlab Toolbox for Parametric Identification of Radiation-Force Models of Ships and Offshore Structures. *Modeling, Identifification and Control*, *30*, 1–15. https://doi.org/10.4173mic.2009.1.1

Pinkster, J. A. (1980). Low frequency second order wave exciting forces on floating structures. *Wageningen, the Netherlands, Netherlands Ship Model Basin, 1980*, *650) (Thesis)*.

Schneekluth, H., & Bertram, V. (1998). *Ship Design for Efficiency and Economy*. Butterworth-Heinemann. https://doi.org/https://doi.org/10.1016/B978-0-7506-4133-3.X5000-2

Seo, M., & Kim, Y. (2011). Numerical analysis on ship maneuvering coupled with ship motion in waves. *Ocean Engineering*, *38*(17–18), 1934–1945. https://doi.org/10.1016/j.oceaneng.2011.09.023

Shigunov, V., el Moctar, O., Papanikolaou, A., Potthoff, R., & Liu, S. (2018). International benchmark study on numerical simulation methods for prediction of manoeuvrability of ships in waves. *Ocean Engineering*, *165*(July), 365–385. https://doi.org/10.1016/j.oceaneng.2018.07.031

Shigunov, V., Guo, B., Reddy, D. N., & Lalovic, I. (2019). Manoeuvrability in adverse conditions: Case studies. *Ocean Engineering*, *179*(January), 371–386. https://doi.org/10.1016/j.oceaneng.2019.02.026

SHOPERA. (2016). AIR POLLUTION AND ENERGY EFFICIENCY Results of research project "Energy Efficient Safe Ship Operation" (SHOPERA). *Imo Mepc/Inf.33*, *232*(65).

Skejic, R. (2013). Ships Maneuvering Simulations in a Seaway - How close are we to reality ? *International Workshop on Next Generation Nautical Traffic Models*, 91–101.

Skejic, R., & Faltinsen, O. M. (2006). A unified seakeeping and maneuvering analysis of a Monohull in incident waves. *Journal of Marine Science and Technology*, *13*(4), 371–394. https://doi.org/10.1007/s00773-008-0025-2

Skejic, R., & Faltinsen, O. M. (2008). A unified seakeeping and maneuvering analysis of ships in regular waves. *Journal of Marine Science and Technology*, *13*(4), 371–394. https://doi.org/10.1007/s00773-008-0025-2

Sui, C. (2021). *Energy Effectiveness and Operational Safety of Low- Powered Ocean-going Cargo Ship in Various (Heavy) Operating Conditions*.

Sui, C., Stapersma, D., Visser, K., de Vos, P., & Ding, Y. (2019). Energy effectiveness of ocean-going cargo ship under various operating conditions. *Ocean Engineering*, *190*(145), 106473. https://doi.org/10.1016/j.oceaneng.2019.106473

Taghipour, R., Perez, T., & Moan, T. (2008). *Hybrid frequency – time domain models for dynamic response analysis of marine structures*. *35*, 685–705. https://doi.org/10.1016/j.oceaneng.2007.11.002

Tello Ruiz, M. (2018). *Manoeuvring Model of a Container Vessel in Coastal Waves Manoeuvreermodel*. Universiteit Gent.

Tello Ruiz, M., Candries, M., Delefortrie, G., Peeters, D., & Mostaert, F. (2012). *Ship manoeuvrig in waves: a literature review. Version 2_0. WL rapporten, 00_96.*

Ueno, M., Nimura, T., & Miyazaki, H. (2003). *Experimental Study on Manoeuvrinc Motion of a Ship in Waves*. http://nippon.zaidan.info/seikabutsu/2003/00574/contents/0352.htm

Uharek, S. A. (2019). *Numerical Prediction of Ship Manoeuvring Performance in Waves*.

Ventikos, N. P., Papanikolaou, A. D., Louzis, K., & Koimtzoglou, A. (2018). Statistical analysis and critical review of navigational accidents in adverse weather conditions. *Ocean Engineering*, *163*(June), 502–517. https://doi.org/10.1016/j.oceaneng.2018.06.001

Vinet, L., & Zhedanov, A. (2011). A "missing" family of classical orthogonal polynomials. In *Journal of Physics A: Mathematical and Theoretical* (Vol. 44, Issue 8). Cambridge University Press. https://doi.org/10.1088/1751-8113/44/8/085201

Wicaksono, A., & Kashiwagi, M. (2018). Wave-induced steady forces and yaw moment of a ship advancing in oblique waves. *Journal of Marine Science and Technology (Japan)*, *23*(4), 767–781. https://doi.org/10.1007/s00773-017-0510-6

Wicaksono, A., & Kashiwagi, M. (2019). *Efficient coupling of slender ship theory and modular maneuvering model to estimate the ship turning motion in waves E ffi cient Coupling of Slender Ship Theory and Modular Maneuvering Model to Estimate the Ship Turning Motion in Waves*. *July*.

World Meteorological Organization. (2017). *Manual on Codes, International Codes, VOL. I.1: Vol. I* (Issue WMO-No. 306).

Yasukawa, H., Hirata, N., Matsumoto, A., Kuroiwa, R., & Mizokami, S. (2019). Evaluations of wave-induced steady forces and turning motion of a full hull ship in waves. *Journal of Marine Science and Technology (Japan)*, *24*(1), 0. https://doi.org/10.1007/s00773-018-0537-3

Yasukawa, H., & Yoshimura, Y. (2015). Introduction of MMG standard method for ship maneuvering predictions. *Journal of Marine Science and Technology (Japan)*, *20*(1), 37–52. https://doi.org/10.1007/s00773-014-0293-y

Zhang, W., Zou, Z.-J., & Deng, D.-H. (2017). A study on prediction of ship maneuvering in regular waves. *Ocean Engineering*, *137*(January), 367–381. https://doi.org/10.1016/j.oceaneng.2017.03.046